Synthesis, Surface Functionalization of Germanium Nanoparticles, and Their Application in Polymer Hybrid Solar Cells

by

Md Asjad Hossain

A thesis submitted in partial fulfillment of the requirements for the degree of

Master of Science

Department of Chemistry

University of Alberta

Abstract

Germanium nanoparticles (GeNPs) have immense potential in various applications, such as opto-electronics, batteries, bioimaging, etc. Germanium has a small band gap (0.67 eV in bulk), large exciton Bohr radius (~24 nm), high absorption coefficient (*ca.* 2.0×10^5 cm^{-1} at 2 eV), and high carrier transport (μ_e = 3900 $cm^2V^{-1}S^{-1}$, μ_h = 1900 $cm^2V^{-1}S^{-1}$). Despite the favourable opto-electronic properties, their potential cannot be utilized fully due to the lack of a robust synthetic method, complex surface chemistry, and non-uniform shape and size distribution. Significant research has been done over the past years; however, unlike silicon nanoparticles, the chemistries are often unpredictable. Till now, synthetic strategies could not achieve spherical GeNPs. There are examples of cubic and hexagonal shapes, but their distributions are not uniform. In addition to size and shape, surface chemistries of GeNPs also are not explored much. Hydrogermylation has been done on the surface of GeNPs, but there are other surface reactions that need to be explored, such as dehydrocoupling. In this thesis, dehydrocoupling surface reactions were studied. GeNPs also were applied as a dopant to enhance the efficiency of the polymer solar cells.

The thesis starts with an introduction to germanium nanoparticles, their common synthetic procedures, surface passivation strategies, properties, and applications. Chapter 2 focuses on the synthesis and surface functionalization of GeNPs via dehydrocoupling. A series of reactions were performed with hydride-terminated GeNPs (H-GeNPs) and octadecylsilane to determine the optimum reaction conditions. Then, dimethyloctadecylsilane and hydride-terminated polydimethylsiloxane were reacted with H-GeNPs to passivate the surface of H-GeNPs. Hydrogermylation with 1-octadecene also was carried out in order to compare their reactivity. In Chapter 3, GeNPs were used as a

dopant or efficiency enhancer in the active layer of polymer solar cells. Upon addition of small amounts of GeNPs, the efficiency of solar cells was improved. Chapter 4 focuses on the synthesis of GeNPs via induction heating, which allows for repeated fast heating and cooling cycles in order to obtain a better shape and size distribution of GeNPs. Finally, Chapter 5 summarizes the outcome of the experimental results and describes future directions.

Preface

The thesis is an original work by Md Asjad Hossain. It was done under the supervision of Professor Dr. Jonathan G. C. Veinot at the Department of Chemistry, University of Alberta. No part of the thesis has been published previously.

In Chapter 2, Dr. Morteza Javadi and I designed the project and carried out some experiments. I performed most of the experiments, designed the optimum reaction conditions, performed the characterizations, analyzed the data, and wrote the thesis. Haoyang (Emmett) Yu helped in some of the characterizations, such as Raman, TEM, and EDX mapping. Alyxandra N. Thiessen helped in measuring some of the XRDs. Dr. Anton Oliynyk performed the refinement of XRD and calculated the crystallite sizes. Dr. Jonathan G. C. Veinot supervised the project and helped me with the composition of the chapter.

In Chapter 3, the synthesis of germanium nanoparticles and their characterizations were performed in the Department of Chemistry, University of Alberta, Canada. The organic–inorganic hybrid thin films and the solar cells were prepared in the Department of Physics, Technical University of Munich, Germany, under the supervision of Professor Dr. Peter Müller-Buschbaum. Nian Li helped me with characterizations such as AFM, GISAXS, and GIWAXS. Hongwon Kim helped me with the fabrication of solar cells and measuring their performance. I performed most of the experiments and characterizations, analyzed the data, and wrote the chapter. Dr. Anton Oliynyk performed the refinement of XRD and calculated the crystallite sizes. Dr. Jonathan G. C. Veinot and Dr. Peter Müller-Buschbaum supervised the project.

In Chapter 4, I performed all the experiments, carried out the characterizations, analyzed the data, and wrote the chapter. Dr. Jonathan G. C. Veinot supervised the project and helped me with the composition of thesis.

Dedicated to my lovely wife.....

Tahamina Akter Rubi

Genius is one percent inspiration and ninety-nine percent perspiration……

-Thomas Alva Edison

Acknowledgements

Throughout my graduate studies, I received support and assistance from my supervisor, colleagues, and friends.

First, I would like to acknowledge my gratitude to my supervisor, Professor Dr. Jonathan G. C. Veinot. His immense support and guidance helped me throughout my graduate studies. He pushed me whenever needed and encouraged me when I felt down.

I would like to thank my supervisory committee members, Dr. Mariusz Klobukowski and Dr. Michael Serpe, for their valuable advice and comments throughout my graduate study. I would like to thank Professor Dr. Arthur Mar for letting me use the induction furnace and Dr. Anton Oliynyk for helping me with the crystallite size determination from XRD.

I was very fortunate to work with the Veinot group. I am really grateful to the past and present group members for their support during my stay at UofA. I am especially grateful to Dr. Morteza Javadi for being a mentor in the lab and helping me to start my research in the group. I am thankful to Haoyang (Emmett) Yu for helping me in characterizing samples and giving me advice. I would like to thank all my past and present colleagues in the group, namely Dr. Regina Sinelnikov, Dr. Maryam Aghajamali, Alyxandra N. Thiessen, Christopher Robidillo, Subha Jana, Xiyu (Zach) Zhang, Jonathan Hiltz, Nduka Ikpo, Sarah Milliken, Yingjie (Jay) He, I Teng Cheong and many others.

I am grateful to the ATUMS community for allowing me to do a research exchange visit at the Technical University of Munich. ATUMS also organized many professional development seminars and career coaching for the trainees to make them competitive in their future career. Special thanks to Leah Veinot and Sergei Vagin for helping me on numerous occasions. I would like to thank my collaborator in Germany, Prof. Peter Muller-Buschbaum, for hosting me and allowing me to work on polymer solar cells at the Technical University of Munich. I would like to thank Nian Lee and Dr. Nuri Hohn who helped in my research during my stay in Munich.

I would like to thank the technical support staff of the analytical lab, machine shop, electronic shop, and glass shop, especially Dr. Wayne Moffat, Jennifer Jones, and Andrew Hiller. I also want to thank NanoFAB staff, especially Peng Li, Dr. Shihong Xu, Dr. Anqiang He, and Dr. Nancy Zhang.

Special gratitude to Dr. Anna Jordan for editing the English of my thesis. Despite my repetitive grammatical mistakes, she was quite patient and walked me through my entire thesis. Anna, you are a lively and cheerful person, and you are a good friend.

Rubi, I cannot express the support that I got from you in words, thank you so much. Other than science, you supported me every way possible for my successful graduate study. I also want to acknowledge the contribution of my family and friends, especially my Mom and Dad. Without you, I would not be where I am now.

Table of Contents

Chapter 1 Introduction

Chapter 2 Thermally-induced Dehydrocoupling on Germanium Nanoparticles

Chapter 3 Germanium Nanoparticles-Polymer Hybrid Solar Cells

Chapter 4 Inductive Heating to Synthesize a Uniform Size and Shape of Germanium Nanoparticles

Chapter 5 Summary and Future Directions

List of Figures

List of Tables

List of Schemes

List of Symbols, Nomenclature, and Abbreviations

Å	Angstrom
ºC	Degree Celsius
0D	Zero-dimensional
1D	One-dimensional
2D	Two-dimensional
3D	Three-dimensional
AC	Alternating current
a. u.	Arbitrary unit
AFM	Atomic force microscopy
ASH	Average shifted histogram
BHJ	Bulk heterojunction
CB	Conduction band
CVD	Chemical vapor deposition
CQDs	Carbon quantum dots
CuPc	Copper pthalocyanine
D-A	Donor-acceptor
DHC	Dehydrocoupling
DLS	Dynamic Light Scattering
DSSC	Dye sensitized solar cell
EDX	Energy dispersive X-ray
EEL	Electron extraction layer
EELS	Electron energy loss spectroscopy
FTIR	Fourier transform infrared
FTO	Fluorine-doped tin oxide
FWHM	Full width and half maxima
GIXS	Grazing Incidence X-ray Scattering
GeNPs	Germanium nanoparticles
GeNPs/GeO*x*	Germanium nanoparticles embedded in germanium oxide
GQDs	Graphene quantum dots
GISAXS	Grazing Incidence Small Angle X-ray Scattering

GIWAXS	Grazing Incidence Wide Angle X-ray Scattering
H	Hour(s)
HEL	Hole extraction layer
HMDS	Hexamethyldisilazane
HAADF	High annular dark field
HF	Hydrofluoric acid
HOMO	Highest occupied molecular orbital
HRTEM	High-resolution transmission electron microscopy
H-PDMS	Hydride-terminated polydimethyl siloxane
HPLC	High-performance liquid chromatography
H-GeNPs	Hydride-terminated germanium nanoparticles
IT-4F	3,9-bis(2-methylene-((3-(1,1-dicyanomethylene)-6,7-difluoro)-indanone))-5,5,11,11-tetrakis(4-hexylphenyl)-dithieno-[2,3-d:2',3'-d']-s-indaceno[1,2-b:5,6-b']dithiophene
ITO	Indium-tin oxide
LMA	Local monodisperse approximation
LIBs	Lithium-ion batteries
LUMO	Lowest unoccupied molecular orbital
Mg	Milligram(s)
mL	Millilitre(s)
min	Minute(s)
MEH-PPV	Poly[2-methoxy-5-(2-ethylhexyloxy)]-1,4-phenylenevinylene
NIR	Near infrared
NMR	Nuclear magnetic resonance
NPs	Nanoparticles
Nm	Nanometer
OD-XAS	Optically detected X-ray absorption spectroscopy
OSC	Organic solar cell
PCE	Power conversion efficiency
PL	Photoluminescence
PEG	Polyethylene glycol

PPV	Poly(phenylenevinylene)
PSC	Polymer solar cell
PEDOT:PSS	Poly(3,4-ethylene-dioxythiophene):poly(styrenesulfonate)
PTB7-Th	Poly([2,6′-4,8-di(5-ethylhexylthienyl)benzo[1,2-b;3,3-b]dithiophene]{3-fluoro-2[(2ethylhexyl) carbonyl] thieno [3,4-b]thiophenediyl})
P3HT	Poly(3-hexylthiophene)
PTFE	Polytetrafluoroethylene
QDs	Quantum dots
QDSC	Quantum dot sensitized solar cell
rGO	Reduced graphene oxide
rpm	Revolutions per minute
SILAR	Successive ion layer adsorption and reaction
STEM-EDX	Scanning transmission electron microscopy–energy dispersive X-ray
STM	Scanning tunneling microscopy
SDD	Sample to detector distance
TMS	Tetramethylsilane
TEM	Transmission electron microscopy
TBAB	Tetrabutylammonium bromide
THAB	Tetrahexylammonium bromide
TOAB	Tetraoctylammonium bromide
TKAB	Tetrakis(decyl)ammonium bromide
VB	Valence band
XAS/EXAFS	X-ray absorption spectroscopy/ extended X-ray absorption fine structure
XPS	X-ray photoelectron spectroscopy
XRD	X-ray diffraction

Chapter 1

Introduction

1.1 Nanomaterials

According to the European Commission, "Nanomaterial means a natural, incidental, or manufactured material containing particles, in an unbound state or as an aggregate or as an agglomerate and where, for 50% or more of the particles in the number size distribution, one or more external dimensions is in the size range 1 nm–100 nm".[1] Lowering the size brings a lot of changes in the properties of the materials. Therefore, nanomaterials have applications in many different fields, including electronics, energy harvestings, sensors, medicines, etc. There are four types of nanomaterials depending upon the dimensionality of the materials, i.e. zero-dimensional (e.g., quantum dots, fullerene), one-dimensional (e.g., nanotubes, nanowires), two-dimensional (e.g., graphene), and three-dimensional (e.g., nanocomposites).[2] To put things into perspective, a comparison between nanomaterials and bulk objects are shown in Figure 1.1.

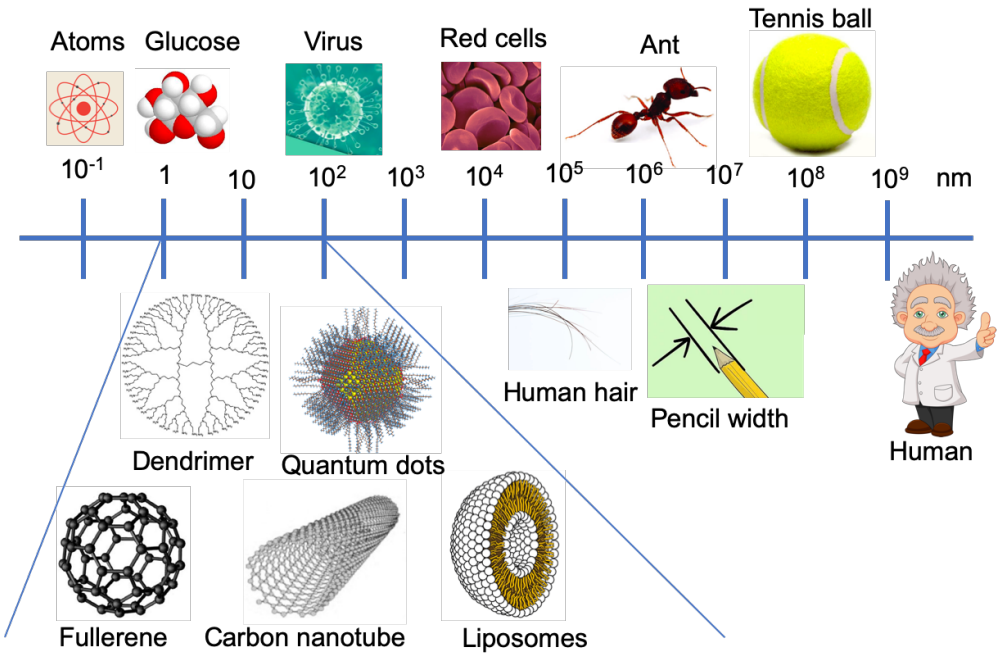

Figure 1.1. A size comparison between nanomaterials with other large-sized materials.

1.2 Quantum Dots and Quantum Confinement

When semiconductor nanoparticles have a smaller size than the exciton Bohr radius, they are called quantum dots (QDs).[3] Their sizes often are 1–10 nm for most semiconductors. In addition, QDs show size- and surface-dependent photoluminescence (PL).[4] When UV light is shone on QDs, an electronic transition occurs from the valence band to the conduction band leaving holes. The electrons and holes electrostatically bound to each other are called excitons. When the electrons relax back to the valence band, the resultant energy is radiated as photoluminescence. Due to the small sizes of QDs, they often are referred to as artificial atoms.[5,6] Their properties lie between the bulk semiconductors and the discrete atoms or molecules. The reason QDs show different properties from the bulk semiconductors is due to a phenomenon called the quantum confinement effect.[7] As the size of a bulk semiconductor decreases, the density of the energy states decreases, and the energy difference (band gap) between the valance band and the conduction band increases. Thus, lowering the size of QDs shows a blue shift in the photoluminescence.[8] Figure 1.2 shows different colors of PL originating from the different sizes of CdSe/ZnS core-shell nanocrystals and the change of band gap due to the quantum confinement effect.

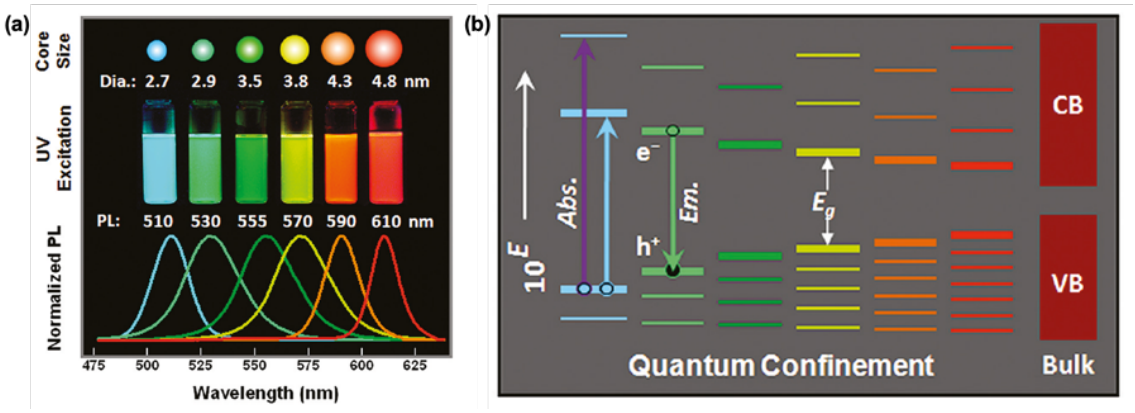

Figure 1.2. (a) Cartoon, photograph, and PL spectra illustrating the color changes of CdSe/ZnS with increasing nanocrystal size. (b) An increase in the band gap of QDs with a decrease in their size due to the quantum confinement effect.[8] Reprinted with permission from reference 8. Copyright 2011 American Chemical Society.

Different kinds of quantum dots have been studied in the last decades. Cd- and Pb-based quantum dots were explored more due to their unique opto-electronic properties,

such as tunable photoluminescence, high quantum yield, narrow PL width, and good photostability. Examples are CdSe,[9] CdS,[10] PbSe,[11] PbS,[12] InP,[13] InAs,[14] Si,[15] Ge,[16] etc. QDs have shown applications in LEDs,[17] bioimaging,[18] photovoltaics,[19] photodetectors,[20] photocatalysis,[21] etc.

1.2.1 Group 14-Based Quantum Dots

Although QDs have remarkable properties and applications, their practical utility is limited due to their toxicity. Most QDs contain a heavy metal, such as cadmium (Cd) or lead (Pb). Research has shown that CdSe QDs are toxic to the cells and can build up in vital organs on prolonged exposure. The European commission has restricted the use of heavy metal containing materials in consumer electronics.[22] Therefore, research on nontoxic QDs has increased significantly in the last couple of years, and the attention is on Group 14 elements because of their non-toxicity and environment friendly characteristics. Carbon based QDs, such as carbon quantum dots (CQDs) and graphene quantum dots (GQDs), are showing potential applications in electroanalysis and bioimaging.[23] Silicon and germanium QDs also have shown promising applications in displays, photocatalysis, bioimaging, and photovoltaics.[22,24] Although, the synthesis, reactivity, and properties of Si QDs have been well studied and understood, Ge QDs have been investigated less and it is a challenge to synthesize well defined sizes and shapes of Ge QDs.

1.3 Germanium Nanoparticles

Germanium nanoparticles (GeNPs) are of research interest for their application in various fields, such as solar cells, field-effect transistors, memory devices, photodetectors, and biological imaging.[25] The GeNPs offer a lower toxicity and a more environmentally friendly alternative to common narrow band gap semiconductor nanoparticles that contain toxic metals, such as Pd, Cd, or Hg. They have a small band gap (0.67 eV in bulk) and show the quantum confinement effect in relatively larger particles (~24 nm exciton Bohr radius).[22]

To understand the properties and explore the applications of GeNPs, it is important to synthesize them controllably with well-defined sizes and shapes. For other nanoparticle systems, such Cd and Pb, researchers gained knowledge on how to control the size, shape

and uniformity, but such knowledge could not be obtained for germanium. The limitations are mainly due to the complexity of their synthesis. Germanium is an extended covalent crystal that is difficult to prepare on the nanoscale.[25] Harsh chemicals, such as sodium metal, metal hydrides, *n*-butyllithium, sodium naphthalide, etc., are required to synthesize GeNPs from their salts. Despite that, significant research has been done to control their synthesis and understand their properties. The following sections will highlight some of their synthesis, surface functionalization, and optical properties.

1.3.1 Synthesis of Germanium Nanoparticles

The synthesis of GeNPs can be divided broadly into two categories: physical and chemical methods. Physical methods include chemical vapor deposition (CVD),[26] etching,[27,28] plasma techniques,[29,30] gas-phase pyrolysis,[31] laser ablation,[32] sputtering,[33] and ion implantation.[34] Chemical methods include chemical reduction, thermal reduction, thermal decomposition, and metathesis reactions.[25] The discussion will focus mainly on the chemical methods for the synthesis of GeNPs.

1.3.1.1 Chemical Reduction of Germanium Compounds

Chemical reduction of germanium compounds was performed mainly on germanium halides, such as $GeCl_4$, GeI_4, and GeI_2. $GeCl_4$ was used to synthesize GeNPs by Weller and coworkers. The authors used lithium naphthalide to reduce Ge(IV) to Ge(0) and CH_3SiCl to passivate the dangling bonds on the GeNP surfaces, but the particles were polydisperse.[35] Sodium naphthalide was used to reduce $GeCl_4$ by Lee et al.[36] and Chiu et al.[37,38] A hydride reducing agent, such as $NaBH_4$, $LiBH_4$, and $N_2H_4.H_2O$, was used first by Jiang and coworkers to reduce $GeCl_4$ ultrasonically at room temperature.[39] The authors synthesized 3–11 nm GeNPs with a broad size distribution. Later, Tilley and coworkers reduced $GeCl_4$ by $LiAlH_4$, $Li(C_2H_5)_3BH$, $LiBH_4$, and $NaBH_4$. The GeNPs were passivated by allylamine using H_2PtCl_6 as a catalyst at room temperature, and they obtained monodisperse GeNPs ranging from 4.0 to 5.5 nm.[40] Carolan and Doyle extended the hydride reduction of $GeCl_4$ by formation of an inverse micelle to control the growth of GeNPs.[41] The authors used cationic quaternary ammonium salts, tetrabutylammonium bromide (TBAB), tetrahexylammonium bromide (THAB), tetraoctylammonium bromide (TOAB), and

tetrakis(decyl)ammonium bromide (TKAB), to control the growth of GeNPs, and then passivated them by allylamine using H_2PtCl_6 as a catalyst, similar to Tilley and coworkers. These water soluble GeNPs were fairly monodisperse, ranging from 3.5 to 4.5 nm (Figure 1.3).

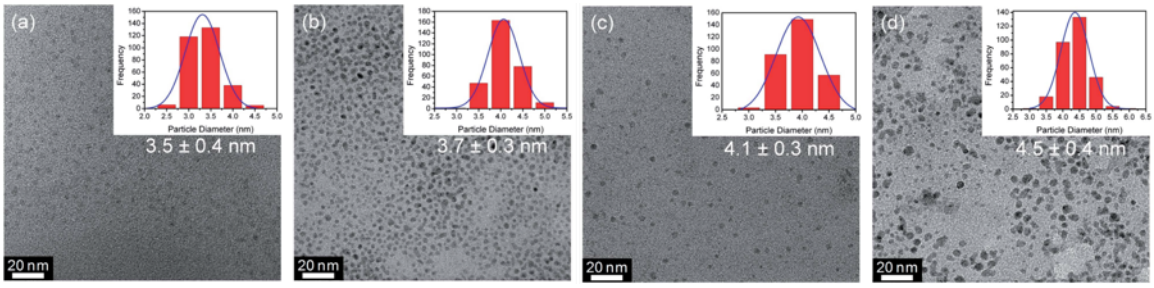

Figure 1.3. Bright-field Transmission Electron Microscopy (TEM) images of Ge nanocrystals (GeNCs) synthesized using the various cationic surfactants (a) TBAB, (b) THAB, (c) TOAB, and (d) TKAB. Inset: size histograms of Ge NCs with curves fitted to the data using a Gaussian model.[41] Reprinted with permission from reference 41. Copyright 2014 Royal Society of Chemistry.

GeI_4 and GeI_2 were reduced by a different reducing agent to synthesize GeNPs.[42,43] Schaak and coworkers mixed GeI_4 with hexamethyldisilazane (HMDS), oleylamine, and oleic acid at 260 ºC.[42] By changing the amount of GeI_4, 6, 12, and 22 nm GeNPs were synthesized. Neale and coworkers synthesized alkyl-terminated GeNPs by reducing GeI_4/GeI_2 mixtures.[44] The proposed mechanism was to seed Ge(0) by the reduction of Ge(II) at 220 ºC; growth occurs from the reduction of Ge(IV) at 250–300 ºC. A mixture of GeI_4/GeI_2 also was reduced by oleylamine by heating in a microwave oven or in a conventional furnace by Kauzlarch and coworkers.[45] The authors were able to obtain 4–11 nm sizes of GeNPs with a simple and safe method without using a strong reducing agent. Recently, Pescara et al. synthesized oleylamine- and hexadecylamine- capped GeNPs by reduction of triphenylgermanium chloride by sulphur.[46]

1.3.1.2 Thermal Reduction of Germanium Precursors

Thermal reduction of germanium precursors is involved mainly in the reduction of sol-gel derived polymers. Veinot and coworkers[47] reported a sol-gel polymer, $(C_6H_5GeO_{1.5})_n$, derived from trichlorogermane. Upon heating at 500 ºC in 5% He/95% Ar or at 600 ºC in

100% Ar, the polymer decomposes via disproportionation and reduction pathways to form crystalline GeNPs embedded in a GeO_2 matrix. The GeO_2 matrix was dissolved in hot water, and the GeNPs were liberated. Similarly, sol-gel derived GeNPs were reported by Ozin et al.[48] and Boyle et al.[49,50]

Recently, Javadi et al.[51] reported a synthesis of $Ge(OH)_2$, which then undergoes thermal disproportionation at 400 ºC to yield GeNPs embedded in a GeO_2 matrix (Figure 1.4). The GeO_2 matrix was dissolved by ethanolic hydrofluoric acid, and the obtained hydride-terminated GeNPs were subjected to thermal and radical hydrogermylation to yield dodecyl-GeNPs.

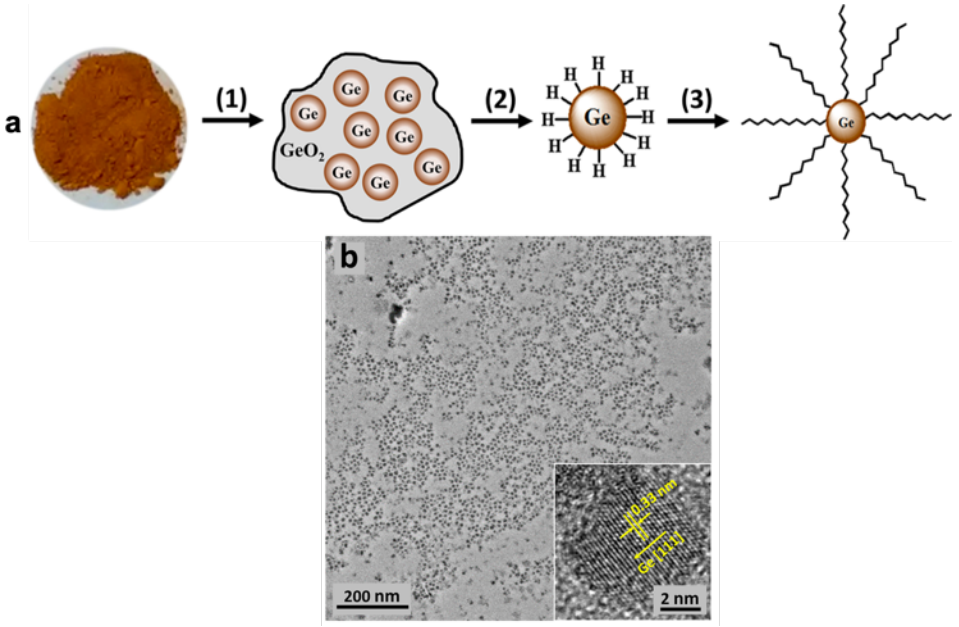

Figure 1.4. (a) (1) Thermal processing of $Ge(OH)_2$ at T = 400 °C in Ar, (2) liberation of H-GeNPs via HF etching, and (3) functionalization/surface modification of GeNPs through hydrogermylation. (b) Bright-field TEM image of dodecyl-GeNPs prepared by thermal hydrogermylation.[51] Reprinted with permission from reference 51. Copyright 2017 American Chemical Society.

1.3.1.3 Thermal Decomposition of Germanium Precursors

Thermal decomposition of organogermane includes the decomposition of zero-valent organogermane precursors to the elemental germanium at a high temperature. Gerion et al.[52] reported that tetraethylgermane decomposed in a high-pressure reactor at 430 ºC to yield crystalline GeNPs embedded in a hydrocarbon matrix. Zaitseva et al.[53] reported a hot

injection method to produce GeNPs by injecting organogermane precursors, such as trichlorogermane, tetramethylgermane, tetraethylgermane, and tetrabutylgermane, into pre-heated organic solvents, such as trioctylamine, squalene, and octacosane. They obtained 2–7 nm GeNPs from tetrachlorogermane and 4–15 nm GeNPs from tetrabutylgermane in squalene.

Purkait et al.[54] reported a one-pot synthesis of alkyl-GeNPs by decomposition of a Ge(II) dihydride at 190 ºC via hot injection and microwave irradiation. The synthesis and surface functionalization occurred in-situ in the presence of capping ligands; they obtained 10-nm particles via hot injection and 5-nm particles via microwave irradiation (Figure 1.5). Korgel et al.[55] introduced a supercritical fluid method of synthesizing GeNPs by using tetraethylgermane at 400–550 ºC and 20.7 MPa pressure in a continuous flow reactor.

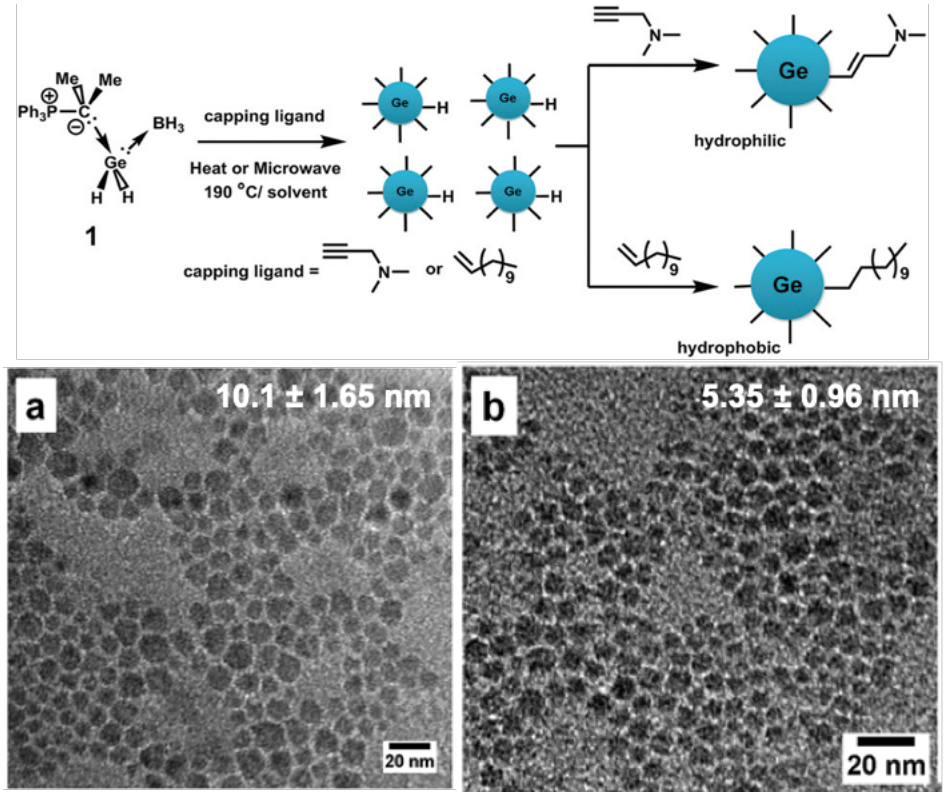

Figure 1.5. Synthesis and functionalization of GeNPs by decomposition of $Ph_3PCMe_2 \cdot GeH_2 \cdot BH_3$ (Top). Representative bright field TEM images of dodecyl-GeNPs via (a) thermal and (a) microwave irradiation. [54] Reprinted with permission from reference 54. Copyright 2015 Royal Society of Chemistry.

1.3.1.4 Metathesis Reactions of Germanium Zintl Salts

An alternative way to obtain GeNPs was demonstrated first in 1998 by Kauzlarich and coworkers, who exploited metathesis reactions between sodium germanide (NaGe) and $GeCl_4$.[56] More experiments were performed by the Kauzlarich group to obtain GeNPs using different Zintl salts, such as KGe and Mg_2Ge, which were reacted with $GeCl_2$ and $GeCl_4$, respectively, over the last couple of years.[57–59] The McMillan group also exploited the synthesis of GeNPs from Mg_2Ge and $GeCl_4$ and studied their formation by in-situ XAS/EXAFS.[60] The authors concluded that the solvent should be extremely dry in order to avoid oxide formation, but they only obtained amorphous GeNPs by this method.

Recently, Qian and coworkers[61] synthesized mesoporous GeNPs by the metathesis reaction of Mg_2Ge and $ZnCl_2$ in an autoclave at 300 ºC (Figure 1.6). The mesoporous GeNPs were used for lithium ion battery applications.

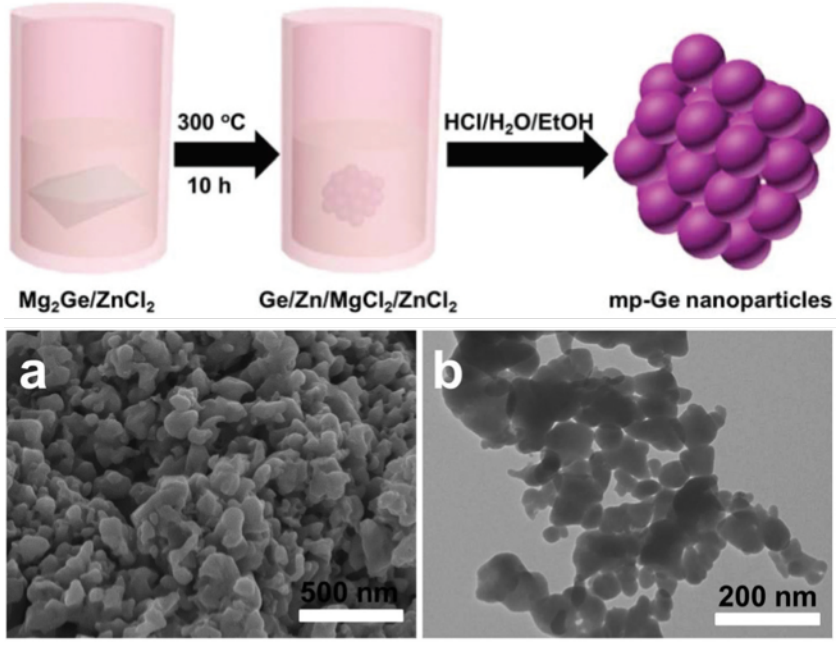

Figure 1.6. Synthesis of mesoporous GeNPs via a Zintl salt metathesis reaction (top). Representative (a) scanning electron microscopy (SEM) image and (a) a bright-field TEM image mesoporous GeNPs.[61] Reprinted with permission from reference 61. Copyright 2018 Royal Society of Chemistry.

1.3.2 Surface Passivation Strategies

The surfaces of GeNPs are extremely air and moisture sensitive, and they need to be protected by surface capping agents or ligands, which shield the nanoparticle surface from oxidation. In most cases, semiconductor nanoparticles are passivated with a surface ligand to exploit their solution processability. In addition, ligands control their growth rate, crystal structure, and morphology before nucleation. After nucleation, they stabilize the particles and protect them from further growth and aggregation. Ligands also impact the optical properties of GeNPs.[62] Surface passivation reactions on GeNPs are broadly of two types: organic and inorganic passivation. In organic passivation, organic molecules react to form covalent bonds on the surface of GeNPs, while in inorganic passivation, another semiconductor grows epitaxially on the surface of GeNPs.

1.3.2.1 Reactions of Hydride-terminated GeNPs

Hydrides are the most commonly encountered capping groups during the synthesis of GeNPs. However, the Ge–H bond is highly reactive to air/moisture and produces oxide-terminated GeNPs upon exposure to air. Therefore, a protective shell needs to be made in order to utilize GeNPs in applications. Hydrogermylation is the most widely used approach to passivate the surface of GeNPs. The reactions involve a hydride-terminated GeNP and an alkene/alkyne. The reaction proceeds via heat, UV light, a radical initiator, or a catalyst. The key to this reaction is to form a strong covalent bond (Ge–C) in order to acquire long term photostability or dispersibility in a wide range of solvents.

Kortshagen and coworkers[30] obtained hydride-terminated GeNPs (H-GeNPs) by plasma methods using $GeCl_4$ and H_2 flow. Next, the H-GeNPs were subjected to hydrogermylation with 1-dodecene at 165 ºC to obtain dodecyl-passivated freestanding GeNPs. Similarly, Veinot and coworkers[63] reduced GeI_4 by $LiAlH_4$, and the resulting H-GeNPs were subjected to hydrogermylation with *n*-undecene to obtain *n*-undecenyl-GeNPs. The alkyl groups generally facilitate the solubility of the GeNPs in a non-polar solvent. To address the solubility in a polar solvent, Tilley and coworkers[64] prepared allylamine-passivated GeNPs. Purkait et al.[54] synthesized 5.35 nm dodecyl-GeNPs that are soluble in a non-polar solvent and 3-dimethylamino-1-propene capped GeNPs that are

soluble in a polar solvent. Using similar chemistry, Carolan et al.[65] synthesized epoxy, acetate, amine, carboxylic acid, and alkyl terminated GeNPs, which showed tunable photoluminescence by surface bonded ligands (Figure 1.7). Similar observations also were reported by McVey et al.[66]

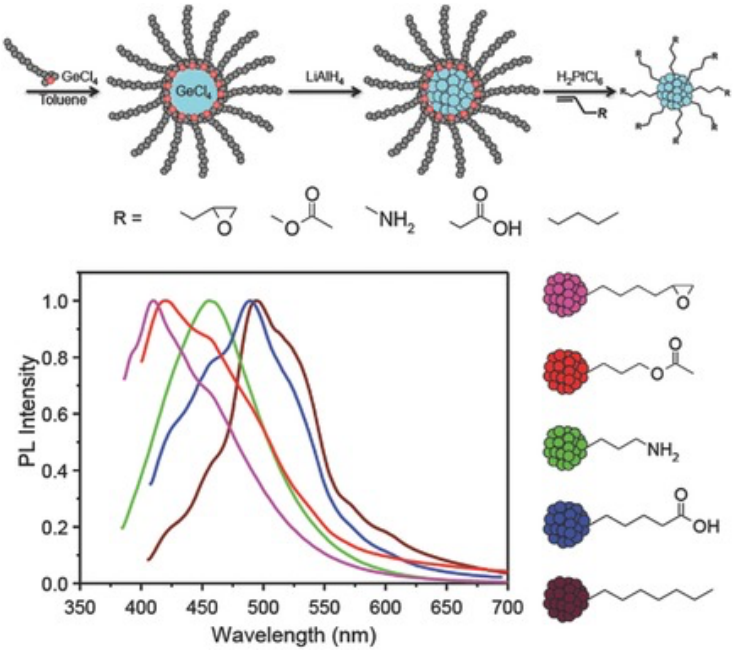

Figure 1.7. Schematic drawings of the synthesis of GeNPs and normalized PL spectra (λ_{ex}: 370 nm) of chloroform dispersions of GeNPs terminated with each of the different functional groups.[65] Reprinted with permission from reference 65. Copyright 2017 Wiley -VCH GmbH & Co. KGaA, Weinheim.

1.3.2.2 Reactions of Halide-terminated GeNPs

Halide-terminated germanium nanoparticles (X-GeNPs) are another air- and moisture-sensitive surface group that forms during the synthesis of GeNPs while a Zintl salt metathesis reaction between a metal germanide and a germanium halide occurs. Then the X-GeNPs are subjected to reactions with alkyl lithium and Grignard reagent to form alkyl-terminated GeNPs. For example, Kauzlarich and coworkers obtained alkyl, acetals, alcohols, esters and polymers passivated GeNPs using a metathesis approach of germanium Zintl salts (Figure 1.8).[59]

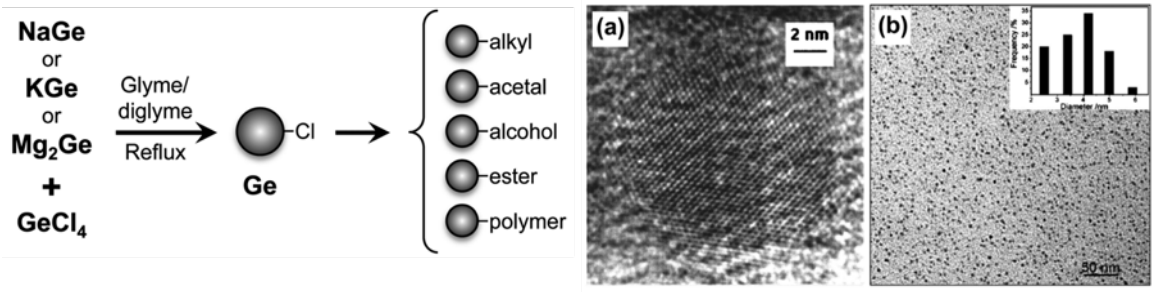

Figure 1.8. The synthesis of GeNPs via a metathesis reaction between Ge Zintl salts and $GeCl_4$ and examples of bright field TEM images and a size distribution histogram.[57] Reprinted with permission from reference 57. Copyright 2008 Elsevier Inc.

1.3.2.3 Inorganic Passivation of GeNPs

Surface passivation of GeNPs is applied mostly via organic molecules that involves either Ge–C or Ge–Si bond on the surface.[25,35] The inorganic passivation is popular among Group II–VI, IV–VI, and III–V semiconductors.[67] Guo et al. reported a successive ion layer adsorption and reaction (SILAR) method to grow a CdS and ZnS shell epitaxially on the surface of the Ge nanocrystal.[68] The authors observed that the presence of an epitaxial II–VI shell enhances the near-infrared photoluminescence greatly and also improves the photoluminescence stability of Ge.

Kortshagen and coworkers[69] reported a gas phase synthesis of core-shell Ge/Si NPs in a flow-through nonthermal plasma reactor. The authors studied the growth of the Si shell on GeNPs by varying the amount of SiH_4 gas in the reactor and observed it by scanning transmission electron microscopy–energy dispersive X-ray (STEM-EDX) mapping (Figure 1.9).

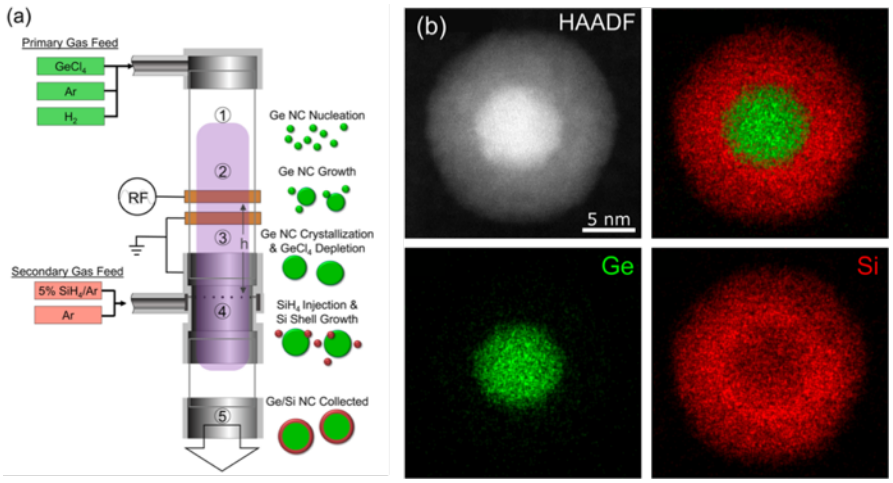

Figure 1.9. (a) Schematic drawings of the follow-through nonthermal plasma reactor to synthesize core-shell Ge/Si nanocrystals and (b) high angular annular dark field image (HAADF) and STEM-EDX mapping of a Ge/Si nanocrystal. Reprinted with permission from reference 69. Copyright 2017 American Chemical Society.

1.3.3 Optical Properties of GeNPs

The origin of photoluminescence of Ge quantum dots has been a debate for almost 28 years after the first discovery of GeQDs PL by Maeda et al. in 1991.[70] Germanium is an indirect band gap semiconductor similar to silicon. Veinot and coworkers investigated the quantum confinement effect of different sizes of GeNPs and observed their band gaps using scanning tunneling microscopy (STM).[71] According to the band gap report, GeNPs should give emission at the near infrared (NIR) region. In fact, NIR emission was observed in the research of Klimov, Neale, and Kortshagen research groups from alkyl passivated GeNPs.[44,72,73]

In contrast, a significant number of researchers found visible PL in GeNPs. However, it is difficult to understand whether the luminescence is due to the confinement effect or the surface defects. Researchers often report contradictory results even in their own publications. For example, the Kauzlarich group showed blue PL from alkyl-GeNPs, which was attributed to quantum confinement, and in another study, they attributed it to the surface defects.[56–58] Doyle and coworkers showed size dependent visible PL, which was attributed to quantum confinement, and later they reported a surface dependent PL property of GeNPs (Figure 1.10).[41,65] Similarly, Tilley and coworkers reported a size dependent PL in 2010 and a surface dependent PL in 2017.[40,66]

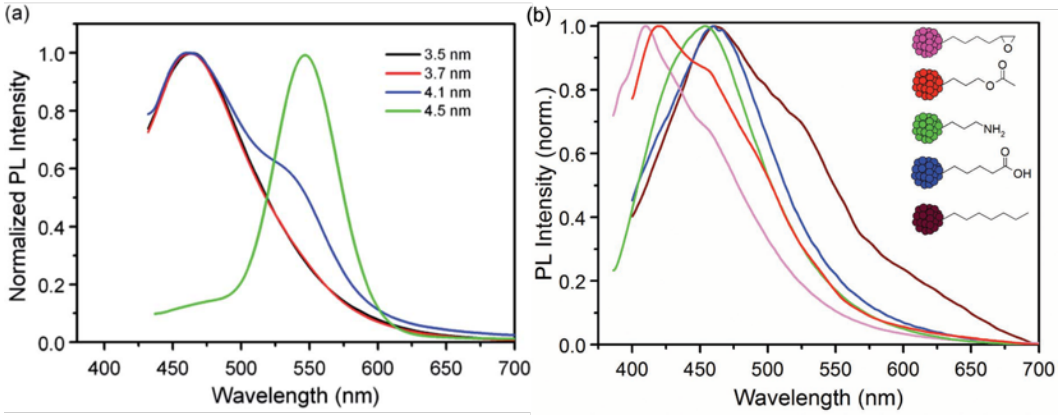

Figure 1.10. (a) PL emission of allylamine capped GeNPs with different sizes attributed to the quantum size effect[41] and (b) PL emission of 4.1 nm GeNP having different functional groups attributed to the surface effect.[65] Reprinted with permission from reference 41 and 65. Copyright 2014 Royal Society of Chemistry. Copyright 2017 Wiley -VCH GmbH & Co. KGaA, Weinheim.

A conclusive explanation was reported by Little et al.,[74] who investigated the origin of PL of hydride-terminated and oxide-terminated GeNPs using optically-detected X-ray absorption spectroscopy (OD-XAS). The authors concluded that in oxidized particles, the PL emission due to the surface oxides and in hydride-terminated particles is from a disordered structure in the surface. Again, if we look carefully at the visible emitting particles, they either have nitrogen containing ligands or their synthesis was carried out in a nitrogen containing solvent. In fact, Veinot and coworkers provided conclusive evidence that the presence of nitrogen containing ligands leads to blue PL in GeNPs.[54] The authors synthesized *ca.* 5 nm dodecyl-GeNPs and 3-dimethylamino-1-propyl-GeNPs, where the alkyl capped particles did not show any visible PL, while the amine capped particles showed blue PL at 510 nm. The presence of PL in the GeNPs that were prepared by hydride reducing agents and Zintl salts are still unknown; this might be due to the use of chemicals containing a metal, such as Li, Na, Mg, etc. during their synthesis. However, careful research should be done before making such an assumption.

1.3.4 Applications of GeNPs

Colloidal germanium nanoparticles have been used in the application of optoelectronic devices, biological imaging, and lithium ion batteries.[25]

1.3.4.1 Optoelectronic Applications

Germanium nanomaterials find their use in optoelectronic applications due to their small band gap (0.67 eV in bulk), a high carrier mobility (μ_e = 3900 $cm^2 V^{-1} S^{-1}$, μ_h = 1900 $cm^2 V^{-1} S^{-1}$), a large absorption coefficient (~2 × 10^5 cm^{-1} at 2 eV), and a large exciton Bohr radius (~24 nm).[25] Many research groups have shown optoelectronic applications of GeNPs.

Kortshagen and coworkers[75] synthesized alkyl-GeNPs using a gas phase synthesis in a plasma reactor, followed by thermal hydrogermylation to facilitate colloidal dispersibility. The authors used the particles to fabricate field effect transistors (FETs) by spin coating of GeNPs onto Au/Si/SiO_2 substrates. The device showed conductivities of 10^{-8} S^{-1} in the dark, and 10^{-7} S^{-1} when illuminated. The off-current increased by two orders of magnitude by annealing, with the mobility of 10^{-2} $cm^2 V^{-1} S^{-1}$. On-to-off ratios of FETs of up to 103 were achieved. The authors also generated n-type, ambipolar, or p-type behavior by varying the annealing profiles.

Recently, Liu et al.[76] reported a synthesis of Ge quantum dots (GeQDs) onto a reduced graphene oxide (rGO) to improve the low IR photoresponses of pristine rGO in an IR photodetector. The photocurrent of the device was matched with the absorption properties of GeNPs rather than rGO. In addition, the device showed a high on-off current ratio and a fast response (Figure 1.11). The fast response of the device was attributed to effective charge separation and charge transfer at the interface of GeNPs/rGO. Other researchers also have shown the use of GeNPs in FETs, photodetectors, and solar cells.[76–81]

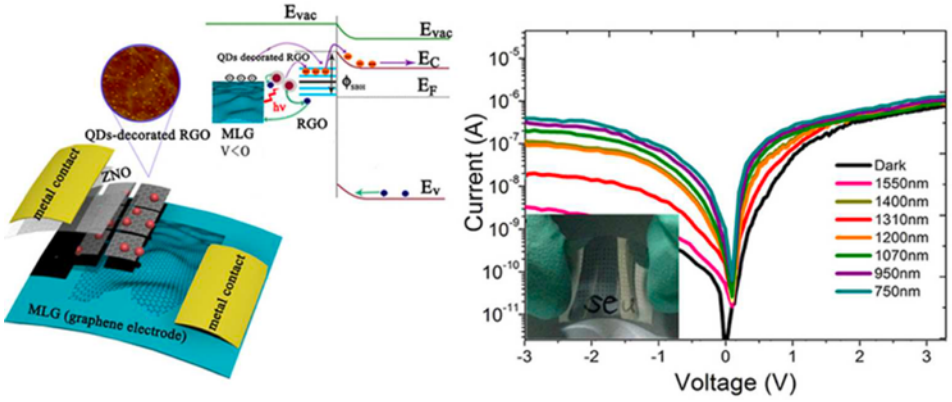

Figure 1.11. Structure schematic of the GeQDs-RGO/ZnO heterostructure photodetector (left) and photocurrent variation of the GeQDs-RGO/ZnO device exposed to different values of incident IR light (right).[76] Reprinted with permission from reference 76. Copyright 2015 American Chemical Society.

1.3.4.2 Lithium-Ion Battery Applications

In recent years, the development of new electrode materials for lithium-ion batteries (LIBs) has shifted to nanomaterials. Germanium nanomaterials are a very attractive choice in LIBs because of their high electrical conductivity, fast lithium ion diffusivity, and a large theoretical capacity (1600 mAh g^{-1}).[82] In addition, germanium nanomaterials offer a superior mechanical stability from volume expansion and pulverization during lithiation and delithiation to the anodes.[83] Germanium nanoparticles and their composite with various carbonaceous materials, e.g., graphene, reduced graphene oxides, carbon nanotubes, carbon nanowires, carbon nanofibers, have shown significant advancement in the capacity and the cycle stability of LIBs.[36,84–100]

Yuan and coworkers[101] synthesized GeNPs on reduced graphene oxide (rGO) sheets by a one-pot heating method and subsequently carbonized them at 500 ºC in a reducing atmosphere (5% H_2/95% Ar) to obtain GeNPs/rGO/C nanocomposites. Galvanostatic performance of the GeNPs/rGO/C anode with a current rate of 0.2 C showed irreversible capacity loss at the first cycle. However, the capacity remained constant after 600 cycles at 1 C after initial capacity loss, and the cycling at 2 C caused only 10% capacity loss; the practical capacity of GeNPs was calculated to be 1332 mAh g^{-1}. A full cell was fabricated using $LiCoO_2$ as a cathode and the GeNPs/rGO/C composite as an anode. The cell showed an excellent capacity of 1000 mAh g^{-1}. Interestingly, the authors also fabricated a commercial aluminum pouch type LIB, which showed a capacity over 20 mAh g^{-1} and was

used to power a scrolling LED display and an electric fan (Figure 1.12). Six parallel connected cells were used to power over 150 LED bulbs (5 mm in size) as well as commercial blue LED arrays.

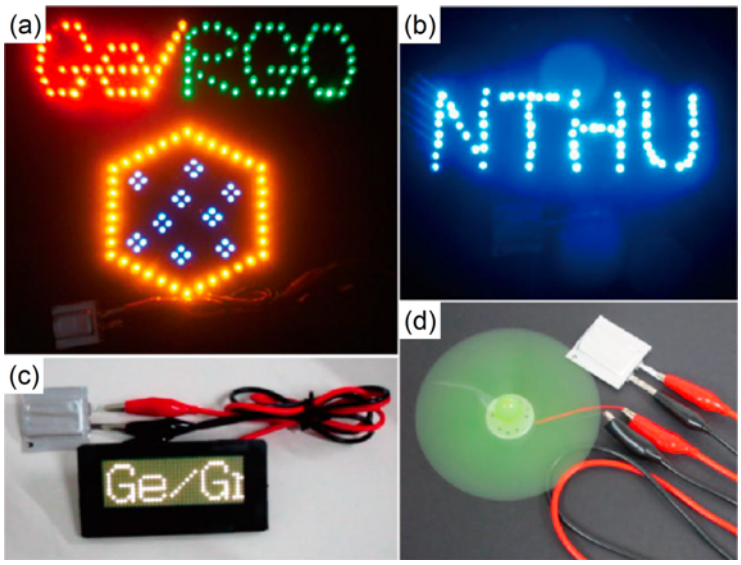

Figure 1.12. GeNPs/rGO/C composite aluminum-pouch-type Li-ion batteries were used to power different electronic devices, including (a) an LED array containing over 150 bulbs, (b) blue LED bulbs, (c) a scrolling LED, and (d) an electric fan.[101] Reprinted with permission from reference 101. Copyright 2014 American Chemical Society.

1.3.4.3 Application in Bioimaging, Cancer Targeting, and Chemical Sensing

One of the attractive applications of semiconductor quantum dots, such as CdSe, is in biological imaging since their surfaces can be rendered biocompatible, and they have size-tunable photoluminescence.[102] However, their toxicity poses serious concerns. Germanium nanoparticles offer the traditional optical properties of quantum dots without the incorporation of toxic elements, such as Cd, Hg, and Pb, and they also offer improvements over molecular dyes, such as stability, signal strength, and lifetime.[40,64]

Boyle and coworkers[103] synthesized hexadecylamine capped colloidal GeNPs with a diameter of 3–5 nm by decomposition of $Ge[N(SiMe_2)_2]_2$ at 300 ºC. GeNPs were rendered water-soluble by carboxy-polyethylene glycol (PEG) phospholipids and were functionalized with carboxyfluorescein-PEG and dinitrophenyl substituted PEG. The carboxyfluorescein group binds with the anti-DNP immunoglobin E (IgE)-cell surface

receptor on the outer surface of rat basophilic leukemia (RBL-2H3) cells and show fluorescence cell imaging capability. The nanoparticles were non-toxic and demonstrated photothermal activity upon excitation by a laser (Figure 1.13a). Similarly, water soluble allylamine capped GeNPs have been used as imaging agents in HepG2 cells and were shown to have relatively low toxicity at a concentration of 100 μg/mL (Figure 1.13b).[40] GeNPs also were subjected to cervical carcinoma (HeLa) cells, and the cell viability was investigated.[16] Nanoparticle concentrations at or below 100 nmol gave a cell viability close to the control experiment and were less toxic then commercially available CdSe/ZnS QDs (Figure 1.13c).

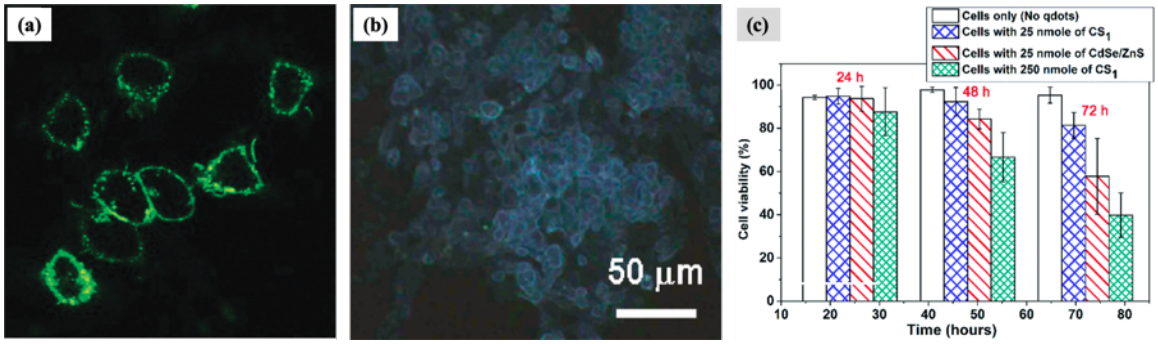

Figure 1.13. (a) Fluorescence microscopy image showing Ge nanoparticles functionalized with carboxyfluorescein-labeled dinitrophenyl groups crosslinking with dinitrophenol-specific IgE antibodies on the surface of the mast cells.[103] (b) Overlay of transmission and fluorescence images of HepG2 cells with hydrophilic allylamine capped Ge nanoparticles transfected into the cytosol.[40] (c) Cell viability of Ge NPs (denoted as CS_1) and comparison with commercial CdSe/ZnS QDs.[16] Reprinted with permission from reference from 103, 40, and 16. Copyright 2007 Wiley-VCH GmbH & Co. KGaA, Weinheim. Copyright 2010 American Chemical Society. Copyright 2016 Royal Society of Chemistry.

Doyle and coworkers[104] applied their blue luminescent water soluble amine-terminated GeNPs as a fluorescent sensor for Fe^{3+}. The authors performed experiments with several metal ions, such as Al^{3+}, Cd^{2+}, Co^{2+}, Cu^{2+}, Fe^{2+}, Fe^{3+}, Hg^{2+}, Mn^{2+}, Ni^{2+}, Pb^{2+}, Pd^{2+}, Pt^{4+}, and Zn^{2+}. Upon exposure to a 50-μM Fe^{3+} solution, the PL of GeNPs decreased by 20%, while the PL decreased by less than 5% for the other metals (Figure 1.14). The limit of detection was observed to be as low as 0.83 μM. Again, the GeNPs could sense Fe^{3+} in tap, river, and lake water despite the presence of contaminants.[104]

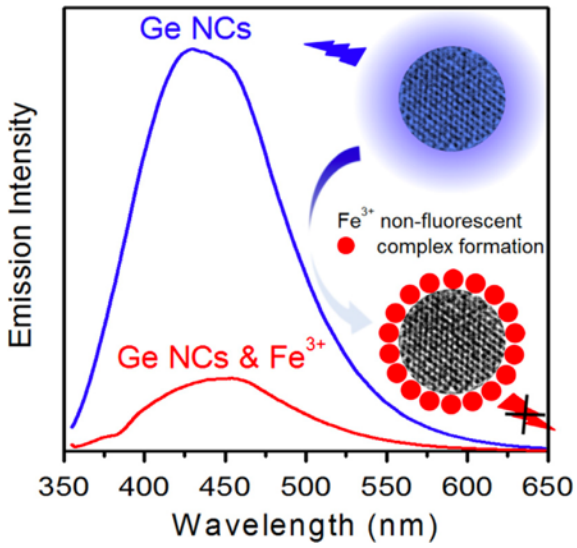

Figure 1.14. Detection of Fe^{3+} ion in water by quenching of the blue luminescent germanium nanocrystals (Ge NCs).[104] Reprinted with permission from reference 104. Copyright 2015 Royal Society of Chemistry.

1.4 Polymer Solar Cells

Utilization of the solar energy has become a very important way forward to meet the world's energy demands. The continuous burning of fossil fuels led to the pollution and the global warming due to the production of CO_2 and other greenhouse gases.[105] World energy consumption is predicted to increase by 28% between 2015 to 2040, with the majority of the projected demand coming from developing countries.[106] Photovoltaics is an established method for the electricity generation, although the high cost and low conversion efficiencies are major drawbacks in the development of solar energy as the primary energy source. Inorganic semiconductor silicon-based solar cells are established and deployed worldwide, but limitations do exist.[107]

Photovoltaic technologies are divided broadly into three generations. The first-generation photovoltaics are based on the crystalline silicon wafers having 15–20% power conversion efficiency (PCE). However, their mass utilization is not viable due to the rigidity of the structure, and their high cost.[108] Second-generation solar cells are based on CdTe, CIGS, etc., which have 10–15% efficiency. The third-generation solar cells are made of semiconductor organic molecules, inorganic nanoparticles or quantum dots, and hybrid organic–inorganic materials; examples are dye-sensitized solar cells (DSSCs),[109] organic solar cells (OSCs),[110] perovskite solar cells,[111] and quantum dot sensitized solar cells

(QDSCs).[112] These solar cells have tremendous potential as an alternative to the silicon solar cells in terms of ease of fabrication and cost, but their main drawback is stability. For example, perovskite solar cells attained 25% efficiency, but they are not stable in the long term and they contain toxic metals that pose environmental threats.[113,114]

Organic solar cells (OSCs), also called polymer solar cells (PSCs), are composed of abundant and non-toxic material. It is possible to produce them in a large scale, low-cost, and roll-to-roll fashion. The efficiency of organic solar cells is increasing steadily over time, with a current highest efficiency of 16%.[115] Therefore, the combination of efficiency enhancement and scalable manufacturing raises the hope that they may serve as an economically viable renewable energy technology.[116–118]

1.4.1 Basic Working Principle of Polymer Solar Cells

In a polymer solar cell, a donor polymer and an acceptor organic molecule form an active layer. The operation of a solar cell involves five physical phenomena: photon absorption, exciton diffusion, exciton dissociation, charge transport, and charge collection.[105] The process of photogeneration and charge transport from a photoactive layer to an external circuit are depicted in Figure 1.15.

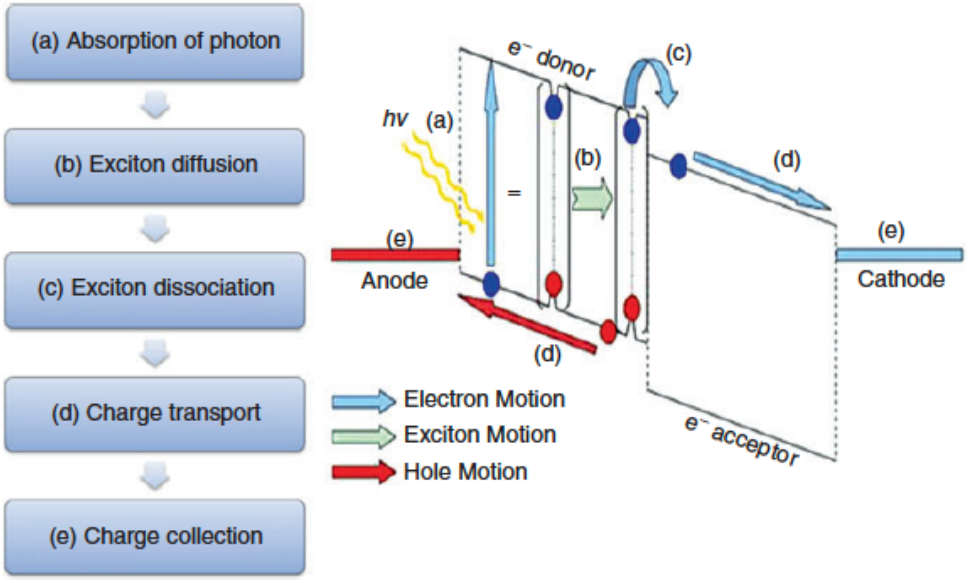

Figure 1.15. The fundamental processes responsible for the photocurrents within a photoactive donor/acceptor layer. The processes involve (a) light absorption and photogeneration of an exciton, (b) exciton diffusion at the donor–acceptor interface, (c) charge separation or exciton dissociation, (d) charge transport to the photoactive layer/electrode interface, and (e) collection of charges by the electrodes.[105] Reprinted with permission from reference 105. Copyright 2018 Springer International Publishing.

At first, an exciton is generated due to the absorption of light by the donor material of an organic solar cell. An exciton is an electrostatically bound electron-hole pair with a binding energy of 1–0.3 eV. Ideally, all photoexcited excitons should reach the dissociation site or the interface of the donor–acceptor. Excitons in semiconducting polymers have a diffusion length of less than 10 nm and recombine (annihilate) rapidly due to their short life.[119,120] Careful combination of the donor and acceptor is required in order for them to dissociate or separate at the interface. Once the exciton has dissociated, the free electrons and holes migrate to the photocathode and photoanode, respectively. Migration of charge occurs due to the driving force gradient in the chemical potentials of the electrons and holes at the donor–acceptor (D-A) junction.[121] The morphology of the semiconducting polymers/molecules plays a vital role during the transport of charge to the respective electrode. After the charge transport occurs, this charge needs to collect effectively in order to get electrical output. The charge collection is sensitive to the electrical contact between the photoactive layer and the electrode and decreases if the interfacial connections are

highly resistive. Ion or metal diffusion into the organic layer,[122] interfacial dipoles at the contact,[123] band bending,[124] and chemical reaction[125] can all influence the injection process.

1.4.2 Polymer Solar Cell Architecture

The simplest polymer solar cell consists of a transparent anode, an organic semiconductor, and a cathode. In such a solar cell, charge separation can occur only at the interface of the organic layer and the contacts (Figure 1.16a). Due to a strong recombination, this architecture shows poor efficiency.[126]

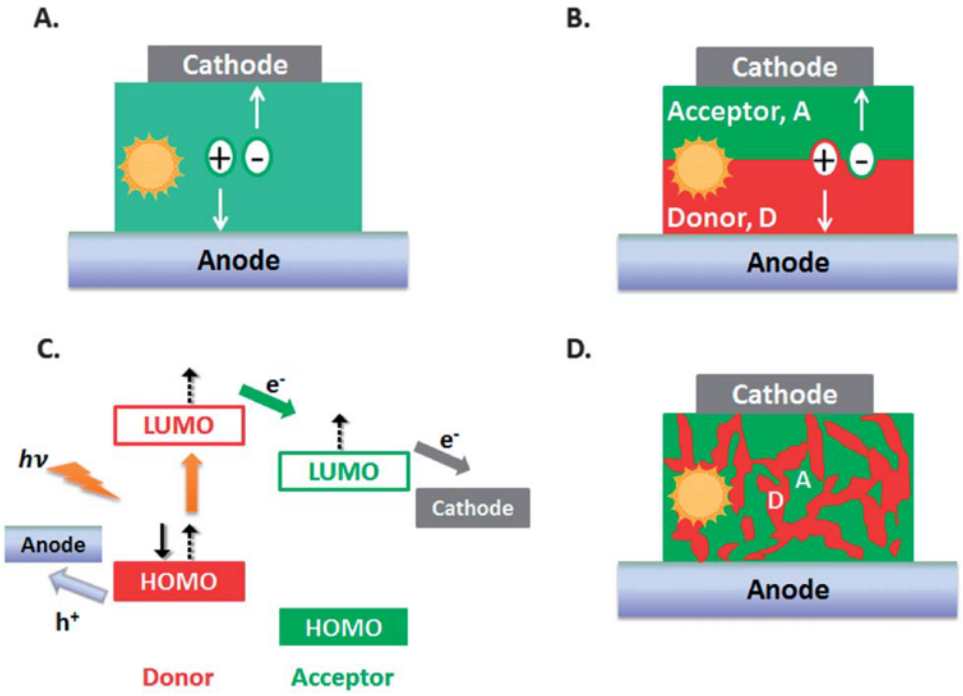

Figure 1.16. Schematic illustration of (A) a single layered organic solar cell, (B) a bi-layer solar cell, (C) exciton dissociation at the donor–acceptor (D-A) heterojunction in an organic solar cell, and (D) a bulk heterojunction solar cell.[126] Reprinted with permission from reference 126. Copyright 2008 Elsevier Inc.

In a bilayer solar cell, a thin layer of an electron donor material is applied on a thin layer of an electron accepting material. The two-component active layer is sandwiched between the anode (donor side) and the cathode (acceptor side). A donor material is a semiconducting polymer that absorbs visible light, and electrons are excited from the highest occupied molecular orbital (HOMO) to the lowest unoccupied molecular orbital (LUMO) level (Figure 16b). An acceptor material should have a lower HOMO and LUMO

level than the donor. Fullerenes are probably the most common acceptor materials studied in organic solar cells. Fullerenes typically show poor optical absorption in the visible spectrum. Thus, the excitons are created mainly in the well absorbing donor polymer, and only the excitons created within the exciton diffusion length from the interface are dissociated. This type of architecture has shown better efficiency than the single layer solar cells due to increased exciton dissociation and reduced recombination issues. However, the overall device efficiency is limited by the exciton diffusion length and the small interfacial area at which exciton dissociation takes place.

The bulk heterojunction (BHJ) solar cell was introduced to overcome the poor efficiencies that arise due to excitons being generated too far from the planar heterojunction. In this structure, an interpenetrating network of donor and acceptor is made by mixing, so that the D-A interface is never far (Figure 16c).[127,128] This facilitates better charge separation and, as a result, better solar cell efficiency. The solution-processed active layer in a BHJ structure ensures low cost of fabrication and simplicity. The donor and the acceptor should be soluble in a common solvent. A solvent has a profound effect on the morphological characteristics of the active layer and, thereby, the opto-electronic properties of the solar cell.[129,130]

1.4.2.1 Forward and Inverted Structure of the BHJ Solar Cells

In a forward solar cell, a D-A blend is sandwiched between a low work function metal cathode and a high work function transparent conducting metal oxide anode. Examples of low work function cathodes are Al, Ca, Ba, and of high work function anodes are indium-tin oxide (ITO) or fluorine-doped tin oxide (FTO).[131–134] The device architecture of a forward OSC is shown in Figure 1.17a.[135] An anode buffer layer, such as poly(3,4-ethylene-dioxythiophene):poly(styrenesulfonate) (PEDOT:PSS), is used to make a smooth surface on an ITO or FTO electrode.[131] However, due to the acidic nature of PEDOT:PSS, ITO etches over time, especially at a high temperature and humidity. Again, it is not possible to do a large-scale roll-to-roll production due to the vacuum evaporation of the top metal electrodes. In addition, vacuum evaporation leaves micropores in the metal electrodes during fabrication, therefore, air and moisture can penetrate the cells and

degrade the polymer active layer.[133] As a result, conventional structured OSC has poor efficiency and low device stability.[134]

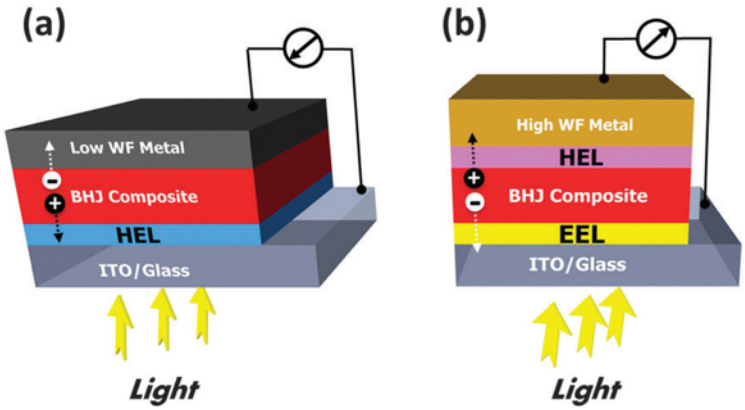

Figure 1.17. Schematic illustration of (a) a forward organic solar cell, and (b) an inverted organic solar cell.[135] HEL is the hole extraction layer and EEL is the electron extraction layer. Reprinted with permission from reference 135. Copyright 2016 Royal Society of Chemistry.

To solve problems associated with forward OSCs, inverted OSCs were developed (Figure 1.17b).[136] In this structure, the ITO or FTO acts as the cathode and the high work function metals act as the anode. Since the polarity of the charge collection is reversed, stable and high work function metals, such as Au, Ag, and Cu, can be used as the anode.[136,137] Therefore, it is possible to print metal anodes instead of costly thermal deposition technologies and also eliminate the use of PEDOT:PSS.[138]

1.4.3 Photoactive Materials

Semiconductor polymers often are used as an active photon absorber in the organic solar cells. Due to the presence of conjugated π-electrons systems that delocalize on the polymer backbone in alternating double- and single-bonds, they become conductive .[139] These types of polymers absorb photons to form excitons resulting from the electron transfer from the HOMO to the LUMO level, which is the key to an organic solar cell.

In the initial stage of OSCs research, small molecules, such as copper pthalocyanine (CuPc), were used as active materials.[140] Research on conjugated polymer systems and their use in organic solar cells became popular in the 1990s. Poly(phenylenevinylene) (PPV) derivatives happened to be the first group of semiconducting polymers. Saricifitci

and coworkers[132] showed that poly[2-methoxy-5-(2-ethylhexyloxy)]-1,4-phenylenevinylene (MEH-PPV) had ultrafast electron transfer to fullerene (C_{60}), which suggested conjugated polymers as electron donors and fullerene derivatives as acceptors. The BHJ structure of MEH-PPV/fullerene interpenetrating network was introduced three years later by Heeger and coworkers.[132] The authors demonstrated a superior efficiency of solar cells compared to bilayer architecture.

The most studied conjugated polymer system that was studied in organic solar cells is probably poly(3-hexylthiophene) (P3HT) derivatives. P3HT derivatives generally were mixed with PCBM (fullerene) derivatives; for example, P3HT:$PC_{61}BM$-based solar cells demonstrated 5% efficiency.[141] The critical factors that lead to high performance devices were identified, which include regioregularity of the polymer, architecture design, addition of processing additives, and post-deposition annealing.[142]

Another group of conjugated polymers studied was low band gap polymers. Low band gap polymers were designed by the donor–acceptor copolymer concept (also called "push–pull"), in which an electron-rich moiety (donor unit) and an electron deficient moiety (acceptor unit) were attached together.[143] It is possible to tune the HOMO and LUMO energy levels by changing the donor and acceptor units. Several low band gap polymers were developed having a high power conversion efficiency, e.g., PCDTBT,[144] PBDTTPD,[145] PTB7,[146] and PTB7-Th.[147] A combination of PTB7-Th donor and $PC_{71}BM$ acceptor showed 10.8% efficiency.[148] Apart from tuning the band gap of the donors and the acceptors, factors that influence the efficiency of a polymer solar cell are the morphology of the donor and acceptor, crystalline orientation of polymers, thermal annealing, and solvent additives.

Although, fullerene-based acceptors were used almost exclusively in OSCs, the development of non-fullerene small molecule acceptor materials gave new light in developing high efficiency OSCs. Fullerenes have a wide gap and are weakly absorbing in the visible region, which prevents complementary light harvesting in acceptor domains.[127] Non-fullerene acceptors are aimed to address those deficiencies by designing low band gap materials.[149,150] Extensive research was performed in developing non-fullerene acceptors. Popular examples are *m*-ITIC,[151] ATT-1,[152] IEICO-4F,[153] IT-M,[154] INIC3,[155] ITIC-Th1,[156]

and IT-4F,[157] all of which demonstrated more than 10% efficiency with combinations of different polymer donors.[150]

1.4.3.1 Role of Interfacial Layer

In BHJ polymer solar cells, an interfacial layer plays an important role in determining the photon-to-electricity conversion, and it is placed between the active layer and the charge collecting electrodes. In a BHJ cell, choosing the proper materials for the interfacial layer is crucial because it can optimize the electrical properties of the BHJ/electrode interface and improve the efficiency of solar cells. Although the polarity of the charge collection is completely opposite in conventional and inverted BHJ solar cells, the photovoltaic processes are the same for both. An ohmic contact between the photoactive layer and the electrodes is needed to minimize the energy barrier. The excitons are generated in the active layer and dissociate at the interface of the donor and acceptor. Then, an interfacial layer can transport a certain charge carrier selectively and block the other one so that only the electrons or the holes can be extracted. Apart from the charge selection, the interfacial layer should possess the following criteria: transparency, efficient charge transport ability, an appropriate energy level to enable ohmic contact, conductivity, good film-forming properties, stability, and low cost.[158,159] Transition metal oxides with a good carrier transport and stability, such as ZnO,[160–163] TiO_2,[164] Cs_2CO_3,[165,166] were used as an electron extraction layer (EEL). For a hole extraction layer (HEL), MoO_3,[167–169] NiO,[170,171] V_2O_5,[172,173] and graphene oxide[174] were applied.

1.4.3.2 Polymer Hybrid Solar Cells

Inorganic semiconductor nanoparticles were utilized as the acceptor materials with a polymer donor in order to fabricate organic–inorganic hybrid solar cells. Several inorganic semiconductor nanoparticles were reported, e.g., CdTe,[175] CdS,[176] CdSe,[177] ZnO,[178] TiO_2,[179] PbS,[180] PbSe,[181] SnO_2,[182] Si,[183] Ge,[81] and $CuInS_2$,[184] to fabricate hybrid solar cells in conjunction with polymer donors.

Liu et al.[185] reported P3HT-Si nanocrystals hybrid solar cells with an efficiency of 1.15%. The reasons why the organic–inorganic hybrid solar cells give low efficiencies are incomplete electron transfer from polymer to nanocrystals and surface traps of nanocrystals

preventing efficient charge transport. Doping of polymer solar cells with inorganic nanocrystals is a very interesting strategy that has been reported. Semiconductor nanoparticles can improve the optical absorption and also enhance the charge transport of a polymer solar cell. Zhao et al.[186] reported an improvement in the efficiency of P3HT:$PC_{61}BM$ solar cells by incorporating Si nanoparticles. The authors obtained a 4.11% efficiency compared to 2.93% (in P3HT-$PC_{61}BM$) by adding 0.05% of Si nanoparticles. Nanoparticles of CuO were utilized in a P3HT-$PC_{70}BM$ solar cell, and 2.96% efficiency was observed, which was 24% higher than the control device.[187] Germanium nanoparticles (GeNPs) also were utilized in P3HT-$PC_{60}BM$ solar cells by Amollo et al.[188] The authors reported an improvement of up to 183% efficiency by incorporating GeNPs/graphene (3 wt% loading) in the device. The improved efficiency was attributed to the effective charge separation and transportation of the nanocomposite in the respective electrodes (Figure 1.18).

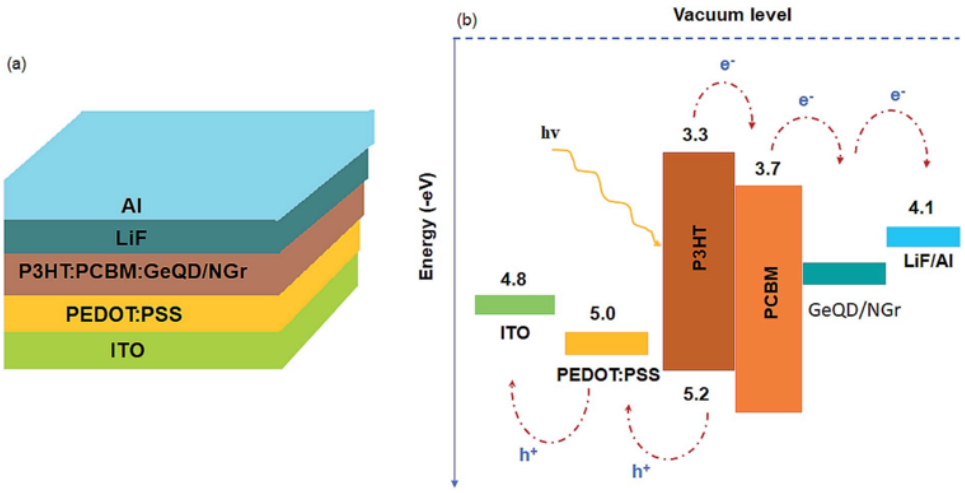

Figure 1.18. (a) Schematic diagram of the BHJ organic solar cell with the GeNPs/nitrogen-doped graphene nanocomposites in the active layer and (b) energy level diagram of the device materials.[188] Reprinted with permission from reference 188. Copyright 2018 Royal Society of Chemistry.

1.5 Scope of this Thesis

Germanium nanoparticles are very attractive due to their unique optoelectronic properties, which make them useful in different applications, such as transistors, lithium-ion batteries, solar cells, and sensors. Therefore, the goals of this thesis were to synthesize germanium

nanoparticles and study new surface reactivity. In this project, heteronuclear dehydrocoupling reactivity was planned to study to by reacting alkylsilanes with the hydride-terminated surface of GeNPs. After that, our goal was to use GeNPs in polymer solar cells as dopant or efficiency enhancer to improve the power conversion efficiency of solar cells. Again, it is important to synthesize GeNPs with uniform size and shapes, because their opto-electronic properties are governed by sizes and shapes. So, in the third project, our aim was to synthesize shape controlled GeNPs by periodic heating and cooling using induction furnace.

Chapter 2 focuses on the synthesis and surface functionalization of GeNPs through dehydrocoupling with alkylsilanes. Three types of long chain alkylsilanes, octadecylsilane, dimethyloctadecylsilane, and hydride-terminated PDMS, were utilized to perform dehydrocoupling with hydride-terminated GeNPs. Their dehydrocoupling reactivity also was compared to their hydrogermylation reactivity, and the products were analyzed to obtain the surface strain due to the presence C or Si on the surface of GeNPs.

Chapter 3 focuses on the utilization of dodecyl-terminated GeNPs as a doping material in a PTB7-Th:IT-4F polymer solar cell. The polymer active layers were characterized by Grazing Incidence Small Angle X-ray Scattering (GISAXS) and Grazing Incidence Wide Angle X-ray Scattering (GIWAXS) to obtain the structural and morphological information of the fabricated films. Inverted structured polymer solar cells were fabricated by blending 0.1–0.9 wt% of GeNPs in the active layers, and the performance of the devices were evaluated.

Chapter 4 describes an attempt to synthesize GeNPs with uniform shape and size by rapid cyclic heating and cooling using an induction furnace.

Chapter 5 summarizes the results of all the projects and proposes possible future research directions.

Chapter 2

Thermally-induced Dehydrocoupling on Germanium Nanoparticles

2.1 Introduction

Germanium nanoparticles (GeNPs) are promising materials that may find use as active systems in far reaching applications, such as solar cells, batteries, field-effect transistors, data storage devices, meta materials, and photodetectors.[25,189,190] Their potential arises partly because bulk germanium has a small band gap (0.67 eV vs 1.1 eV in silicon) and large exciton Bohr radius (~24 nm vs 4.9 nm in silicon) which lead to the influence of quantum confinement being observed in *large* particles when compared to other quantum dot systems.[25] These *larger* nanoparticles are particularly attractive because they should maintain exquisitely tunable properties of nanomaterials while being *more* resistant to deleterious reactions that result from their reduced surface area-to-volume ratio. Still, GeNPs surfaces remain sensitive to air (i.e., oxygen) and moisture that can induce formation of surface oxides.[191,192]

Drawing on the well-established hydrosilylation approaches used to tailor silicon surface chemistry and the perceived similarities of silicon and germanium reactivity, we and others explored hydrogermylation as one approach for modifying the surfaces of bulk and nanoscale Ge.[40,72,191,193–195,51] Despite these early advances, challenges remain, and investigating the surface chemistry of germanium nanomaterials, particularly GeNPs, is of paramount importance if their attractive properties are to be exploited.

Dehydrocoupling (DHC) involves the formal liberation of H_2 upon reaction of two M–H (e.g., M = Si and/or Ge) species, resulting in the formation of an M–M bond; this general reaction has proven to be an effective synthetic tool in Group 14 element molecular chemistry.[196,197] Applications of DHC also have been extended to the modification of bulk and nanoscale Group 14 semiconductor surfaces. Li et al.[198] derivatized bulk silicon wafer and porous-Si surfaces via zirconocene and titanocene catalyzed DHC of surface Si–H moieties; these reactions lead to the introduction of aryl- or alkyl-silanes. We extended

DHC to reactions of organosilanes with H-terminated SiNPs using Wilkinson's catalyst ($(PPh_3)_3RhCl$); unfortunately, the utility of this approach was limited by the material optical properties being compromised by residual Rh impurities.[199] An important step forward was realized when Kim et al.[200] demonstrated that DHC could be thermally-initiated on porous-Si surfaces in the absence of a metal-based catalysts – this advance made it possible to functionalize via DHC while maintaining the substrate photoluminescent response; however, it is important to note that the products of these reactions possessed substantial surface oxide.

Homonuclear DHCs of arylgermanes have been exploited in the preparation of oligo- and poly-germanes,[201] but it has not been applied yet as a strategy for modifying bulk or nanoscale Ge surfaces. Reaching beyond the mere curiosity of whether DHC will provide a viable approach to GeNP surface modification, establishing heteronuclear dehydrocoupling protocols involving germanium nanoparticle surfaces and organosilanes could provide a first step toward preparing heretofore-unknown core shell-like nanostructures of Group 14 elements; it also may provide a method for introducing crystal strain-induced band gap engineering. In this regard, we demonstrate the modification of hydride-terminated GeNPs via the DHC with a series of alkylsilanes.

2.2 Experimental

2.2.1 Reagents and Materials

Germanium dioxide powder (GeO_2, 99.9%) and dimethyloctadecylsilane were purchased from Gelest. Hypophosphorous acid (50 wt% in water), sodium hydroxide pellets, toluene (99.9%, HPLC grade), 1-octadecene (90%), octadecylsilane (97%), hydrogen-terminated poly(dimethylsiloxane) (H-PDMS, average M_n ~580), dodecane (99%), and acetonitrile (99.9%, HPLC grade) were purchased from Sigma-Aldrich. Toluene and acetonitrile were purified using a Pure-Solv purification system and collected immediately prior to use. Hydrochloric acid (36.5–38.0 %) and ammonium hydroxide (28–30%) were purchased from Caledon Labs. Electronics grade hydrofluoric acid (HF, 49% aqueous solution) was purchased from J. T. Baker. Ultrapure H_2O (18.2 MΩ/cm) was obtained from a Barnstead

Nanopure Diamond purification system and was used in all reactions. Molecular sieves (4 Å) were purchased from Sigma-Aldrich and activated in a vacuum oven prior to use. Unless otherwise indicated, reagents were used as received.

2.2.2 Preparation of GeNPs Embedded in Germanium Oxide

GeNPs embedded in a germanium oxide matrix (GeNPs/GeO_x) were prepared using a procedure developed in our laboratory.[51] Briefly, $Ge(OH)_2$ was prepared by dissolving 2.0 g of GeO_2 in 14 mL freshly prepared aqueous NaOH (~17 M). Subsequently, HCl (6 M, 48 mL) was added dropwise to the GeO_2 solution to achieve a pH ~1. Next, hypophosphorus acid in water (50 wt% H_3PO_2; 15 mL) was added and the mixture was refluxed for 5.5 h under static argon. Concentrated NH_4OH (20 mL) was added to the boiling reaction mixture to yield a brown precipitate that was isolated by vacuum filtration and washed three times with 10-mL aliquots of ultrapure water. After drying in a vacuum oven at *ca.* 70 ˚C for 15 h, 1.6 g of 'brown $Ge(OH)_2$' was obtained. This brown powder (1.0 g) was placed in a quartz boat for 1h in a Lindberg Blue tube furnace, whose temperature was ramped to 400 ˚C (18 ˚C/min), under flowing argon (15 mL/min). After cooling to room temperature, a dark brown solid consisting of GeNPs embedded in germanium oxide (GeNPs/GeO_x) was obtained and ground to a fine powder using an agate mortar and pestle. The resulting material (*ca.* 1.0 g) was characterized using X-ray powder diffraction and stored in ambient atmosphere until needed.

2.2.3 Isolation of Hydride-terminated GeNPs

Hydride-terminated GeNPs (H-GeNPs) were liberated from the GeNP/GeO_x via ethanolic hydrofluoric acid (HF) etching using a literature procedure.[51] (**Caution**! HF must be handled with extreme care and in accordance with local regulations.) Briefly, GeNPs/GeO_x (0.2 g) was placed in a polyethylene terephthalate beaker, followed by absolute ethanol (2.0 mL). This mixture was exposed to an ultrasonic bath for approximately 2 min, after which, ultrapure water was added (2.0 mL), and the heterogeneous brown mixture was stirred using a magnetic stir bar/stir plate for 10 min. Subsequently, aqueous HF (49% HF; 2.0 mL) was added. After stirring for 15 min, the liberated H-GeNPs were collected upon extraction into toluene (3×10 mL toluene) to yield a dark brown cloudy dispersion and

were isolated as a brown pellet upon centrifugation at 3000 rpm. The H-GeNPs were re-dispersed in toluene containing activated molecular sieves and stirred. The molecular sieves were removed, and the mixture was centrifuged at 3000 rpm to recover the H-GeNPs (*ca.* 20% mass yield). This process was repeated again, and the obtained H-GeNPs were derivatized immediately using the DHC conditions noted below.

2.2.4 Dehydrocoupling on H-GeNPs Surfaces

The H-GeNPs obtained from etching 0.2 g of GeNP/GeO_x were dispersed in dodecane (5 mL, dried over activated molecular sieves), transferred to a Schlenk flask equipped with a Teflon stir bar, and attached to an argon charged double manifold. Subsequently, 3.5 mmol of the alkylsilane in question and an additional 15 mL dry dodecane were added. The cloudy reaction mixture was subjected to three freeze-pump-thaw cycles and then heated in an oil bath at 180 ˚C for 96 h with stirring. Next, the cloudy crude product mixture was transferred to polytetrafluoroethylene (PTFE) centrifuge tubes, and toluene (3 mL) was used to collect all the samples from the Schlenk flask. Subsequently, acetonitrile (30 mL) was added as an antisolvent. The resulting brown suspension was centrifuged at 12000 rpm for 30 min to yield a brown precipitate and a colorless supernatant. The supernatant was discarded, and the solid was re-dispersed in 5 mL of toluene with sonication to yield a cloudy suspension. Subsequently, acetonitrile (45 mL) was added, and the mixture was centrifuged at 12000 rpm for 30 min to yield a brown solid. This solvent/antisolvent suspension/precipitation procedure was repeated once. Finally, the precipitate (i.e., alkylsilane functionalized GeNPs) was dispersed in 5 mL of dry toluene, and the functionalized GeNPs was stored in a vial at ambient conditions for further use and characterization. It is important to mention that to obtain the optimum conditions for DHC, the reaction mixture was filtered through a 0.45-μ PTFE syringe filter, and better functionalization was evaluated qualitatively by observing the intensity of the amber color.

2.2.5 Hydrogermylation of H-GeNPs Surfaces

An established literature procedure was employed to modify GeNP surfaces via thermally-induced hydrogermylation.[51] These materials provide a baseline for comparison with functionalized GeNPs obtained from DHC reactions. Briefly, H-GeNPs liberated from the

identical GeNP/GeO_x were mixed with neat 1-octadecene (10 mL) and heated in an oil bath at 180 ˚C for 96 h with stirring. The resulting octadecyl-terminated GeNPs were purified and stored using the identical procedure outlined for the DHC products.

2.2.6 Materials Characterization and Instrumentation

Fourier Transform Infrared spectroscopy (FTIR) was performed using a Nicolet Magna 750 IR spectrophotometer for samples prepared via drop casting from a toluene suspension onto a silicon wafer.

Proton nuclear magnetic resonance spectroscopy (^{1}H NMR) was performed using a Varian Unity Inova Console 500 MHz NMR spectrometer. The signals were calibrated in MestReNova version 9.0.1-13254 using a TMS (0 ppm) standard. Samples were prepared such that they contained a few milligrams of GeNPs in 0.03% TMS in 0.6 mL $CDCl_3$.

A Renishaw inVia Raman microscope equipped with a 633-nm diode laser was used with 50% power to obtain Raman spectra. Samples were prepared by drop casting of a suspension on to a gold coated glass slide.

X-ray Diffraction was performed using a Rigaku Ultima IV equipped with a Cu-Kα radiation source (λ = 1.54 Å) using thin film stage. The $Ge(OH)_2$ and GeNP/GeO_x samples were prepared by putting powder on to a 10×10 mm^2 Si (100) wafer. Functionalized GeNPs samples were prepared by drop casting on to a 10×10 mm^2 Si (100) wafer. The XRD results were analyzed by a TOPAS Academic software package.[202]

X-ray photoelectron spectra were obtained in energy spectrum mode at 210 W using a Kratos Axis Ultra X-ray photoelectron spectrometer. The X-ray source was Al Kα (1486.6 eV). Samples were prepared onto a copper foil (5×5 mm^2) substrate. CasaXPS (Version 2.3.13) was used to calibrate binding energies using the C 1s peak as a reference (284.8 eV). The C 1s region was fit/deconvoluted to determine the amount of oxide arising from adventitious carbon. The Ge 3d region of the XPS was fit to Ge $3d_{3/2}$ and Ge $3d_{5/2}$ partner lines with spin-orbit splitting fixed at 0.58 eV and intensity ratio at 0.67. The Si 2p region was fit to Si $2p_{1/2}$ and $2p_{3/2}$ partner lines with spin-orbit splitting at 0.6 and intensity ratio at 0.5. A Shirley type background was applied to deconvolute the data, and the background was subtracted after deconvolution.

Bright-field transmission electron microscopy (TEM), high-resolution TEM (HRTEM), and energy dispersive X-ray (EDX) were performed in JEOL JEM-ARM200CF equipped with a cold field emission gun (cFEG) having an accelerating voltage of 200 kV. High angular annular dark field (HAADF) image and electron energy loss spectroscopy (EELS) were gained in scanning mode with a nominal electron probe size of 0.5 nm using JEOL 2200 FS TEM/STEM. TEM samples were prepared by drop-coating 1–2 drops of dilute toluene suspension containing GeNPs onto a holey carbon coated copper grid (150 mesh, Electron Microscopy Science), and the solvent was removed by using filter paper under the grid. Bright-field TEM and HRTEM images were processed using ImageJ software (version 1.51j8), and at least 300 particles were measured to obtain size distributions of GeNPs.

Dynamic light scattering (DLS) data was obtained using a Malvern Zetasizer Nano S series, dynamic light scattered with a 633-nm laser. All the toluene suspentions containaing GeNP samples were equilibrated to 25 ℃ prior to data acquisition and scanned three times.

2.3 Results and Discussion

Oxide-embedded germanium nanoparticles (GeNPs/GeO_x) were prepared using procedures developed in our laboratory that exploit the thermal disproportionation of $Ge(OH)_2$.[51] Subsequent removal of the protective oxide matrix provided hydride-terminated GeNPs (H-GeNPs) that served as substrates for DHC and the hydrogermylation reactions investigated here (Scheme 2.1).

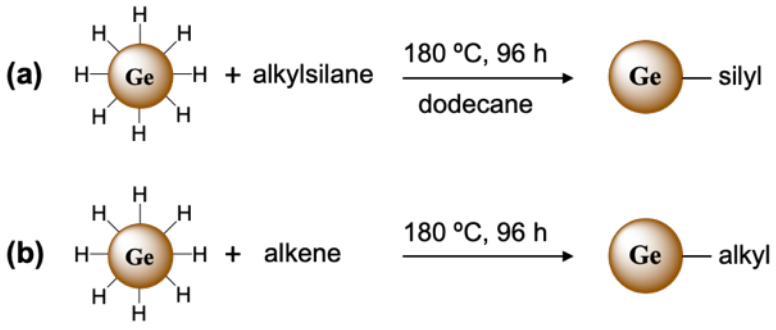

Scheme 2.1. Protocols for functionalizing hydride-terminated Ge nanoparticles via (a) dehydrocoupling, and (b) hydrogermylation.

Briefly, H-GeNPs that were extracted from HF were washed with toluene and dried over molecular sieves. Then, they were mixed with dodecane and the alkylsilane of interest in a Schlenk flask for DHC reaction and subjected to three freeze-pump-thaw cycles. Subsequently, they were heated at 180 ˚C for 96 h under an Ar atmosphere with stirring. For hydrogermlyation, the washed and dried H-GeNPs were mixed with 1-octadecene, allowed to freeze-pump-thaw, and then allowed to react under the same conditions mentioned above.

To evaluate the effective surface functionalization, octadecylsilane was chosen as the model substrate for optimization of the reaction time and temperature. The extent of the reaction progress was determined qualitatively based upon the intensity of the amber color of the PTFE (0.45 μ) filtered reaction mixture for T = 80, 130, and 180 °C (Figure 2.1a) and t = 24, 48, and 96 h (Figure 2.2a).

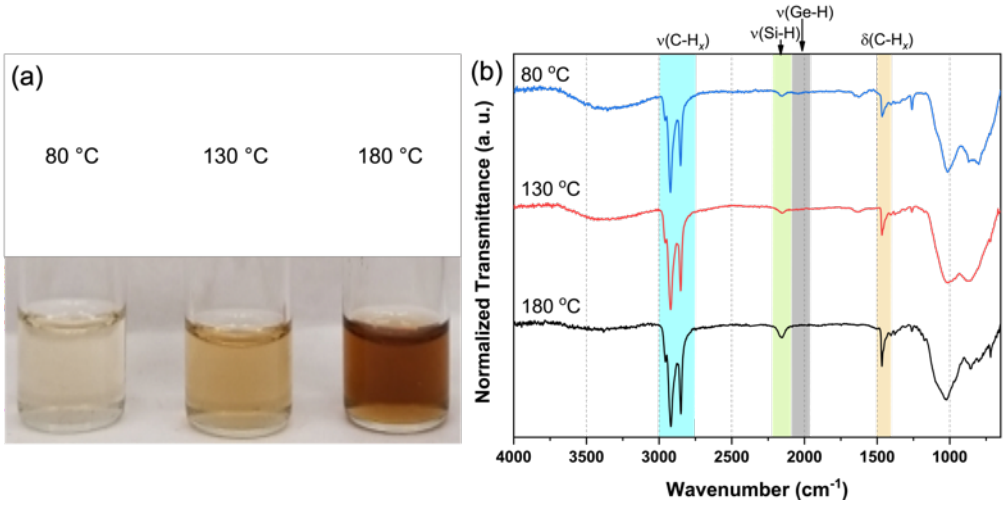

Figure 2.1. (a) Photograph of unpurified filtered samples and (b) FTIR of purified octadecylsilyl-GeNPs samples obtained by reactions at the indicated temperatures for 48 h.

Reaction mixtures obtained from higher temperatures and longer times (at T = 180 °C, t = 96 h) appear more intensely colored, consistent with more effective functionalization. In all cases, the FTIR features of octadecylsilyl-GeNPs at *ca.* 2960–2850 cm^{-1}, *ca.* 1464 cm^{-1}, and *ca.* 2157 cm^{-1} are associated with C–H$_x$ stretching, C–H$_x$ bending, and Si–H stretching, respectively (Figure 2.1a and Figure 2.2b). The O–H on the surface is believed to result from oxidation occurring during the purification using acetonitrile while GeNPs surfaces are poorly functionalized. In Figure 2.1b, we observe that

octadecylsilyl-GeNPs have the feature associated with Ge–H (*ca.* 2015 cm^{-1}) at 80 °C, which disappears when the reaction was performed at 130 and 180 °C. Also, the broad O-H stretching frequency at *ca.* 3300–3400 cm^{-1} diminishes when the reaction was performed at higher temperature. Again, by comparing the reaction times of 24, 48, and 96 h, we observe the disappearance of the feature associated with Ge–H and O–H stretching at longer reaction times, which implies better functionalization (Figure 2.2b).

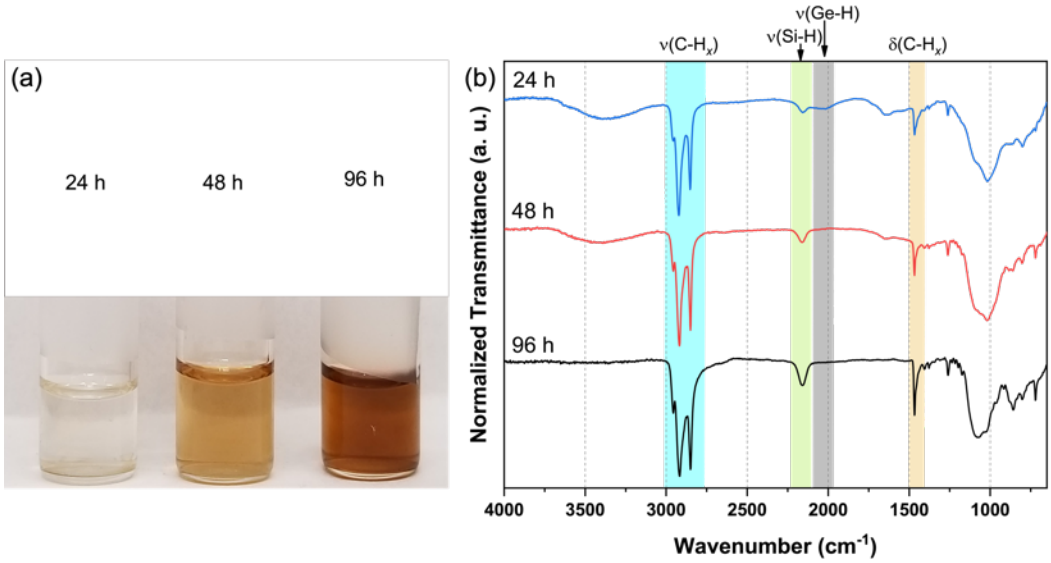

Figure 2.2. (a) Photograph of unpurified filtered samples and (b) FTIR of purified octadecylsilyl-GeNPs samples obtained by reactions at 180 °C for the indicated times.

After optimizing the reaction time and temperature, we chose octadecylsilane, dimethyloctadecylsilane, and H-PDMS as silane ligands to present the versatility of the DHC reaction. Hydrogermylation also was employed using 1-octadecene to compare with the DHC reactions. The FTIR of H-GeNPs, octadecyl-GeNPs, octadecylsilyl-GeNPs, dimethyloctadecylsilyl-GeNPs, and H-PDMS-GeNPs is shown in Figure 2.3. The spectra give insight into the surface species on GeNPs. The spectrum obtained for H-GeNPs shows two distinctive absorptions at *ca.* 2009 and *ca.* 843 cm^{-1} arising from Ge–H stretching and bending vibrations, respectively. Following the hydrogermylation and DHC reaction, the Ge–H features are no longer evident and are replaced by intense absorptions at *ca.* 2960–2850 cm^{-1} and *ca.* 1469 cm^{-1} attributed to C-H_x stretching and bending modes, respectively,

of the aliphatic chain of ligands.[203] The feature at *ca.* 2161 cm^{-1} is associated with Si–H bonds in octadecylsilyl-GeNPs.

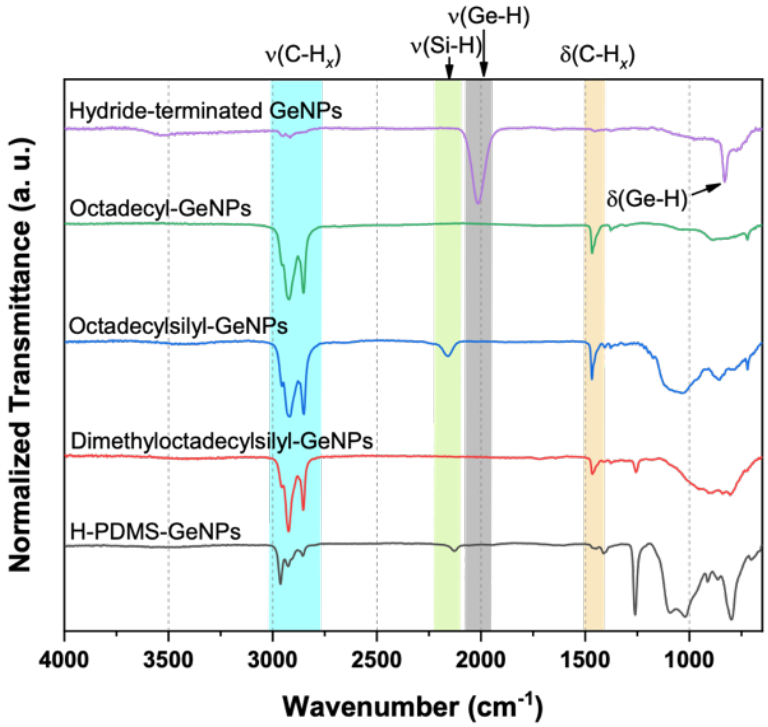

Figure 2.3. FTIR spectra of hydride-terminated GeNPs, octadecyl-GeNPs, octadecylsilyl-GeNPs, dimethyloctadecylsilyl-GeNPs, and H-PDMS-GeNPs.

For dimethyloctadecylsilyl-GeNPs, no feature associated with Si–H was observed, which supports the functionalization. The H-PDMS-GeNPs are showing a small feature of Si–H at *ca.* 2122 cm^{-1} that was expected due to the presence of two Si–H in terminal position of polymer. FTIR spectra of the ligands are given in Figure 2.4 for comparison.

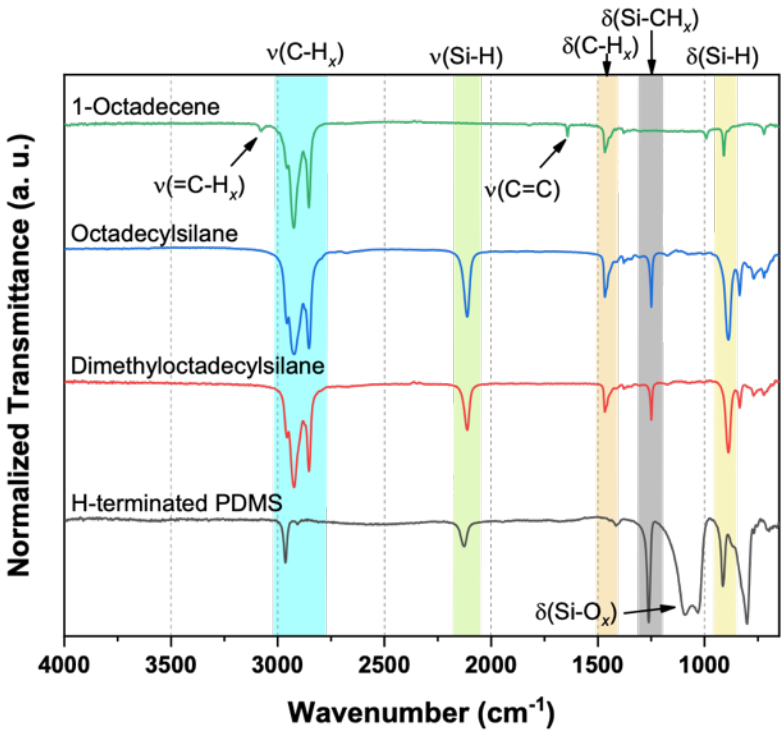

Figure 2.4. FTIR spectra of 1-octadecene, octadecylsilane, dimethyloctadecylsilane, and H-PDMS.

The Raman spectra of alkyl/alkylsilane functionalized GeNPs show strong phonon absorption at *ca.* 299 cm^{-1} that is attributed to a Ge−Ge modes (Figure 2.5).[204] It is documented in the literature that a Ge–Si optical phonon is expected to appear around 400 cm^{-1} in the SiGe alloy.[205] However, one layer of Si–Ge bond may not provide enough signal to detect. The Raman spectrum of crystalline-Ge (*c*-Ge) was shown for comparison. The shoulder observed from functionalized GeNPs suggests the presence of amorphous GeNPs, consistent with presented XRD data (see below).[204]

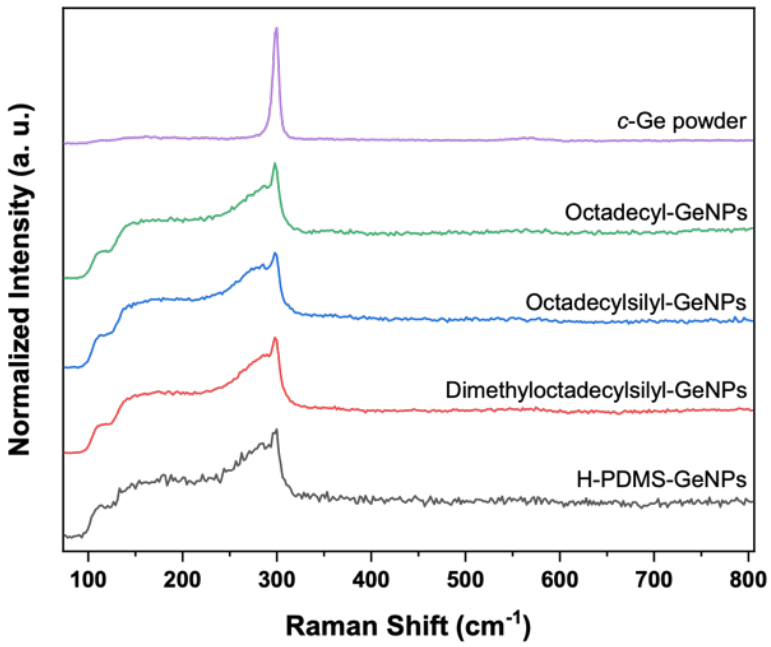

Figure 2.5. Raman spectra of *c*-Ge powder, octadecyl-GeNPs, octadecylsilyl-GeNPs, dimethyloctadecylsilyl-GeNPs, and H-PDMS-GeNPs.

Proton nuclear magnetic resonance (^{1}H-NMR) spectroscopy provides insight into the nature of the GeNPs surface species. In this context, ^{1}H-NMR of octadecyl-GeNPs (Figure 2.6*(i)*) shows a set of broad resonances arising from terminal methyl protons (centered at δ = 0.88 ppm), and methylene chain protons (in the range of δ = 1.1–1.5 ppm). The integration ratios of the terminal methyl to the methylene chain protons signals were determined to be 3:32.36, respectively, which are consistent with the expected surface octadecyl moiety.

The octadecylsilyl-GeNPs (Figure 2.6*(ii)*) shows terminal methyl protons at 0.88 ppm, Si adjacent methylene protons at 0.6 ppm, and methylene protons at 1.1–1.6 ppm (integration ratios 3:2.58:24.94). It is important to mention that in octadecylsilane, this silane proton shows a resonance at 3.48 ppm (Figure 2.7), which may have shifted to 4.6 ppm when it is attached to GeNPs. In the case of dimethyloctadecylsilyl-GeNPs (Figure 2.6*(iii)*), no silane proton was observed when attached to GeNPs; it appeared at 3.88 ppm before the reaction consistent with functionalization. The integration ratios of terminal methyl (at δ = 0.88 ppm), to methylene chain (δ = 1.1–1.6 ppm), to silicon adjacent methylene (δ = 0.56 ppm), to silicon adjacent methyl (δ = 0.096 ppm) protons were determined to be 3:31.38:1.89:5.08, respectively. For H-PDMS-GeNPs (Figure 2.6*(iv)*),

there was still a resonance from the silane proton due to the presence of two terminal Si–H in the ligand, however, measuring the intensity ratios does not give meaningful information.

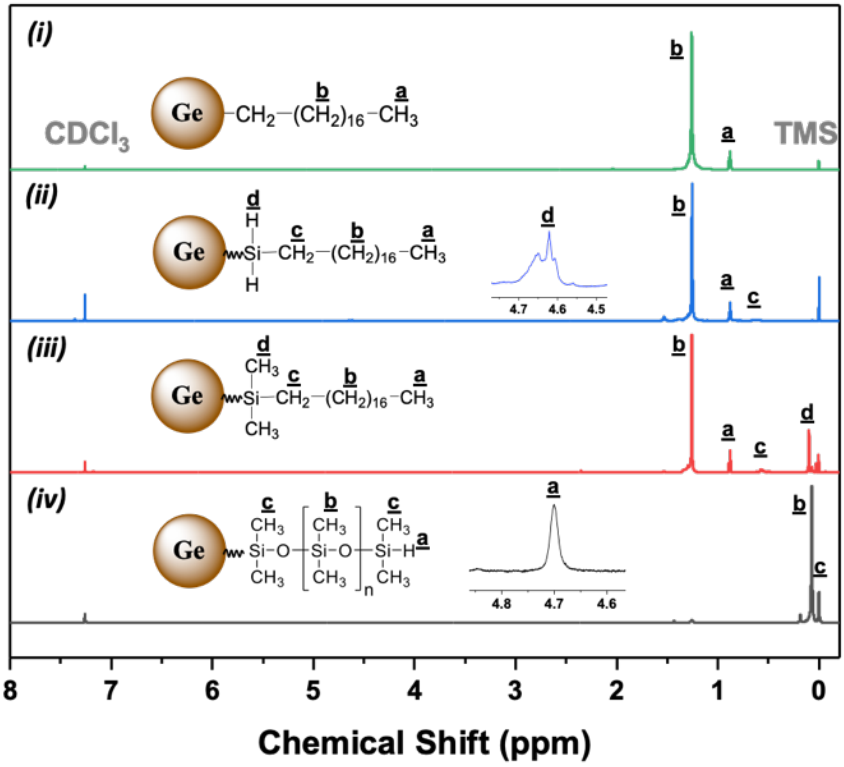

Figure 2.6. ^{1}H-NMR of *(i)* octadecyl-GeNPs, *(ii)* octadecylsilyl-GeNPs, *(iii)* dimethyloctadecylsilyl-GeNPs, and *(iv)* H-PDMS-GeNPs in $CDCl_3$ (7.2 ppm) solvent with 0.03% TMS (0.0 ppm).

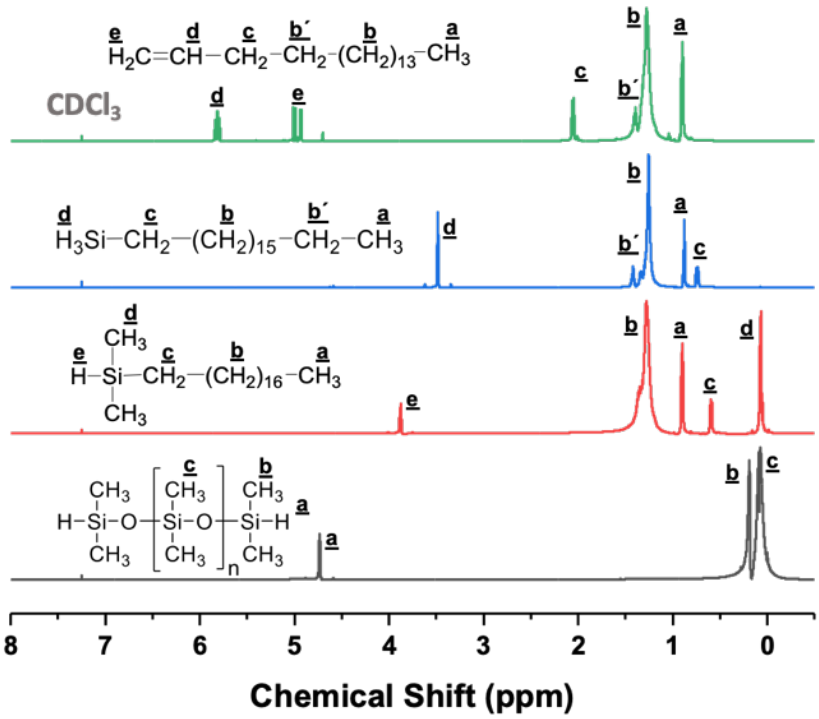

Figure 2.7. ^{1}H-NMR of (from top) 1-octadecene, octadecylsilane, dimethyloctadecylsilane, and hydride-terminated PDMS in $CDCl_3$ (7.2 ppm) solvent.

The functionalized GeNP samples, reactants, and intermediate materials were analyzed with powder X-ray diffraction. To take into account the contribution from zero-background Si-wafer holders, empty holders were evaluated, and some characteristic peaks were observed. Empty holders showed broad reflections at 20.24°, 51.27°, 55.23°, 79.3° and a sharp reflection at 53.56° on the sample holder for $Ge(OH)_2$, the GeNPs/GeO_x composite (Figure 2.8a), and all sample holders for octadecyl-GeNPs, octadecylsilyl-GeNPs, dimethyloctadecylsilyl-GeNPs, and H-PDMS-GeNPs (Figure 2.8b). All the reflections from sample holders have been taken into account as background for sample analysis. More specifically, in addition to six polynomial backgrounds, a function of the sample holder background parameters and peak positions with their intensities of sample holders were added.

The sample containing amorphous $Ge(OH)_2$, which was prepared by reducing GeO_2 using hypophosphorus acid, shows a broad feature. The sample containing GeNPs/GeO_x composite shows phases, Ge (a = 5.64 Å cell parameter, and 7.6 nm particle size) and amorphous GeO_2 (a = 5.05 Å and c = 5.37 Å). The fit is shown on Figure 2.8a.

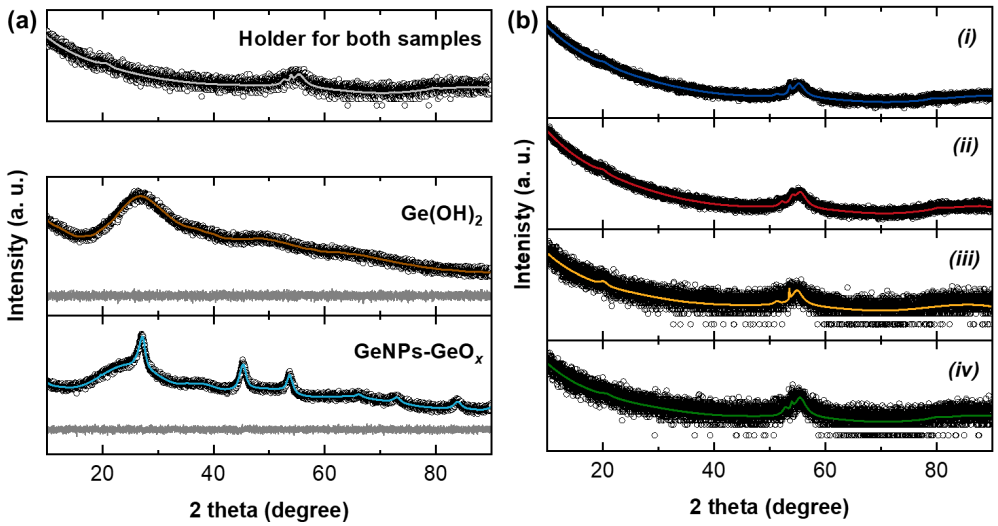

Figure 2.8. X-ray Diffraction of (a) sample holder for $Ge(OH)_2$ and GeNPs/GeO_x, $Ge(OH)_2$, and GeNPs/GeO_x composite and (b) sample holders for *(i)* octadecyl-GeNPs, *(ii)* octadecylsilyl-GeNPs, *(iii)* dimethyloctadecylsilyl-GeNPs, and *(iv)* H-PDMS-GeNPs.

The alkyl/alkylsilane functionalized GeNPs samples were analyzed with diffraction line-broadening methods to determine the size of crystallites and strain from X-ray powder diffraction data (Figure 2.9a). After refining the reference, instrument parameters and peak shape values were fixed, and line broadening was assumed to result only from physical features. Size determination from diffraction data were analyzed with integral breadth, fwhm, and Lorentzian/Gaussian broadening methods. All the methods assume a normal distribution of spherical crystallites. Strain broadening analysis was performed, and the strain value as defined by Stokes and Wilson was refined.[206,207] Table 2.1 lists the crystallite sizes/integral breadths of 5.92, 6.52, 7.43, and 7.83 nm for octadecyl-GeNPs, octadecylsilyl-GeNPs, dimethyloctadecylsilyl-GeNPs, and H-PDMS-GeNPs, respectively. The alkyl-GeNPs show a smaller strain component than alkylsilane-GeNPs. Again, the dimethyloctadecylsilyl-GeNPs and H-PDMS-GeNPs exhibit larger strain than octadecylsilyl-GeNPs.

The reflections at 27.09°, 45.30°, 53.65°, 65.91°, 72.84°, and 83.65° correspond to cubic germanium 111, 220, 311, 400, 331, and 422 planes, respectively (Figure 2.9a, PDF# 04-0545).[208] For octadecyl-GeNPs, two weak reflections at 19.58° and 21.27° were observed. A broad reflection at 21.31° was observed for octadecylsilyl-GeNPs. To identify

the origin of this reflection, an XRD of octadecylsilane (melting point 28 ˚C) was carried out, and a reflection was found at the same 2-theta position (Figure 2.9b).

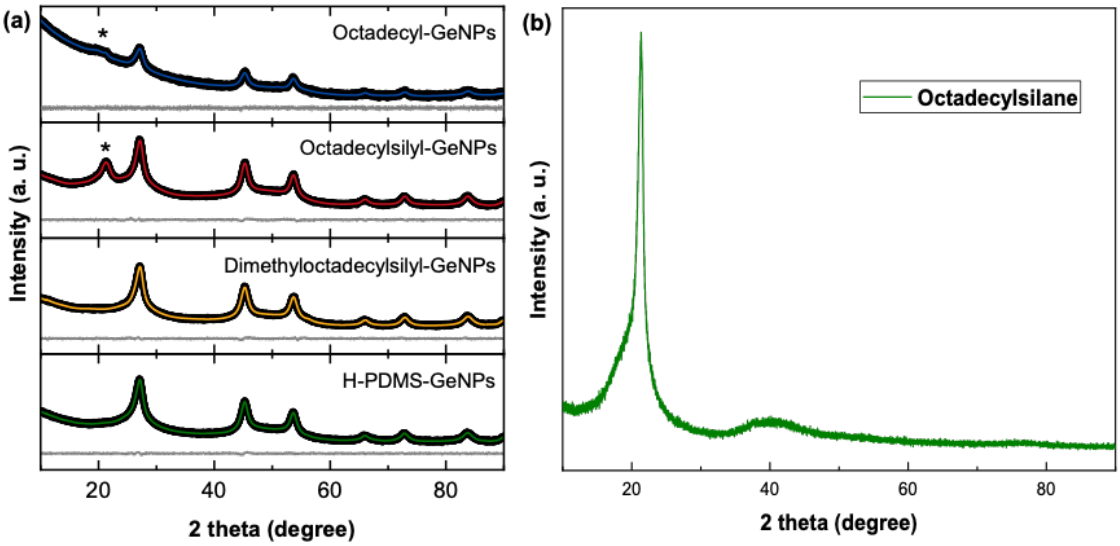

Figure 2.9. X-ray Diffraction of (a) octadecyl-GeNPs, octadecylsilyl-GeNPs, dimethyloctadecylsilyl-GeNPs, and H-PDMS-GeNPs, and (b) octadecylsilane.

Table 2.1. Crystallographic Refinement Data for GeNP Samples

Sample	Octadecyl-GeNPs	Octadecylsilyl-GeNPs	Dimethyl-octadecylsilyl-GeNPs	H-PDMS-GeNPs
Space group	$Fd\bar{3}m$ (No. 227)	$Fd\bar{3}m$ (No. 227)	$Fd\bar{3}m$ (No. 227)	$Fd\bar{3}m$ (No. 227)
a (Å)	5.6515(6)	5.6539(2)	5.6522(2)	5.6561(4)
T (K)	296	296	296	296
Radiation	Cu Kα, λ=1.5406 Å	Cu Kα, λ=1.5406 Å	Cu Kα, λ=1.5406 Å	Cu Kα, λ=1.5406 Å
2θ limits	10.00–80.00°	10.00–80.00°	10.00–80.00°	10.00–80.00°
Refinement method	Pawley	Rietveld	Rietveld	Rietveld
No. of data collected	4117 data points	4117 data points	4117 data points	4117 data points
No. of Bragg reflections	7	7	7	7
No. of variables	26	26	26	26
Residuals[a]	R_{wp} = 0.0468 R_{exp} = 0.0455	R_{wp} = 0.0289 R_{exp} = 0.0249	R_{wp} = 0.0355 R_{exp} = 0.0309	R_{wp} = 0.0322 R_{exp} = 0.0298
Goodness of fit	1.02	1.12	1.14	1.08
Synthetic peaks	19.58° 21.27°	21.31°	24.19°	24.19°
Integral breadth size	5.9(2) nm	6.5(2) nm	7.4(3) nm	7.8(3) nm
Strain, e_0	0.00016(2)	0.00082(3)	0.00131(4)	0.00155(4)

[a] $R_{wp} = \left[\sum[w(y_o - y_c)]/\sum w y_o^2\right]^{1/2}$ $R_{exp} = [(N\text{-}P+C)/\Sigma(wy_o^2)]^{1/2}$; $R_{wp} = [\Sigma[w(y_o - y_c)] / \Sigma wy_o^2]^{1/2}$; N is the total number of observations, P is the number of parameters refined, C is the number of constraints used in the refinement.

The survey X-ray photoelectron (XP) spectra of octadecyl-GeNPs confirms the presence of Ge, C, and O (Figure 2.10), and all the alkylsilane functionalized GeNPs confirm the presence of Ge, Si, C, and O. The percentage of each element calculated from survey XPS is given in Table 2.2. The amount of Ge compared to C species is very low for the octadecyl-GeNPs and octadecylsilyl-GeNPs, which can be attributed to greater surface coverage as evidenced by ^{1}H-NMR (see below). In the dimethyloctadecylsilyl-GeNPs and H-PDMS-GeNPs, the amount of Ge is greater compared to previous samples, consistent with poor surface coverage by organic surface groups.

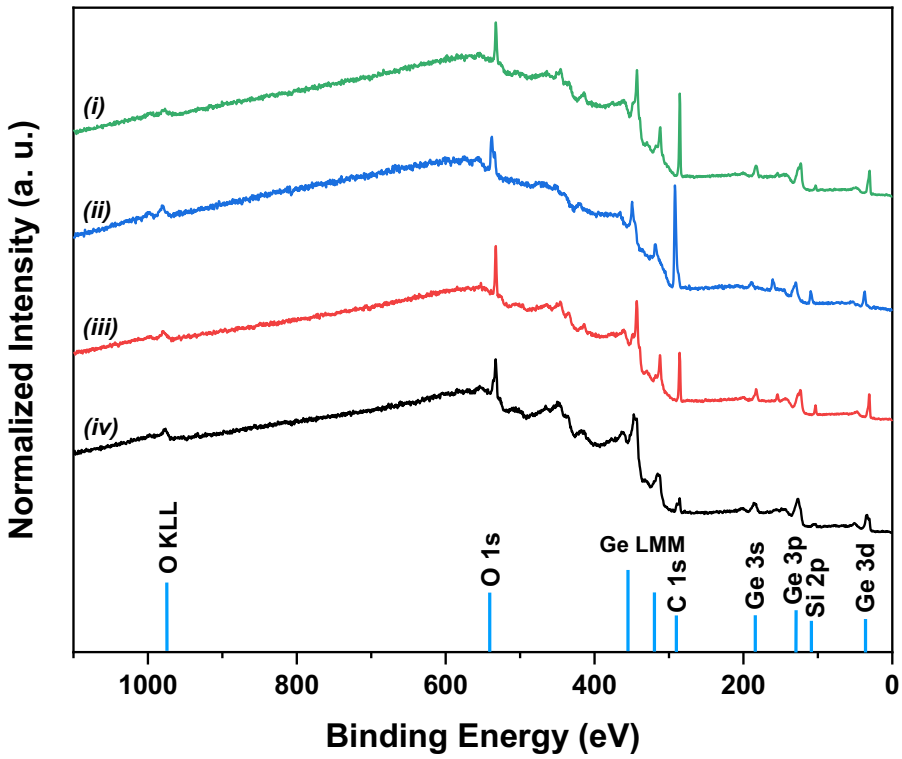

Figure 2.10. Survey XP spectra of *(i)* octadecyl-GeNPs, *(ii)* octadecylsilyl-GeNPs, *(iii)* dimethyloctadecylsilyl-GeNPs, and *(iv)* H-PDMS-GeNPs.

Table 2.2. Percentage of Element in the DHC Samples

Sample	C 1s	O 1s	Ge 3p	Si 2p
Octadecyl-GeNPs	69.17%	15.61%	15.22%	-
Octadecylsilyl-GeNPs	75.24%	13.99%	6.39%	4.43%
Dimethyloctadecylsilyl-GeNPs	52.90%	19.93%	18.73%	8.45%
H-PDMS-GeNPs	29.25%	23.23%	39.95%	7.56%

The high-resolution XP spectra of the Ge 3d region of all samples (Figure 2.11) were fitted/deconvoluted to the $3d_{5/2}$ and $3d_{3/2}$ spin-orbit couple with a binding energy *ca.* 29.6 eV and 30.1 eV for elemental and surface Ge(0,I), along with some partial oxidation at *ca.* 31.4, and 32.7 eV, which are attributed to the suboxides (GeO_x, $0 < x \leq 2$).[209] Small shifts towards higher binding energy (up to 0.3 eV) were observed for alkylsilane functionalized GeNPs compared to alkyl-GeNPs. However, this is not surprising since adventitious C 1s was used as the calibration standard, which can induce an error of ±0.3

eV.[210–212] The Si 2p region of the high-resolution XP spectrum (Figure 2.11) is fitted to the $2p_{1/2}$ and $2p_{3/2}$ spin-orbit couple, with a binding energy of *ca.* 102.1 and 102.6 eV, respectively, and can be attributed to alkylsilane attached to GeNPs.[213] The C 1s region also was fitted to obtain the amount of oxide from adventitious carbon (Figure 2.12, Table 2.3). A small portion of oxygen in the present GeNPs samples can be attributed to adventitious carbon species, but the majority of the oxygens are from functionalized GeNPs.

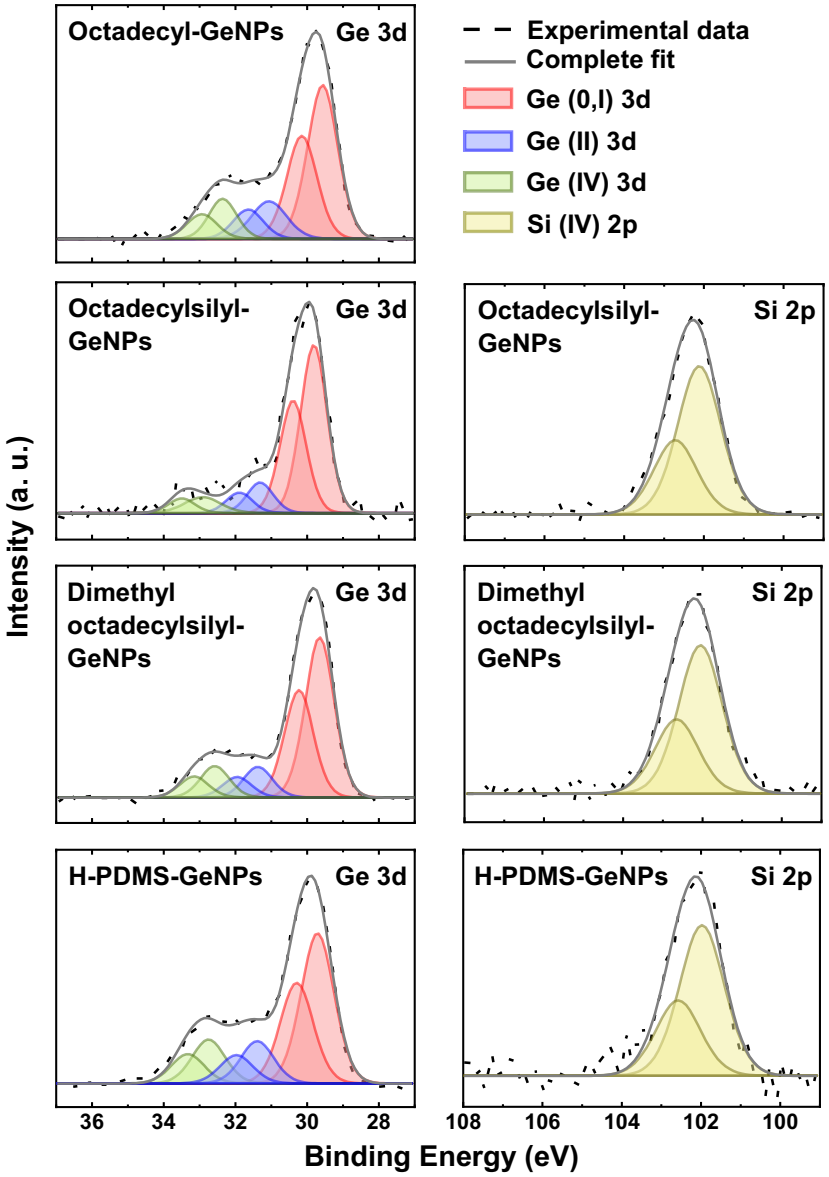

Figure 2.11. High-resolution XP spectra of Ge 3d and Si 2p in alkene and alkylsilane functionalized GeNPs.

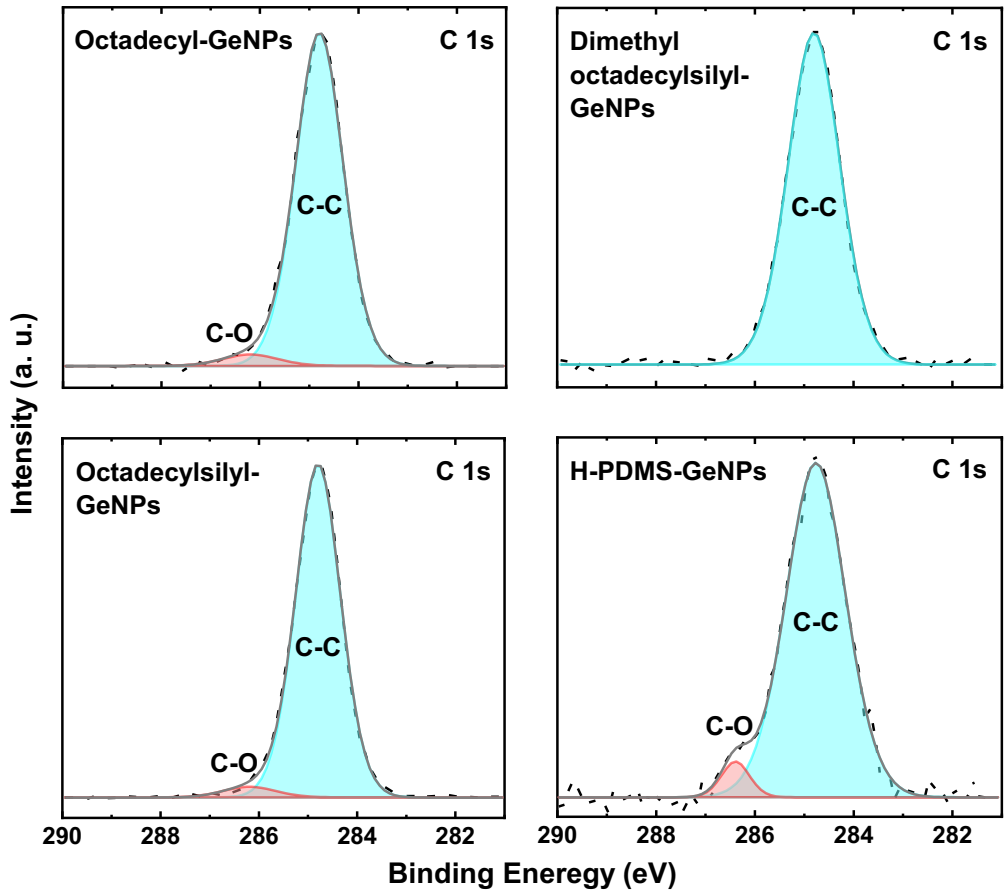

Figure 2.12. High Resolution XP spectra of C 1s of octadecyl-GeNPs, octadecylsilyl-GeNPs, dimethyloctadecylsilyl-GeNPs, and H-PDMS-GeNPs (black dashed line = experimental data, gray solid line = complete fit, blue = C–C, red = C–O).

Table 2.3. Percentage of Oxide in C 1s in DHC Samples

Sample	C–C	C–O
Octadecyl-GeNPs	96.15%	3.85%
Octadecylsilyl-GeNPs	96.3%	3.63%
Dimethyloctadecylsilyl-GeNPs	100%	-
H-PDMS-GeNPs	95.20%	4.80%

Direct evaluation of oxide-embedded GeNPs using electron microscopy is impractical, however, inspection of liberated functionalized GeNPs is informative. TEM and HRTEM give insight into the morphology and local crystallinity of the functionalized NPs. Figure 2.13 shows representative brightfield TEM and HRTEM images of octadecyl-GeNPs, octadecylsilyl-GeNPs, dimethyloctadecylsilyl-GeNPs, and H-PDMS-GeNPs. The

GeNPs are shaped randomly and exhibit an average diameter (taken as the longest dimension) of 7.93 ± 1.28 nm for octadecyl-GeNPs and 7.70 ± 1.08 nm for octadecylsilyl-GeNPs. The size distributions of the particles, measured by average shifted histogram (ASH),[214] show fairly broad distributions (Figure 2.13(e-f)). It was not possible to measure the size of the dimethyloctadecylsilyl-GeNPs and H-PDMS-GeNPs because they were aggregated, suggesting crosslinking. The hydrodynamic radius of all the particles measured, using Dynamic Light Scattering (DLS), is 23 and 29 nm for octadecyl-GeNPs and octadecylsilyl-GeNPs, respectively. In contrast, the hydrodynamic radius of dimethyloctadecylsilyl-GeNPs and H-PDMS-GeNPs is 335 and 375 nm, respectively, (Figure 2.14); these are consistent with the aggregation noted in brightfield TEM and suggests that crosslinking may happen in H-PDMS-GeNPs. HRTEM imaging (Figure 2.13(a-d), inset) shows crystalline domains with the lattice spacing of 0.33 nm, consistent with the present XRD analysis that correspond to Ge (111) lattice spacing.[51]

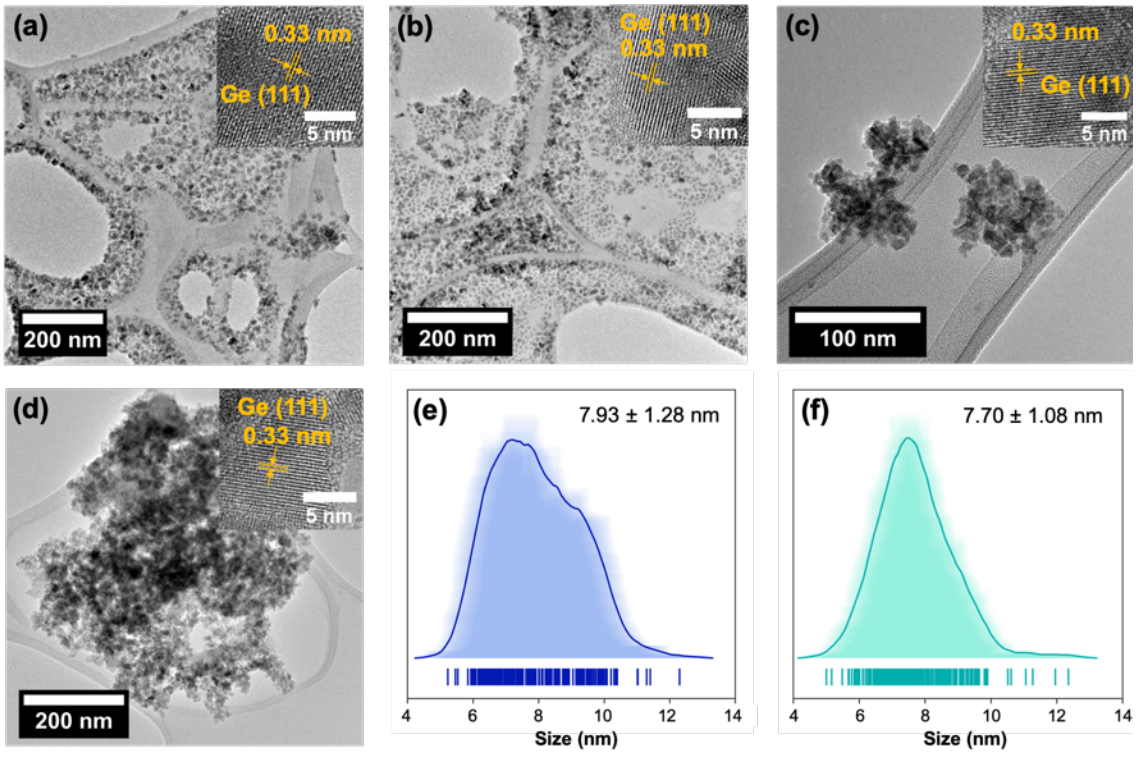

Figure 2.13. Brightfield TEM images of (a) octadecyl-GeNPs, (b) octadecylsilyl-GeNPs, (c) dimethyloctadecylsilyl-GeNPs, and (d) H-PDMS-GeNPs (inset: HRTEM), and the particle sizes histogram of (e) octadecyl-GeNPs and (f) octadecylsilyl-GeNPs obtained by ASH.

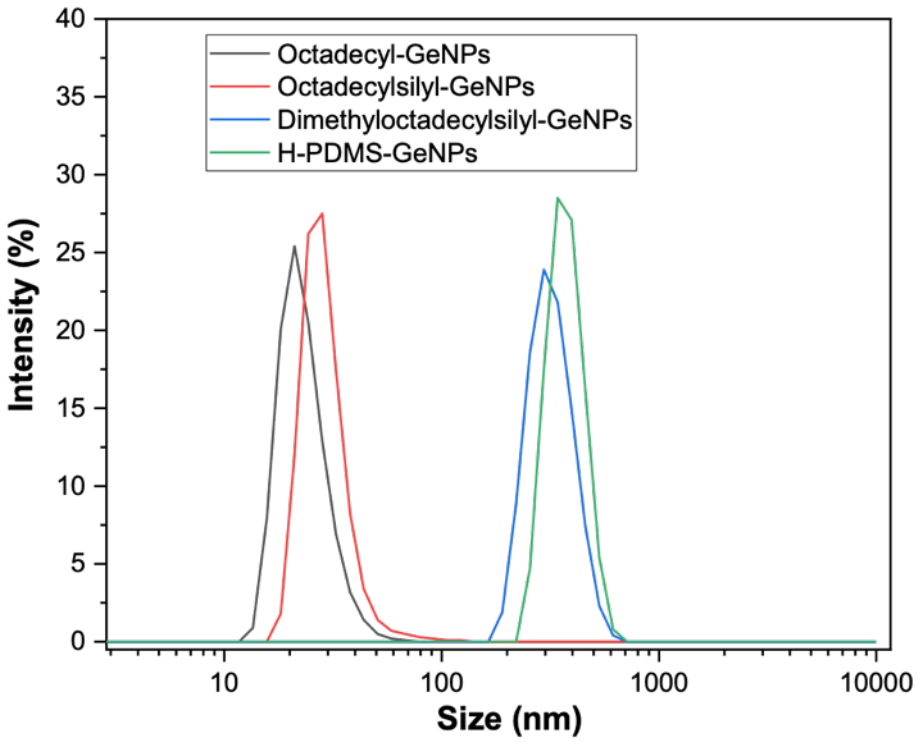

Figure 2.14. DLS size distribution of octadecyl-GeNPs, octadecylsilyl-GeNPs, dimethyloctadecyl-GeNPs, and H-PDMS-GeNPs.

EDX mapping can provide insight into the presence of the alkylsilane moieties on the GeNPs. Figures 2.15.1 to 2.15.4 show the EDX elemental mapping of octadecyl-GeNPs, octadecylsilyl-GeNPs, dimethyloctadecylsilyl-GeNPs, and H-PDMS-GeNPs, respectively. Each figure consists of a high angular annular dark field (HAADF) image, elemental maps of Ge, C, O, Si, and an overlay of elements. Octadecyl-GeNPs show Si distributed across the grid that is believed to arise from trace silicon impurities from the TEM grid. EDX mapping of an empty TEM grid is given in Appendix A. Despite this Si background, all GeNP samples showed Si signals co-localized with GeNPs, which supports the functionalization. The elemental spectra of all GeNPs are shown in Figure 2.16.

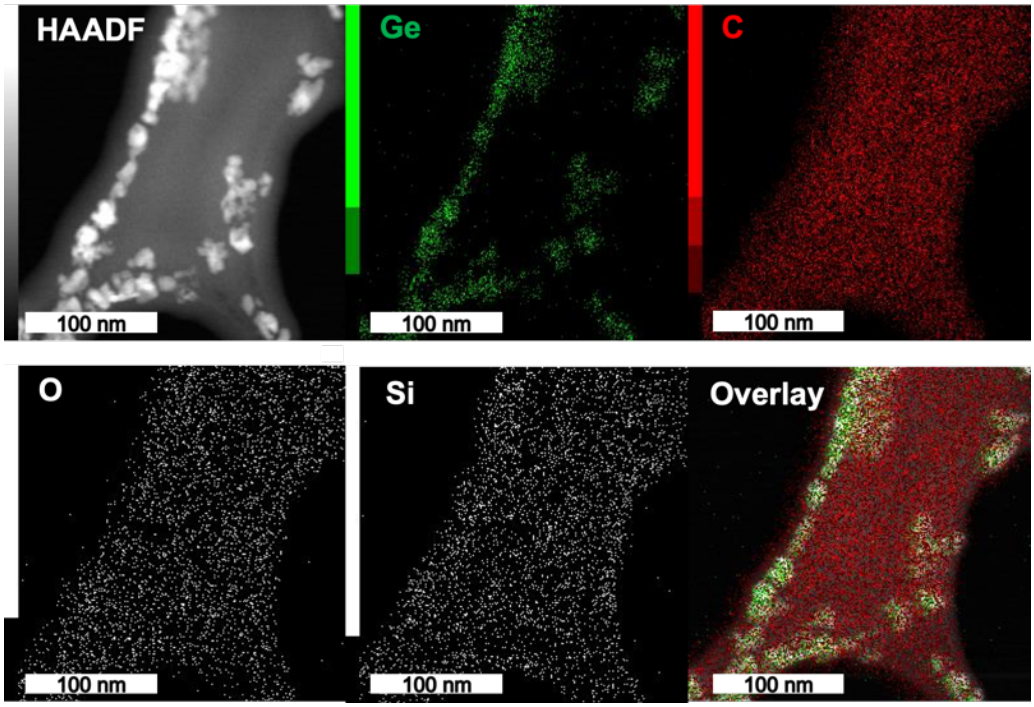

Figure 2.15.1. EDX elemental mapping of octadecyl-GeNPs.

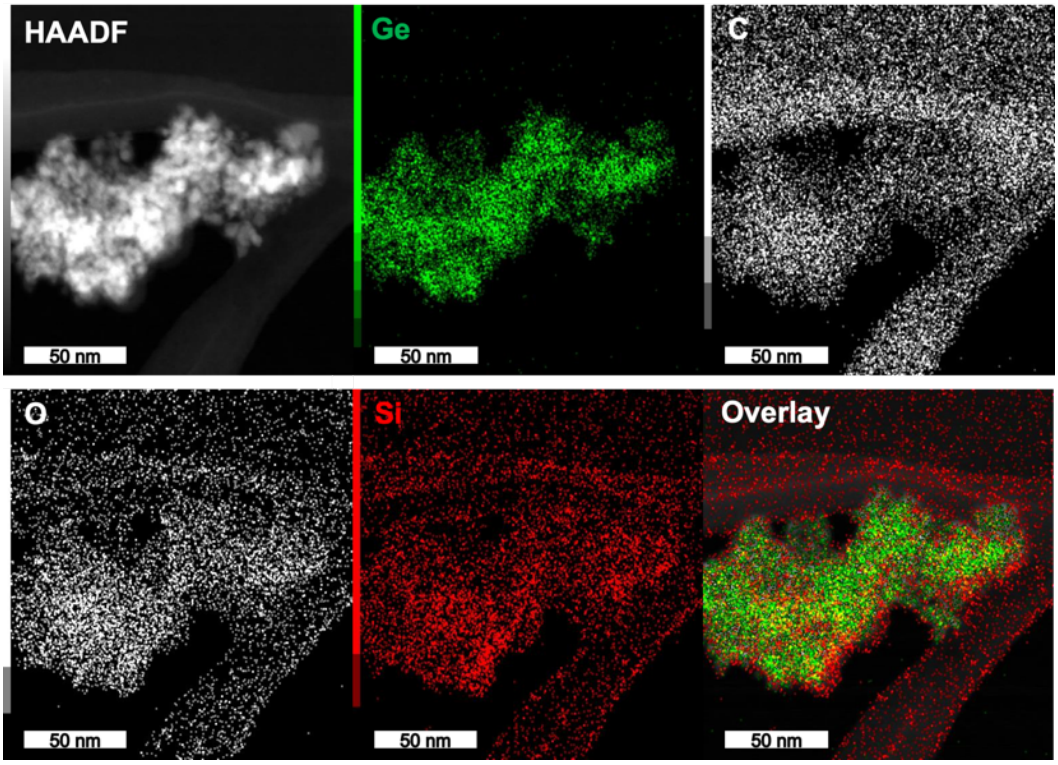

Figure 2.15.2. EDX elemental mapping of octadecylsilyl-GeNPs.

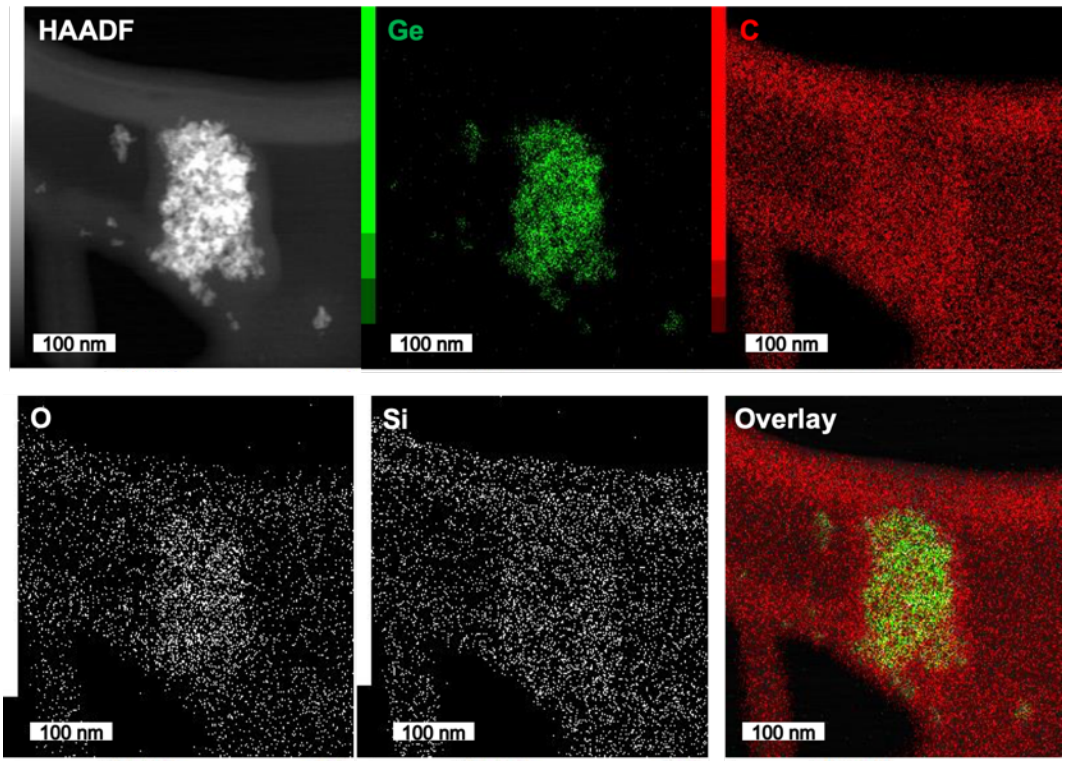

Figure 2.15.3. EDX elemental mapping of dimethyloctadecylsilyl-GeNPs.

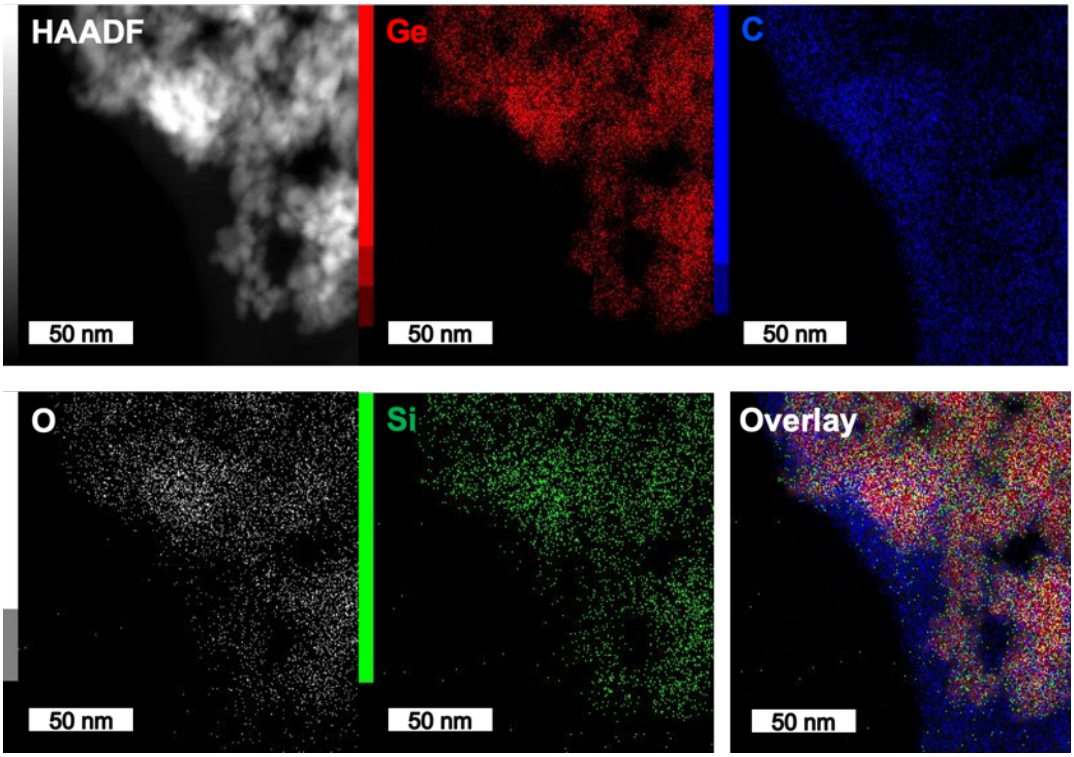

Figure 2.15.4. EDX elemental mapping of H-PDMS-GeNPs.

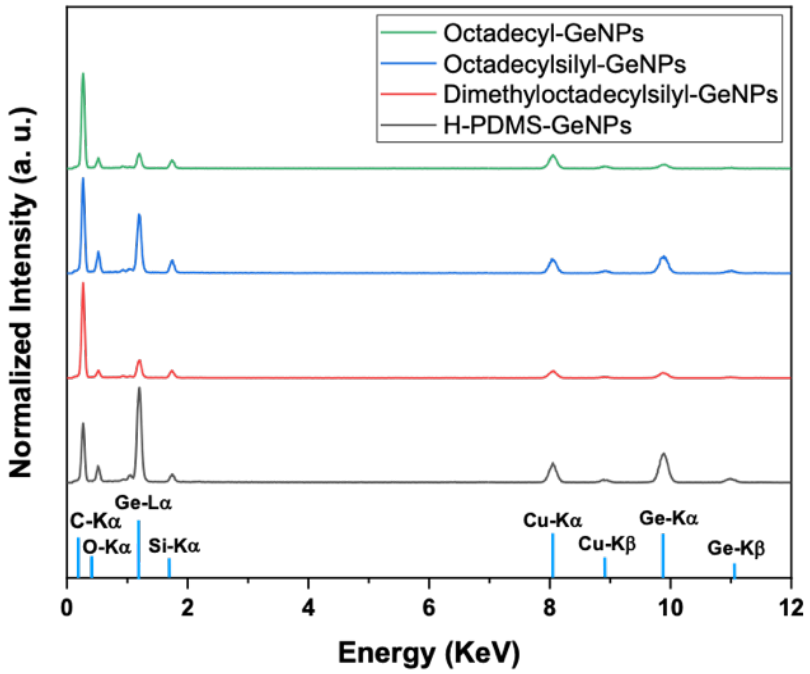

Figure 2.16. TEM-EDX spectra of octadecyl-GeNPs, octadecylsilyl-GeNPs, dimethyloctadecyl-GeNPs, and H-PDMS-GeNPs.

To gain more insight into the presence and location of Si at the surface of GeNPs, HAADF imaging and Electron Energy Loss Spectroscopy (EELS) line scans were acquired for octadecylsilyl-GeNPs. HAADF imaging shows a contrast between core and surface materials, consistent with different materials at the particle surface and within the particle core (Figure 2.17a). The EELS line scans of two representative single particles indicate that the intensities of silicon signals are substantially higher at the particle edges, while the composition of the core is dominated by germanium (Figure 2.17b).

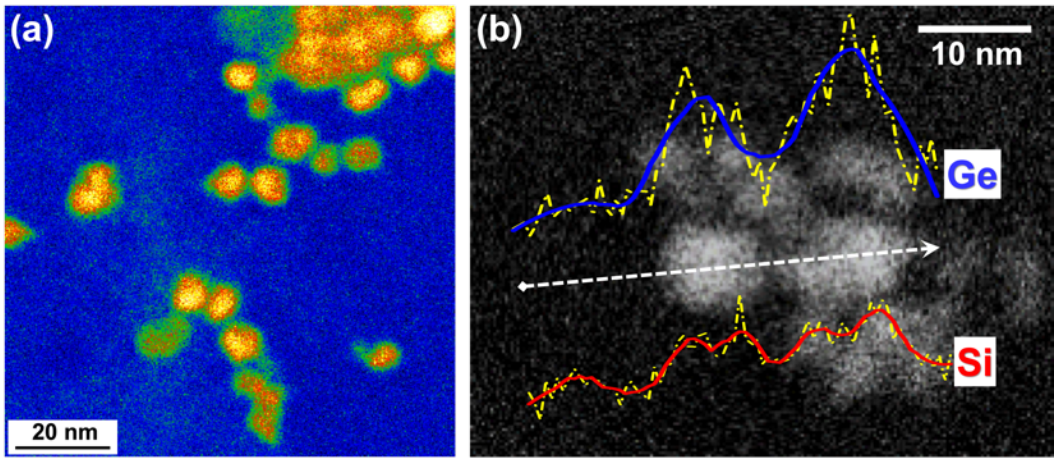

Figure 2.17. (a) HAADF image of octadecylsilyl-GeNPs, and (b) EELS line scanning of two single particles showing the composition of the core and shell.

To obtain the surface coverage of the alkylsilane/alkene functionalized-GeNPs, ^{1}H-NMR spectroscopy was employed. Using a predefined amount of tetramethylsilane (TMS, 0.03% v/v) as an internal standard and evaluating a ratio of the integrated peak areas of the surface groups provides an estimate of the percent surface coverage. In this context, the average surface coverage of octadecyl-GeNPs, octadecylsilyl-GeNPs, and dimethyloctadecylsilyl-GeNPs obtained from hydrogermylation/dehydrocoupling reaction are defined to be 170%, 139%, and 80.6%, respectively (Table 2.4, 2.5, and 2.6).

Table 2.4. Determination of Surface Coverage of Octadecyl-GeNPs Using ^{1}H NMR

NMR peak	Ligand to TMS Proton ratio	Moles of ligand[#]	% Surface coverage[$]
a (-CH_3)	6.23	3.29×10^{-5}	157
b (-$(CH_2)_{16}$-)	61.12	2.85×10^{-5}	182

[#] 0.03% v/v of TMS in 0.6 mL of $CDCl_3$ solvent has been defined as 1.32×10^{-6} moles.
[$] Per 7.3 mg of functionalized GeNPs contain 1.81×10^{-5} moles considering *ca.* 18% of atoms on the surface.

Table 2.5. Determination of Surface Coverage of Octadecylsilyl-GeNPs Using ^{1}H NMR

NMR peak	Ligand to TMS Proton ratio	Moles of ligand[#]	% Surface coverage[$]
a (-CH_3)	1.53	8.08×10^{-6}	163
b (-$(CH_2)_{16}$-)	12.91	6.39×10^{-6}	129
c Si-(CH_2)-	0.78	6.18×10^{-6}	125

[#] 0.03% v/v of TMS in 0.6 mL of $CDCl_3$ solvent has been defined as 1.32×10^{-6} moles.
[$] Per 2.0 mg of functionalized GeNPs contain 4.96×10^{-6} moles considering *ca.* 18% of atoms on the surface.

Table 2.6. Determination of Surface Coverage of Dimethyloctadecylsilyl-GeNPs Using ^{1}H NMR

NMR peak	Ligand to TMS Proton ratio	Moles of ligand[#]	% Surface coverage[$]
a (-CH_3)	2.27	1.20×10^{-5}	89.6
b (-$(CH_2)_{16}$-)	22.55	1.12×10^{-5}	83.3
c Si-(CH_2)-	1.36	1.08×10^{-5}	80.6
d -Si-$(CH_3)_2$-)	3.50	9.24×10^{-6}	68.9

[#] 0.03% v/v of TMS in 0.6 mL of $CDCl_3$ solvent has been defined as 1.32×10^{-6} moles.
[$] Per 5.4 mg of functionalized GeNPs contain 1.34×10^{-5} moles considering *ca.* 18% of atoms on the surface.

To understand the amorphous shoulder signal that was observed in the Raman spectra of all the synthesized GeNPs (Figure 2.5), we filtered the reaction mixture of octdecylsilyl-GeNPs after the reaction, collected the filtered (by 0.45-μ PTFE) and non-filtered (particles that did not pass through filter) particles, and performed a separate purification and characterization. The FTIR of filtered and non-filtered samples in Figure 2.18 suggests successful functionalization where both the spectra exhibit characteristic peaks of octadecylsilyl-GeNPs similar to Figure 2.4. The ^{1}H-NMR (Figure 2.19) of these samples show a characteristic chemical shift that was observed earlier in Figure 2.6, consistent with functionalization.

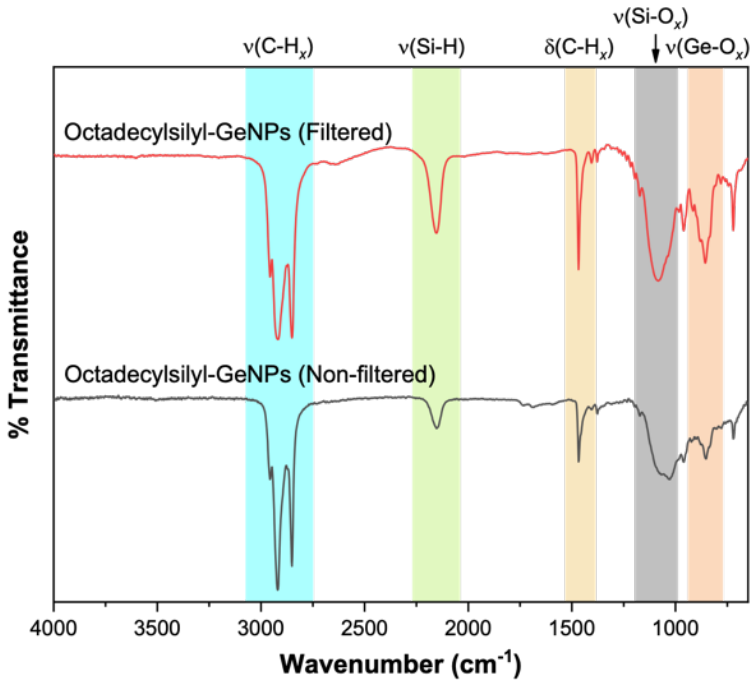

Figure 2.18. FTIR of filtered and non-filtered octadecylsilyl-GeNPs samples.

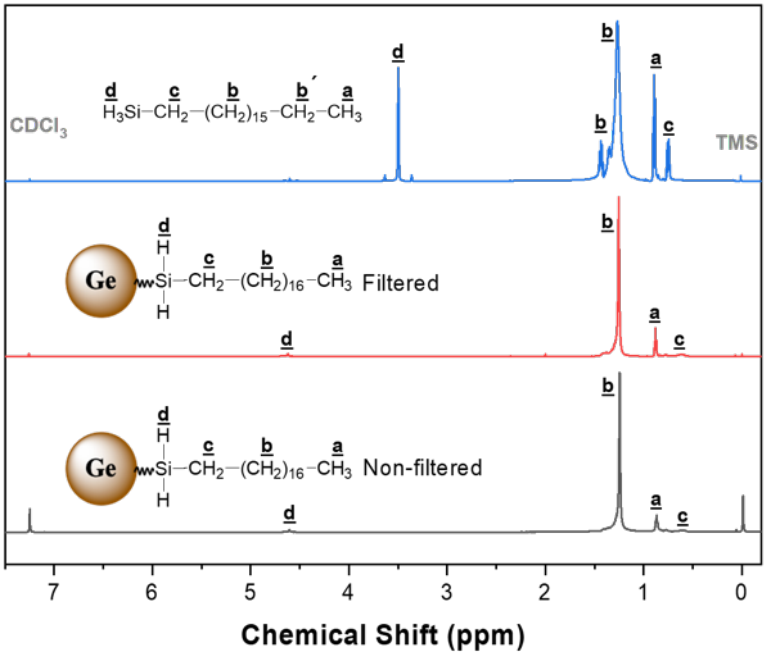

Figure 2.19. ^{1}H-NMR of octadecylsilane, filtered, and non-filtered octadecylsilyl-GeNPs samples in $CDCl_3$ (7.2 ppm) solvent with 0.03% TMS (0.0 ppm).

The XRD of filtered samples does not show crystalline GeNPs, but non-filtered samples show the presence of crystalline GeNPs (Figure 2.20). In both samples, we observe the reflection associated with the octadecylsilane. In TEM, filtered samples were observed to be fairly dispersed, but the non-filtered samples were aggregated (Figure 2.21).

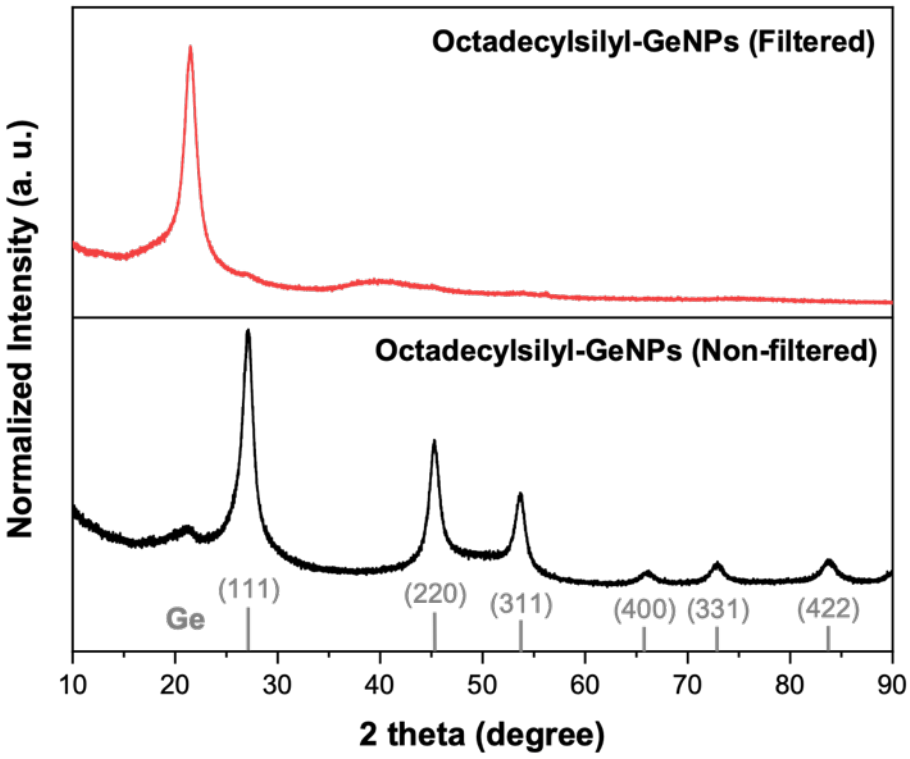

Figure 2.20. X-ray Diffraction of filtered and non-filtered octadecylsilyl-GeNPs samples. Standard reflections of Ge (PDF# 04-0545) are provided for comparison.

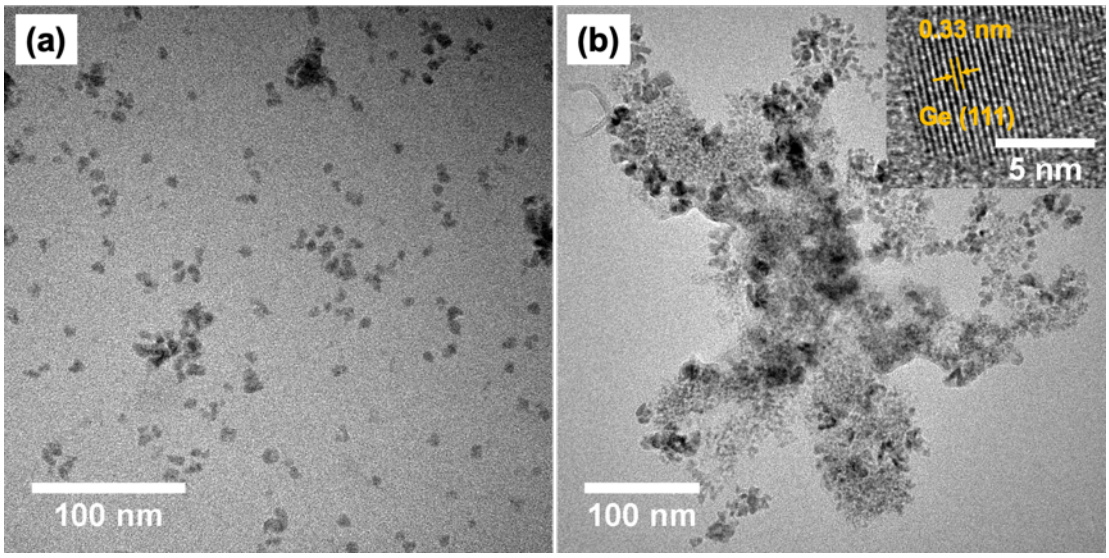

Figure 2.21. Bright field TEM images of filtered and non-filtered octadecylsilyl-GeNPs samples.

A control reaction has been performed with dodecane and octadecylsilane. The FTIR and ^{1}H-NMR results of the control reaction are shown in Appendix A.

2.4 Conclusion

We have synthesized alkylsilane functionalized GeNPs through DHC successfully. DHC of alkylsilane on GeNPs proceeds via Si–Ge bond formation, and by attaching appropriate groups we can modify the surface further. FTIR and ^{1}H-NMR show the presence of alkylsilane in the samples. XPS and TEM-EDX show the presence of silicon, along with germanium. Raman data demonstrate the presence of amorphous and crystalline GeNPs mixtures. Later on, we found that the particles that pass through the filter are amorphous. Finally, EELS line scanning confirms the presence of silicon, mostly on the surface of GeNPs. DHC has given us an efficient and catalyst free way to functionalize GeNPs. It has demonstrated comparable reactivity with hydrogermylation, which in turn may give us a pathway to make new functional nanomaterials.

Chapter 3

Germanium Nanoparticles-Polymer Hybrid Solar Cells

3.1 Introduction

3.1.1 Scope of the Research

Due to the limited sources of fossil fuels and the growing demand for world-wide energy (13 TW in 2001 vs 30 TW in 2050),[215,216] research on cost-effective alternative energy sources has increased significantly in the past few years. While the conventional silicon solar cells are expensive, they also are unable to provide enough energy density for human needs.[217–219] Semiconductor polymers are excellent candidates in photovoltaics because of their solution processability, tunable properties, and feasibility in industrial production.[220] Among different architectures of organic photovoltaics (OPVs), the bulk heterojunction (BHJ) structure, in which a conjugated polymer is mixed with a fullerene derivative, is studied most widely. In this structure, the conjugated polymer acts as an electron donor, and the fullerene derivative acts as an electron acceptor.

Poly(3-hexylthiophene) (P3HT) is one of the most studied donor polymers because of its good self-assembly and charge transport capabilities. Moreover, with the combination of a fullerene acceptor ($PC_{61}BM$), researchers could achieve up to 5% power conversion efficiency (PCE).[217] Zhang et al., reported more than 10% PCE using a benzodithiophene (BDT) based donor polymer.[221] PTB7-Th is one of the BDT based polymers that has a narrow band gap (1.6 eV) and a deep highest occupied molecular orbital (HOMO) level, which is well matched with various electron acceptor materials.[222] Non-fullerene acceptors are getting much attention due to their simple synthesis and low cost compared to fullerene derivatives. One of the early discovered non-fullerene acceptor materials, ITIC blended with PTB7-Th, has shown greater PCE compared to fullerene (6.8% vs 6.05%).[223] Zhao et al. prepared IT-4F by fluorinating the ITIC and obtained 13% PCE by blending with PBDB-T-SF donor.[157] The advantages of fluorinated semiconductors are that they downshift the HOMO and LUMO levels of the molecules without a causing strong steric

hindrance[224] and improve their crystallinity by non-covalent interactions of F···H and F···S, which in turn facilitate charge transport.[225] It is essential to correlate the crystallinity, the polymer grain size, etc. with the charge transport and the performance of solar cells. Grazing Incidence X-ray scattering (GIXS) is a very important technique to obtain the crystallinity and grain sizes of active layers of a polymer solar cell; [226] this is discussed later in this chapter.

Hybrid solar cells have attracted considerable attention among researchers because of the desirable properties of conjugated polymers and inorganic nanoparticles. In hybrid solar cells, semiconductor polymers act as an electron donor and nanoparticles act as an electron acceptor. Semiconductor nanoparticles have properties which differ from bulk materials due to quantum confinement and the possibility to tune their absorption properties by tuning their size. Various colloidal inorganic nanoparticles have been used in hybrid solar cells, including CdSe,[227] ZnO,[228] TiO_2,[229] PdS,[230] PdSe,[181] and Si[185] nanocrystals. However, the PCE was not very impressive, and the highest PCE observed in hybrid solar cells is 4.1% for the combination of P3HT and CdSe nanoparticles in the active layer.

An interesting strategy for boosting the efficiency of polymer solar cells is to add a third component in the active layer. Huang et al.[231] introduced Bi_2O_2S nanocrystals into the PTB7-$PC_{71}BM$, which significantly improved the PCE by promoting charge transfer, increasing exciton diffusion, and reducing charge recombination. Germanium nanoparticles (GeNPs) are very promising materials for optoelectronic applications because of their large exciton Bohr radius (*ca.* 24 nm), narrow band gap (*ca.* 0.67 eV in bulk), high carrier mobility, and high absorption coefficient (*ca.* 2.0×10^5 cm^{-1} at 2 eV).[41,232] Amollo et al.[233] have introduced GeNPs/graphene nanocomposites into the active layer of P3HT-$PC_{60}BM$ solar cells and obtained a higher PCE due to the better charge separation and transfer by the nanocomposites. The challenge associated with GeNPs is that in a normal atmosphere they often are covered by an insulating oxide shell, which limits their application. Therefore, the surface of the GeNPs should be passivated with appropriate surface groups to prevent oxidation and maintain favorable optoelectronic properties.

In this research, dodecyl-terminated Ge nanoparticles (dodecyl-GeNPs) were synthesized and mixed with a semiconducting polymer donor and a small molecule acceptor (PTB7-Th and IT-4F) and deposited as thin films on glass and silicon wafer substrates. The structures of PTB7-Th (Poly([2,6′-4,8-di(5-ethylhexylthienyl)benzo[1,2-b;3,3-b]dithiophene]{3-fluoro-2[(2ethylhexyl) carbonyl] thieno [3,4-b]thiophenediyl})) and IT-4F (3,9-bis(2-methylene-((3-(1,1-dicyanomethylene)-6,7-difluoro)-indanone))-5,5,11,11-tetrakis(4-hexylphenyl)-dithieno-[2,3-d:2',3'-d']-s-indaceno[1,2-b:5,6-b']dithiophene) are shown in Figure 3.1. The samples were characterized by atomic force microscopy (AFM), GIXS, UV-vis, and 4-point probe to obtain structural, optical, and electronic properties. Their solar cell performances were evaluated by a solar simulator.

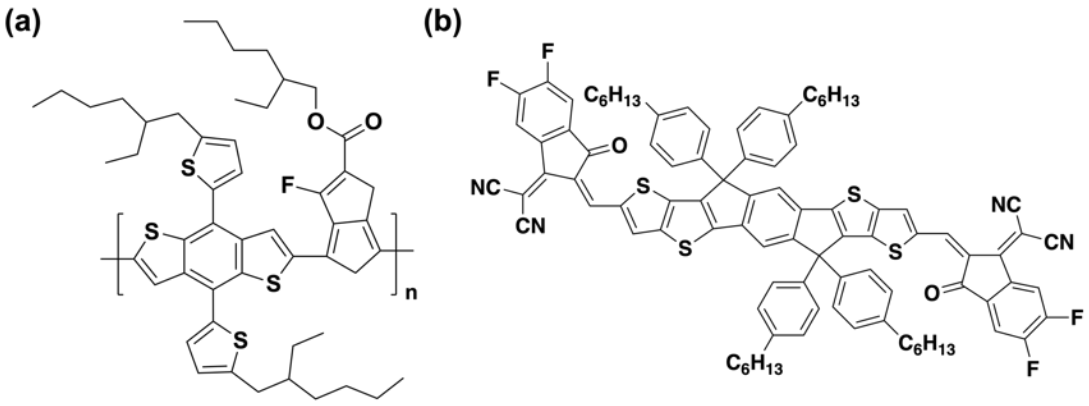

Figure 3.1. Structure of (a) PTB7-Th and (b) IT-4F.

3.1.2 Grazing Incidence X-ray Scattering for Photovoltaics

Grazing Incidence X-ray Scattering (GIXS) is a technique to obtain morphological information of active materials and thin films used in organic photovoltaics.[234] There are two types of GIXS depending on the sample to detector distance (SDD), Grazing Incidence Small Angle X-ray Scattering (GISAXS) and Grazing Incidence Wide Angle X-ray Scattering (GIWAXS).

The GISAXS technique probes the surface and bulk morphologies of thin films in a length scale from nanometer to micrometer size. A basic experimental setup of the GISAXS is shown in Figure 3.2.[235] The monochromatic X-ray beam impinges on the sample surface under a very shallow angle, α_i, typically with $\alpha_i < 1^\circ$. The X-rays are

scattered by the samples under investigation and meet a 2D detector in reciprocal space. The scattering of X-rays originates from variations of the refractive index, n, on the materials, described by[236]

$$n = 1 - \delta(\lambda) + i\beta(\lambda) \tag{3.1}$$

depending on the dispersion, δ, and the absorption, β. The δ and β can be written as

$$\delta(\lambda) = \frac{e^2\lambda^2}{8\pi^2 m_e c^2 \varepsilon_0}\rho\frac{\sum_k f_k^0(\lambda) + f'(\lambda)}{\sum_k M_k}$$

$$\beta(\lambda) = \frac{e^2\lambda^2}{8\pi^2 m_e c^2 \varepsilon_0}\rho\frac{\sum_k f''(\lambda)}{\sum_k M_k}$$

where, e is the elementary charge, λ is the wavelength of X-rays, m_e is the electron rest mass, c is the speed of light, ε_0 is the permittivity constant, ρ is the mass density, M_k is the atomic weight, and f' and f'' are the dispersion corrections. The value of f_k^0 can be approximated by the number of electrons, Z_k. The summation is done for all atoms k of a small molecule or of a monomer subunit in the polymer under investigation.[226]

In the experimental set up of the GISAXS (Figure 3.2), the x-axis is along the direction of X-ray beam, the y-axis is parallel to the sample surface, and the z-axis is along the surface normal. The diffuse scattering of X-rays occurs due to the lateral deviations of the refractive index of the materials; thus, desired information about the morphology of probed films can be obtained.

Monochromatic X-rays with a wave vector $\vec{k}_i$ and a wave number $k_0 = 2\pi/\lambda$ are scattered along the $\vec{k}_f$ direction, therefore, the scattering vector is defined as

$$\vec{q} = (q_x, q_y, q_z) = \vec{k}_f - \vec{k}_i \tag{3.2}$$

where, $q_x = 2\pi(cos\psi cos\alpha_f - cos\alpha_i)/\lambda$, $q_y = 2\pi(cos\psi cos\alpha_f)/\lambda$ and $q_z = 2\pi(sin\alpha_i + sin\alpha_f)/\lambda$.[226]

Each material has a characteristic critical angle, α_c, below which the X-rays are reflected via total internal reflection. When the exit angle of X-ray matches the critical angle, the scattering intensity of X-rays, called the Yoneda peak, is enhanced greatly.[237] For the GISAXS experiment, $\alpha_i > \alpha_c$ generally is used to obtain in-depth morphological information of the film. A 2D detector is used for the GISAXS, and the sample to detector distance (SDD) is 2–3 m. The GISAXS technique only records intensities of the diffuse scattering waves. To obtain structural information of the material, the intensity signals need

to be modeled. In this thesis, horizontal line cuts at the Yoneda position are modeled to obtain information about lateral structures using the local monodisperse approximation (LMA) method.[234,238] The DPDAK software package has been used to model the two-dimensional (2D) GISAXS intensity distribution within the framework of the LMA method.[239] In this method, it is possible to obtain the domain sizes of active polymer materials and the corresponding center-to-center distances of the domains. In organic photovoltaics (OPVs), the domain sizes and distances are important to correlate the exciton (electron-hole pair) diffusion lengths of semiconductor polymers and their photovoltaic performances.[240]

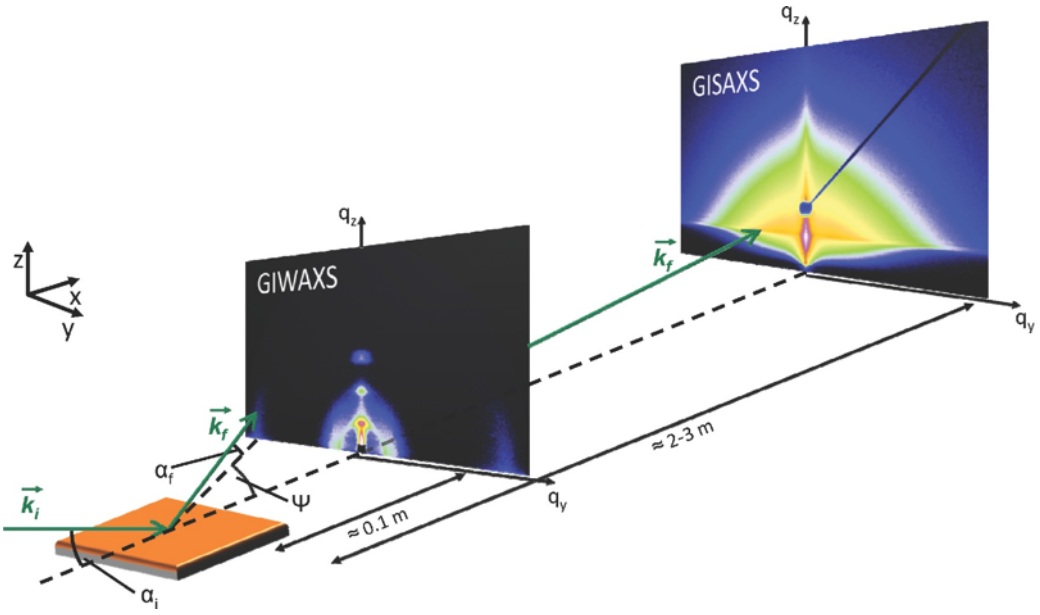

Figure 3.2. Schematic presentation of the experimental set-up used in GISAXS and GIWAXS.[235] Reprinted with permission from reference 235. Copyright 2014 Wiley-VCH Verlag GmbH & Co. KGaA.

The experimental setup for GIWAXS is similar to GISAXS, except that the SDD of the 2D detector is much shorter to cover the wide-angle data. It is possible to obtain information about molecular stacking, crystal orientation, and crystal size of the materials using the shorter SDD, usually in the order of 10 cm. The GISAXS scattering also shows up here, however, it is faintly visible and usually blocked by a beam stop. For the GIWAXS, when *hkl*-lattice planes fulfill Bragg's law at a certain angle, constructive interference occurs, and that gives rise to a maximum scattering. The SSD is chosen in

such way that polymeric crystals (e.g., π-π stacking, orientation) are probed and also at least the first reflection of inorganic crystals is detectable. Compared to XRD, GIWAXS is able to detect the preferred orientation of the crystals in thin films. For example, in terms of the semiconducting polymer P3HT, the orientation distribution of its crystallites that either face-on or edge-on can be quantified using GIWAXS.[241] For OPVs, a certain crystal orientation relative to the sample surface is more beneficial for charge transport than the other orientations.[242] In order to understand the correlation between the crystal orientation and scattering signals better, four scenarios of GIWAXS patterns are illustrated schematically in Figure 3.3.

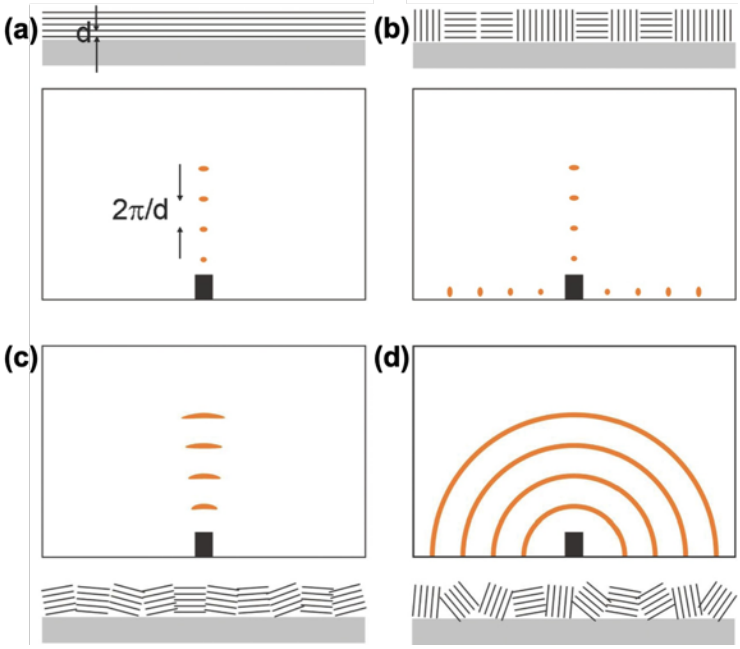

Figure 3.3. Sketch of film crystallinity and corresponding 2D GIWAXS data in the case of (a) horizontal lamellar stacking, (b) vertical and horizontal stacking, (c) textured horizontally oriented domains, and (d) completely disordered lamellar stacking. The GISAXS signal is blocked by a beam stop (black box).[235] Reprinted with permission from reference 235. Copyright 2014 Wiley-VCH Verlag GmbH & Co. KGaA.

For highly crystalline polymers/materials with a direction of all crystal planes parallel to the substrate, well pronounced Bragg reflections appear on the 2D detector along the surface normal, with a distance of $2\pi/d$ (Figure 3.3a). If both parallel and perpendicular crystal planes are present, the Bragg reflections appear along the surface normal as well as in the horizontal direction (Figure 3.3b). For textured films having

domains oriented with an angular distribution parallel to the substrate, the Bragg reflections become broadened along the vertical direction (Figure 3.3c). In the case of powder like films having no preferential orientation, the Debye-Scherrer ring appears in the GIWAXS pattern instead of Bragg reflections (Figure 3.3d).

In the GIWAXS measurements, a spherical surface in q-space is projected onto a 2D detector, thus the obtained GIWAXS pattern is distorted. In order to extract structural information, the raw 2D GIWAXS pattern must be reconstructed into the natural reciprocal space coordinates.[243] Here, the x-axis in the GIWAXS pattern is q_r *or* q_{xy}, where q_r is determined by $q_r = \sqrt{{q_x}^2 + {q_y}^2}$. In this thesis, the grazing incidence X-ray scattering graphical user interface (GIXSGUI) analysis package in MATLAB is used to retrieve the corrected reciprocal space patterns.[243] An example of the raw 2D GIWAXS data and the data after reconstruction is shown in Figure 3.4. A wedge of missing data is observed in the reconstructed image due to the inaccessible q-range from the experiment.

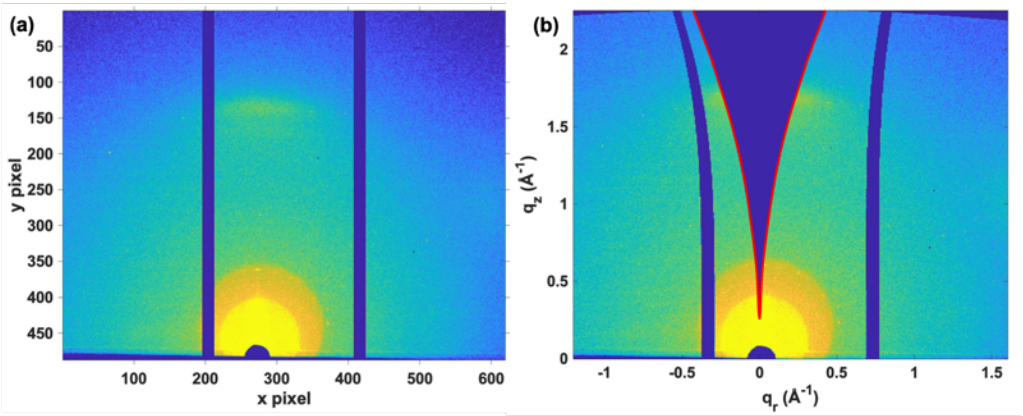

Figure 3.4. (a) An example of raw 2D GIWAXS data recorded and (b) the corresponding corrected 2D GIWAXS data retrieved using GIXSGUI. The inaccessible q-range in a wedge shape is denoted by the red curves. Two curved blue stripes at q_y = -0.3 Å^{-1} and 0.7 Å^{-1} are due to the intermodular detector gaps.

3.2 Experimental

3.2.1 Reagents and Materials

Germanium dioxide powder (GeO_2, 99.9%) was purchased from Gelest. Hypophosphorous acid (50 wt% in water), sodium hydroxide pellets, methanol (99.8%), anhydrous ethanol,

acetone, isopropyl alcohol (98%), toluene (99.9%, HPLC grade), 1-dodecene (95%), zinc acetate dihydrate (≥98%), ethanolamine (≥98%), 2-methoxyethanol, chlorobenzene (99.8%), and 1-8 diiodooctane (97%) were purchased from Sigma-Aldrich. Toluene was purified using a Pure-Solv purification system and collected immediately prior to use. Hydrochloric acid (36.5–38.0%) and ammonium hydroxide (28–30%) were purchased from Caledon Labs. Electronics grade hydrofluoric acid (HF, 49 % aqueous solution) was purchased from J. T. Baker. Ultrapure H_2O (18.2 MΩ/cm) was obtained from a Barnstead Nanopure Diamond purification system and was used in all reactions. Molecular sieves (4 Å) were purchased from Sigma-Aldrich and activated in a vacuum oven prior to use. PTB7-Th (M_n = 52500 $gmol^{-1}$, PDI = 2.0) was purchased from 1-Material Inc. IT-4F was purchased from Solarmer Materials Inc. Unless otherwise indicated, reagents were used as received. Silicon (100 mm diameter, (100) orientation) substrates were purchased from Si-Mat. Microscopic soda-lime glasses (26 × 76 mm^2) were purchased from Carl Roth GmbH. Indium tin oxide (ITO) coated glass substrates (22 × 22 mm^2) were purchased from Solems (ITO thickness 100 nm, sheet resistance 30 Ω/sq).

3.2.2 Preparation of GeNPs embedded in Germanium Oxide

See Section 2.2.2

3.2.3 Isolation of Hydride-terminated GeNPs

See Section 2.2.2

3.2.4 Hydrogermylation of H-GeNPs Surfaces

An established literature procedure was employed to modify GeNP surfaces via thermally-induced hydrogermylation.[51] Briefly, H-GeNPs were liberated from the GeNP/GeO_x and mixed with neat 1-dodecene (10 mL). The cloudy mixture was subjected to three freeze-pump-thaw cycles and heated in an oil bath at 190 ˚C for 15 h, with stirring, to yield a deep brown solution. The resulting dodecyl-terminated GeNPs (dodecyl-GeNPs) were transferred to polytetrafluoroethylene (PTFE) centrifuge tubes, and 30 mL of anhydrous ethanol were added as an antisolvent. The resulting brown suspension was centrifuged at 12000 rpm for 20 min to yield a brown precipitate and a colorless supernatant. The

supernatant was discarded, and the precipitate was re-dispersed in 5 mL of toluene, with sonication, to yield a transparent brown solution. Then, 15 mL of anhydrous ethanol and 15 mL of methanol were added, and the mixture was centrifuged at 1200 rpm for 20 min to yield brown precipitate. This solvent/antisolvent suspension/precipitation was repeated once. Finally, the precipitate (dodecyl-GeNPs) was dispersed in 5 mL of dry toluene and stored in a vial for further use and characterization.

3.2.5 Cleaning of Glass and Silicon Substrates

Prior to the preparation of GeNPs/polymer blend films, soda-lime glass microscope slides and Si wafer substrates were cut into smaller pieces (roughly 10 × 10 mm^2) with a diamond cutter and acid cleaned to remove surface impurities.[244] Briefly, an acid bath was prepared by using 84 mL of H_2O_2, 198 mL of H_2SO_4 (98%), and 54 mL of DI water and heated at 80 ºC. The Si and glass substrates were loaded on a Teflon holder and immersed in this acid bath. After 15 min, the substrates were collected from the acid bath, rinsed with DI water, and dried in flowing N_2. After drying, the substrates were stored in a clean sample box for further use.

3.2.6 Preparation of Ge-PTB7-Th Thin Films

A PTB7-Th solution was prepared by mixing 60 mg of PTB7-Th with 6 mL of chlorobenzene in a glass vial in an argon filled glove box and stirred at 70 ˚C for 15 h to obtain blue suspension. The suspension was divided into six glass vials, each containing 1 mL of 10 mg/mL PTB7-Th. Then, 0, 0.1, 0.3, 0.5, 0.7, and 0.9 wt% of dodecyl-GeNPs (1.0 mg/mL in dry toluene) were added to those vials. Additional dry toluene was added to keep the concentration of PTB7-Th constant, and the mixtures were stirred for 3 h. The samples were spin coated at 1000 rpm for 2 min on an acid cleaned glass and Si substrate. The thin film samples were dried at room temperature (RT) and were kept in a glovebox for further use and characterization.

3.2.7 Preparation of Ge-PTB7-Th-IT4F Thin Films

A sample of 1,8-diiodooctane (DIO) (10 µL) was mixed and stirred in 1.99 mL of chlorobenzene to obtain 0.5% DIO in chlorobenzene. Then, 20 mg/mL of a donor-acceptor

polymer was prepared by addition of 20 mg of PTB7-Th and 20 mg of IT-4F in 2 mL of prepared chlorobenzene solution. The mixture was stirred at 70 ˚C for 15 h and split into six vials containing 300 μL each. Next, 0, 0.1, 0.3, 0.5, 0.7, and 0.9 wt% of dodecyl-GeNPs (1.0 mg/mL in dry toluene) were added to those vials. Additional dry toluene was added to keep the concentration constant. The mixtures were stirred for 3 h and spin coated at 2000 rpm for 2 min on an acid cleaned glass and Si substrate. The thin film samples were dried at RT and were kept in a glovebox for further use and characterization.

3.2.8 Fabrication of Solar Cell Devices

3.2.8.1 Etching and cleaning of ITO

To avoid short circuits in the solar cells, the ITO layer of an ITO coated glass substrate was etched partially. A schematic diagram of the etching and cleaning of ITO is shown in Scheme 3.1. Briefly, a 12-mm width of sticky tape was attached to the middle of the ITO substrate as a template. Next, Zn powder was spread on the ITO exposed edges and 5-mm wide stripes of ITO were wiped off from two opposite edges of the substrate by using HCl-soaked cotton buds (Q-tips). The substrates were rinsed with water and the sticky tape was removed.[245]

The ITO coated glass substrates were cleaned ultrasonically with an Alconox® solution (detergent), deionized water, acetone, and isopropyl alcohol in a sequence of 10 min each. The substrates were dried in a N_2 flow. Finally, the partially etched ITO coated glass substrates were cleaned by oxygen plasma using Plasma System Nano (Diener Electronics) at 0.4 mbar for 10 min. The thin films of ZnO were prepared immediately after plasma cleaning.

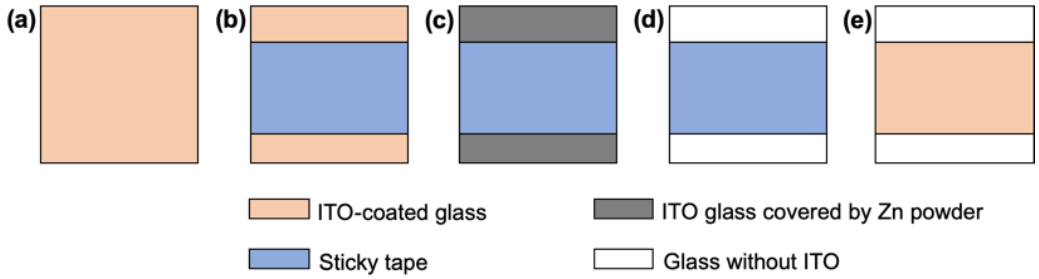

Scheme 3.1. Schematic procedure of etching and cleaning of ITO; (a) a plain ITO coated glass substrate, (b) a 12-mm^2 wide sticky tape is applied over the center of the substrate, (c) Zn powder is scattered on non-templated ITO, (d) Zn powder and ITO are wiped away with HCl-soaked cotton buds (Q-tips), and (e) the substrate is rinsed with water and the sticky tape removed.

3.2.8.2 Preparation of active layer thin films

A ZnO precursor solution was prepared by dissolving 1.0 g of zinc acetate dihydrate and 0.284 mL ethanolamine in 10 mL of 2-methoxyethanol.[246] The solution was stirred at 60 ºC for 2 h to yield a clear homogeneous solution and was aged for 1 day before spin coating. The ZnO precursor solution was spin coated onto the pre-cleaned ITO-coated glass substrates at 3000 rpm for 1 min and then annealed at 200 ˚C for 1 h in air to obtain a *ca.* 30-nm ZnO layer. After that, PTB7-Th/IT-4F, 0.3% GeNPs/PTB7-Th/IT-4F, and 0.9% GeNPs/PTB7-Th/IT4F solutions were spin-coated at 1200 rpm for 2 min to obtain a *ca.* 100-nm thickness active layer. Next, using a shadow mask, thin layers of MoO_3 (10 nm) and Al contact (100 nm) were deposited sequentially on top of the active layer using thermal evaporation at low air pressure (2×10^{-6} mbar). A schematic diagram of fabrication of solar cells is given in Figure 3.5a and a picture of the fabricated cells is given in Figure 3.5(b). The fabricated solar cells were used to obtain *J-V* characteristics and the power conversion efficiency (PCE).

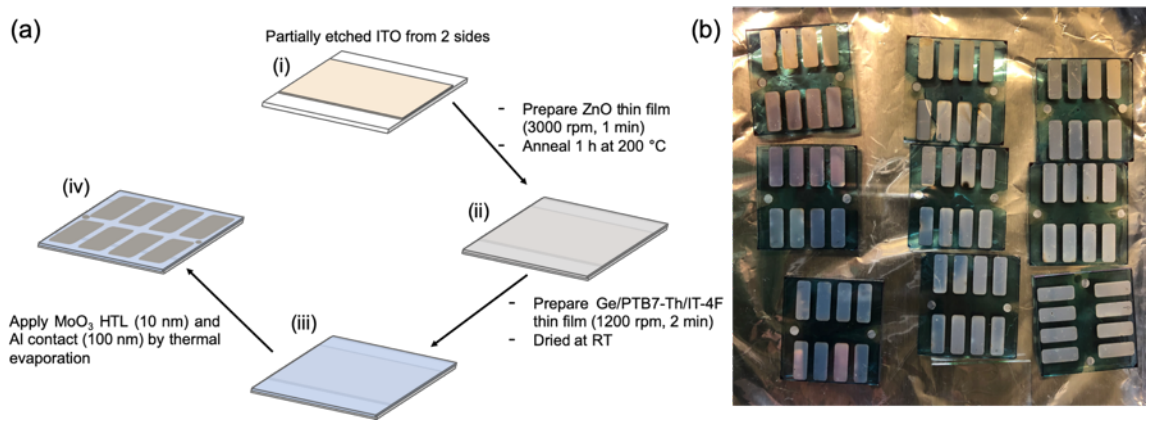

Figure 3.5. (a) Schematic diagram of fabrication of solar cells: (i) a partially etched and cleaned ITO, (ii) sample with ZnO layer, (iii) sample with active layer (Ge/polymer blend), and (iv) sample after applying MoO_3 (10 nm) and Al (100 nm) contact. (b) A photograph of fabricated Ge/PTB7-Th/IT-4F solar cells.

3.2.9 Materials Characterization and Instrumentation

X-ray diffraction (XRD) was performed using a Rigaku Ultima IV equipped with a Cu-Kα radiation source (λ = 1.54 Å) using the thin film stage. The functionalized dodecyl-GeNPs samples were drop casted onto a Si (100) wafer and dried under air. The diffraction patterns were obtained with an incident angle of 0.5º and a scan speed of 0.25º/min. The $Ge(OH)_2$ and GeNPs/GeO_x samples were prepared by putting *ca.* 50 mg of powder onto a Si (100) wafer and were analyzed similarly in the thin film stage. The patterns were analyzed with the TOPAS Academic software package.[202] A NIST 640f Si standard was used for calibration. Instrument parameters were determined with a bulk Ge wafer ground into powder as the bulk standard. Additionally, diffraction data of Si wafers were collected to determine the contribution from the holders.

Bright-field transmission electron microscopy (TEM) and high-resolution TEM (HRTEM) were performed in a JEOL JEM-ARM200CF equipped with a cold field emission gun (cFEG) having an accelerating voltage of 200kV. TEM samples were prepared by drop-coating 1–2 drops of a dilute toluene suspension containing GeNPs onto a carbon coated copper grid (150 mesh, Electron Microscopy Science), and the solvent was removed by using filter paper under the grid. The images were processed using ImageJ software (version 1.51j8), and at least 300 particles were measured to obtain the size distributions of GeNPs.

Fourier Transform Infrared spectroscopy (FTIR) was performed using a Nicolet Magna 750 IR spectrophotometer. The samples were prepared via drop casting from a toluene suspension onto a silicon wafer.

An Axiolab A microscope (Carl Zeiss) was used to obtain optical microscopy with 10X zoom of 0.82 μm/pixel resolution. ImageJ software (version 1.51j8) was used to analyze the image.

Atomic force microscopy (AFM) was used to probe the surface roughness of polymer hybrid thin films. An Autoprobe CP research (Veeco Metrology Group) AFM instrument with conical shaped cantilevers (Ultralever OLNC-B, radius 10 nm) was used with a resonance frequency of 70–80 KHz and spring constant of 2.1 N/m. The Gwyddion software (v2.20) was used to analyze and post-treat the obtained AFM data.

The thickness of the thin films was measured by a DektakXT™ profilometer. The thin films of the polymer layer were scratched, and the height profile of the non-scratched and scratched part of the film were obtained.

The sheet resistance of the polymer hybrid thin films was measured using a four-point probe (Cascade Microtech (C4S-54/5)) consisting of four equally spaced tungsten carbide test probes (1-mm distance and 135-μm radius). The conductivity was calculated from the sheet resistance and thickness of the films using the equation $\kappa = 1/R_s t$, where κ is conductivity, R_s is the sheet resistance, and t is the thickness of the film.

GISAXS and GIWAXS measurements were carried out at the P03/KiNaXS beamline of the PETRA III storage ring at DESY (Hamburg, Germany). The wavelength of the X-ray was 1.059 Å (Energy 11.7 KeV). A Pilatus 1M 2D detector was used to record scattering signals consisting of 981 × 1043 pixels for GISAXS and 619 × 487 pixels for GIWAXS. The pixel size for both cases were 172 μm × 172 μm. For GISAXS measurements, a grazing incident angle of 0.19º and an SDD of 3302.31 mm were chosen. For GIWAXS, 0.35º of grazing incidence angle and 270.044 mm of SDD were used. The GISAXS was analyzed by using DPDAK software. The GIWAXS data were analyzed by using MATLAB (version R2018a) and the GIXSGUI toolkit.

To obtain power conversion efficiency (PCE) of the fabricated solar cells, the *J-V* characteristics were collected in air atmosphere with a solar simulator SolarConstant1200 (K.H. Steuernagel Lichttechnik GmbH) equipped with a rare earth halogen lamp (AM1.5,

100 mWcm^{-2}). As shown in Figure 3.5, each cell contains 8 pixels. During solar cell measurements, a shadow mask with an illumination area of 0.12 cm^2 (each pixel) was used. The electric current density that flows through the solar cell, both under dark conditions and under simulated sunlight, was measured as a function of bias applied. A Keithley 2400 SourceMeter unit was used to apply bias and measure current simultaneously. In a standard *J-V* curve, maximum power point, P_{MP}, is defined by $P_{MP} = J_{MP} \times V_{MP}$ maximum. The fill factor, *FF*, is defined as the ratio between P_{MP} and the theoretical maximum power, $P_{max} = V_{oc} \times J_{sc}$

$$FF = \frac{P_{MP}}{P_{max}} = \frac{V_{MP}J_{MP}}{V_{oc}J_{sc}} \quad 3.3$$

where, V_{oc} is the open circuit voltage and J_{sc} is the short circuit current density.

The *PCE* is defined as the ratio of the device output power, P_{out}, to the irradiation input power, P_{in}

$$PCE = \frac{P_{out}}{P_{in}} = \frac{V_{oc}J_{sc}FF}{P_{AM1.5}} \quad 3.4$$

The PCE was obtained automatically from the instrument along with *J-V* curve.

3.3 Results and Discussion

3.3.1 Characterization of GeNPs

$Ge(OH)_2$ was synthesized by reduction of GeO_2 using hypophosphorus acid and it was converted to oxide embedded GeNP (GeNPs/GeO_x) composites upon thermal disproportionation at 400 °C under inert atmosphere.[51] After that, H-GeNPs were obtained by etching the GeO_x from GeNPs/GeO_x, then the H-GeNPs were functionalized by 1-dodecene through thermal hydrogermylation.[51]

The XRD of $Ge(OH)_2$ shows broad reflections, consistent with the presence of amorphous Ge (Figure 3.6).[37] The GeNPs/GeO_x shows reflections of crystalline Ge.[208] The reflections at 27.12°, 45.31°, 53.60°, 66.07°, 72.85°, and 83.71° correspond to cubic germanium (111), (220), (311), (400), (331), and (422) planes, respectively (PDF# 04-0545). Table 3.1 shows details of the phase, space group, cell parameters, and crystallite

size of GeNPs analyzed by Pawley refinement method. The functionalized dodecyl-GeNPs also show the presence of cubic germanium, with an average diameter of 6.03 nm.

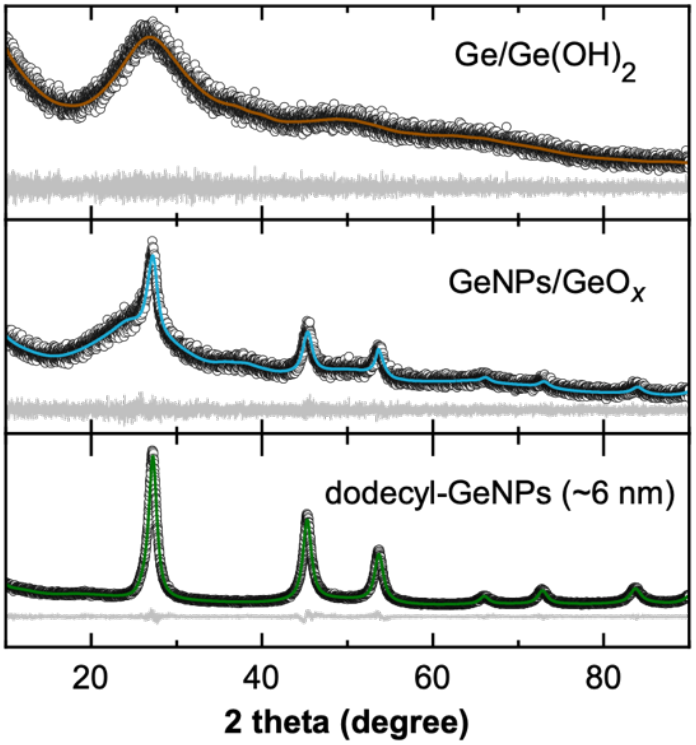

Figure 3.6. X-ray diffraction of $Ge(OH)_2$, GeNPs/GeO_x composite, and dodecyl-GeNPs.

Table 3.1. Crystallographic Refinement Data for Samples

Sample	$Ge(OH)_2$	Ge/GeO_x		Dodecyl-GeNPs 6.03 nm crystallite size
phase	Ge	Ge	GeO_x	Ge
space group	–	$Fd\bar{3}m$ (No. 227)	$P3_121$ (No. 152)	$Fd\bar{3}m$ (No. 227)
a (Å)	–	5.645(2)	5.01(3)	5.6522(2)
b (Å)	–	5.645(2)	5.01(3)	5.6522(2)
c (Å)	–	5.645(2)	5.65(6)	5.6522(2)
T (K)	296	296		296
radiation	Cu Kα, λ=1.5406 Å	Cu Kα, λ=1.5406 Å		Cu Kα, λ=1.5406 Å
2θ limits	10.00–90.00°	10.00–90.00°		10.00–90.00°
refinement method	Pawley	Pawley		Pawley
no. of data collected	8000 data points	8000 data points		8000 data points
no. of Bragg reflections	–	7		7
no. of variables	10	39		29
residuals[a]	R_{wp} = 0.0566	R_{wp} = 0.0713		R_{wp} = 0.0619
	R_{exp} = 0.0652	R_{exp} = 0.0701		R_{exp} = 0.0558
goodness of fit	1.32	1.02		1.11

[a] $R_{wp} = \left[\sum[w(y_o - y_c)]/\sum w y_o^2\right]^{1/2}$ $R_{exp} = [(N\text{-}P+C)/\Sigma(wy_o^2)]^{1/2}$; $R_{wp} = [\Sigma[w(y_o - y_c)] / \Sigma wy_o^2]^{1/2}$; N is the total number of observations, P is the number of parameters refined, C is the number of constraints used in the refinement.

Consistent with the XRD, the TEM of the dodecyl-GeNPs shows that the GeNPs are randomly shaped, with an average size of 6.82 ± 1.08 nm (Figure 3.7). The HRTEM (Figure 3.7a-inset) shows a d-spacing of 0.33 nm, consistent with a Ge (111) plane.[204] The size distribution was achieved by using the average shifted histogram (ASH) approach.[214]

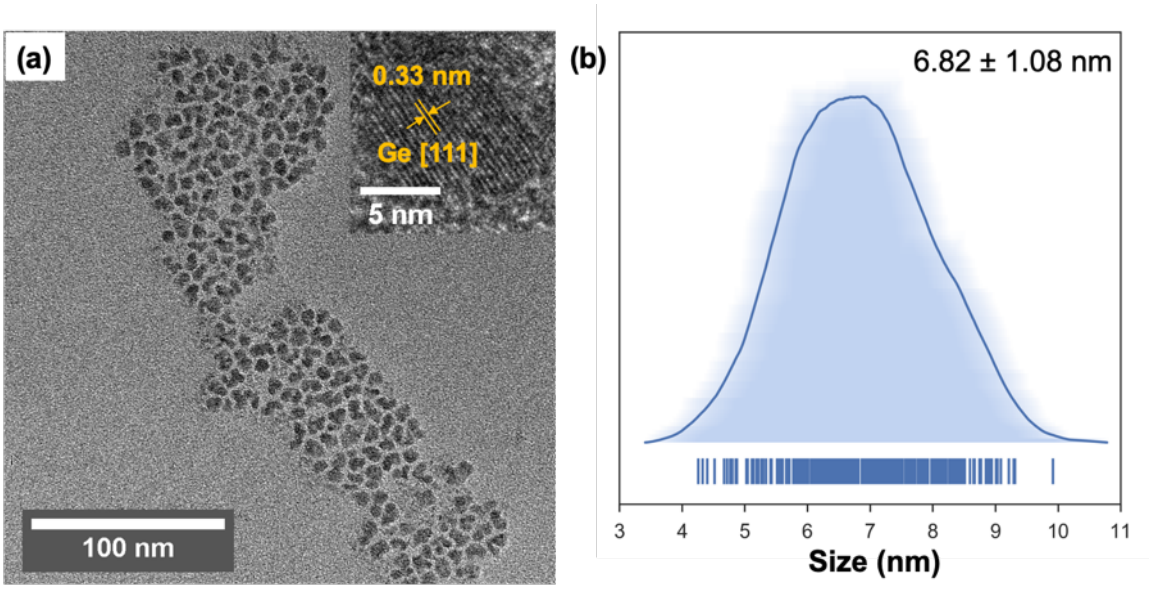

Figure 3.7. (a) Bright field TEM image (inset- HRTEM) and (b) average shifted histogram of dodecyl-GeNPs.

FTIR was employed to investigate the surface chemistry of GeNPs. Figure 3.8 illustrates that upon hydrogermylation reaction with H-GeNPs, the Ge-H stretching at *ca.* 2015 cm^{-1} is replaced with a C-H_x stretching and a bending frequency at *ca.* 2950–2850 cm^{-1} and *ca.* 1464 cm^{-1}, respectively, consistent with surface-bonded alkyl groups being introduced.

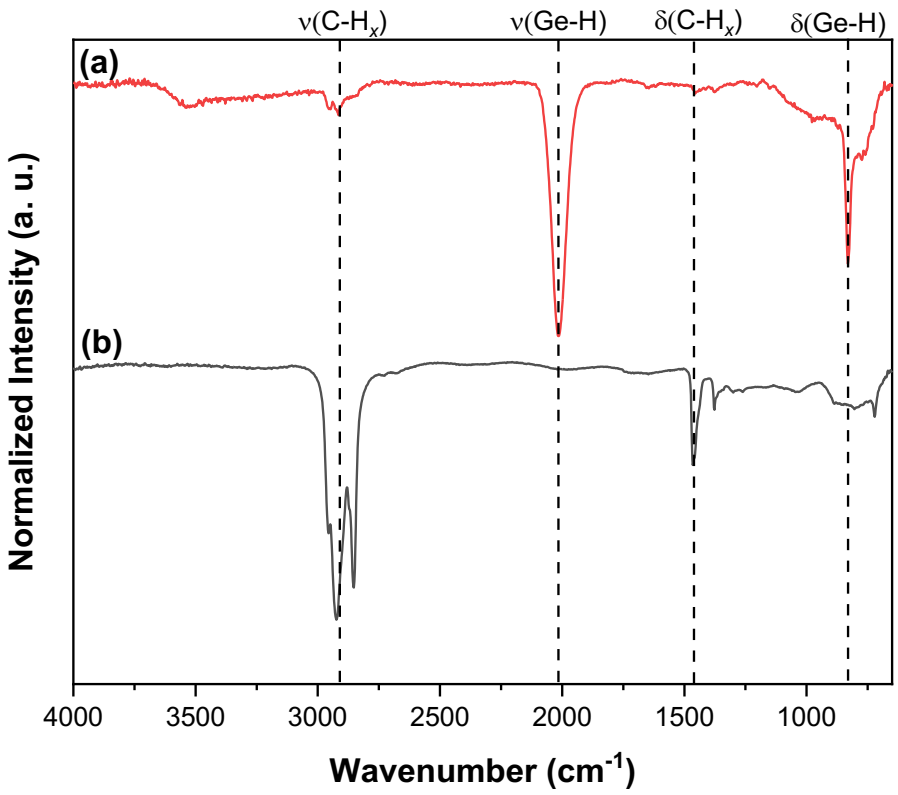

Figure 3.8. FTIR spectra of (a) H-GeNPs and (b) dodecyl-GeNPs.

3.3.2 Characterization of GeNP/PTB7-Th Thin Films

The dodecyl-GeNPs were mixed with the PTB7-Th polymer and deposited on Si and glass substrates as thin films. The thin films of PTB7-Th (PT), 0.1% Ge/PTB7-Th (0.1GPT), 0.3% Ge/PTB7-Th (0.3GPT), 0.5% Ge/PTB7-Th (0.5GPT), 0.7% Ge/PTB7-Th (0.7GPT), and 0.9% Ge/PTB7-Th (0.9GPT) were evaluated qualitatively using optical microscopy to obtain the film morphology. Figure 3.9 shows representative optical microscopic images of polymer blend thin films on Si substrates. All films exhibit smooth surfaces at the sensitivity of the imaging method, and there was no qualitative difference observed between samples.

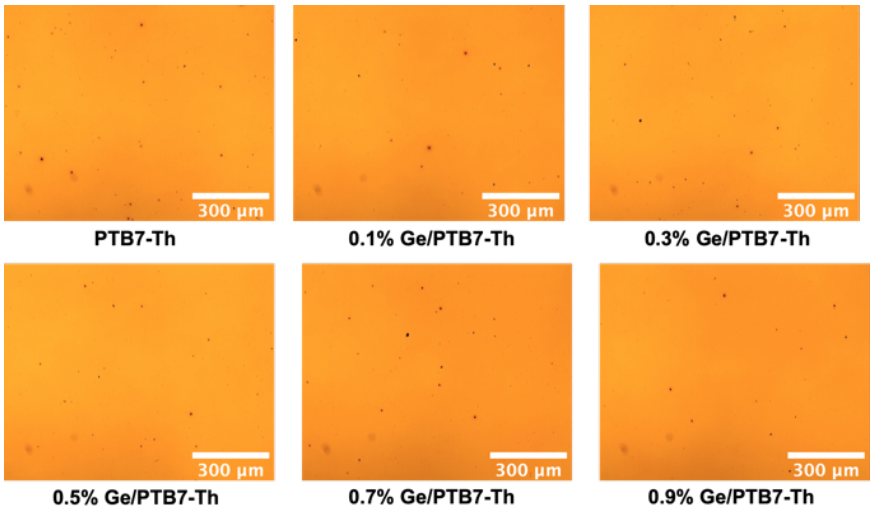

Figure 3.9. Optical microscopy images of PTB7-Th thin films containing 0, 0.1, 0.3, 0.5, 0.7, and 0.9% of GeNPs.

Atomic force microscopy (AFM) images of polymer blend thin films, shown in Figure 3.10, were analyzed by using Gwydion software. The mean roughness of PT, 0.1GPT, 0.3GPT, 0.5GPT, 0.7GPT, and 0.9GPT was 460.08 pm, 522.5 pm, 546.6 pm, 506.5 pm, 502.3 pm, and 594 pm, respectively. The root mean square (RMS) roughness of PT, 0.1GPT, 0.3GPT, 0.5GPT, 0.7GPT, and 0.9GPT was 585.6 pm, 724 pm, 748 pm, 693.3 pm, 694 pm, and 1052 pm, respectively. Consistent with the optical microscopy images, the mean roughness and RMS roughness of the thin films did not show any obvious trend (Figure 3.11).

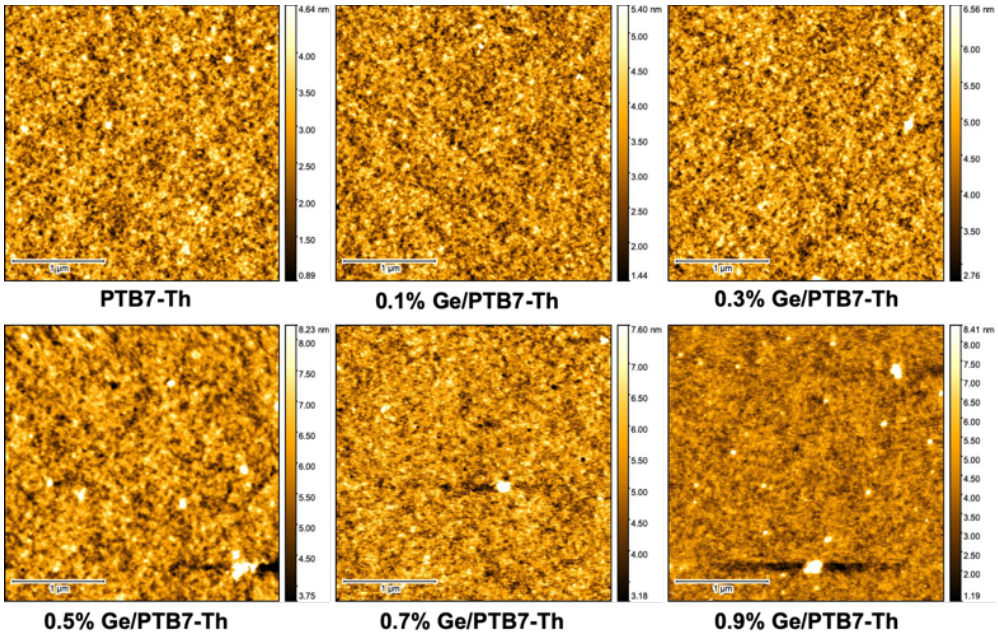

Figure 3.10. AFM images of PTB7-Th thin films with 0, 0.1, 0.3, 0.5, 0.7, and 0.9% of GeNPs.

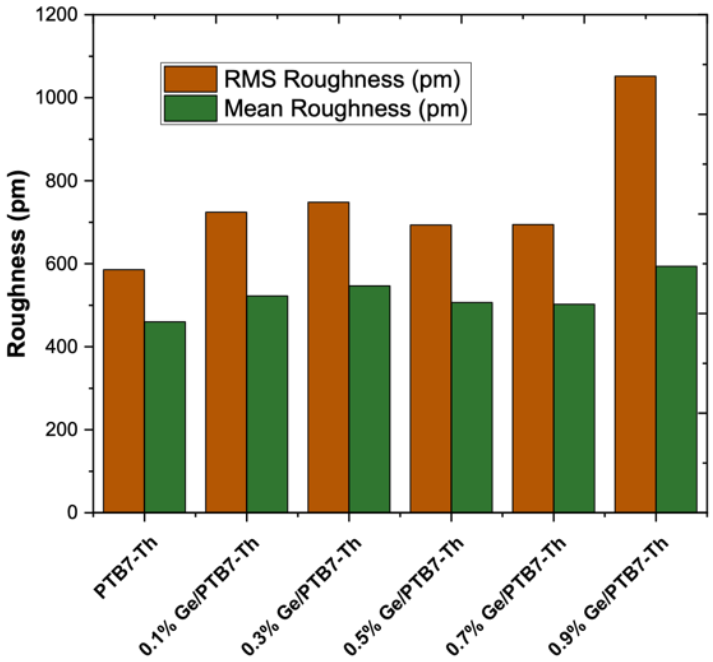

Figure 3.11. Mean roughness and RMS roughness of PTB7-Th thin films with 0, 0.1, 0.3, 0.5, 0.7, and 0.9% of GeNPs.

The thickness of the polymer blend films was measured by profilometry. The thickness of the films was in the range of 18–20 nm. The sheet resistance of the polymer blend films was measured by a four-point probe resistivity measurement equipped with a

Keithley 2400 SourceMeter. Later, the conductivity was calculated from the sheet resistance and thickness of the film and depicted in Figure 3.12. Upon addition of GeNPs, the conductivity shows a slight increase. This may be attributed to the higher carrier mobility of GeNPs.[247]

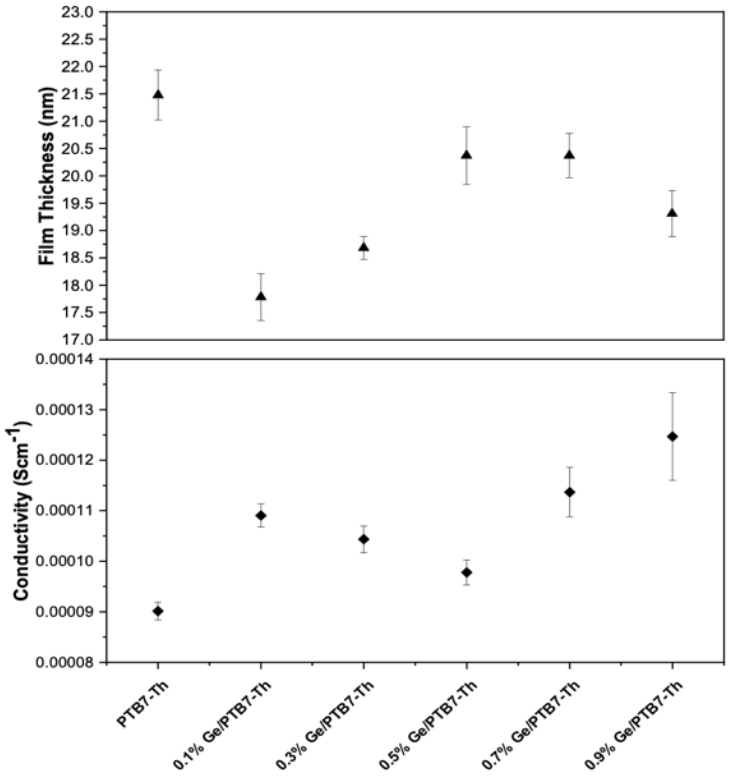

Figure 3.12. Film thickness and conductivity of PTB7-Th thin films with 0, 0.1, 0.3, 0.5, 0.7, and 0.9% of GeNPs.

The UV-vis absorption spectrum of PTB7-Th is consistent with the literature.[248] The spectra of the neat polymer and GeNP/polymer blends were normalized to the film thickness (Figure 3.13). It was noted qualitatively that the intensity of the absorbance of polymer blend films increased upon addition of GeNPs into PTB7-Th. This may be attributed to the scattering characteristics of GeNPs.[249]

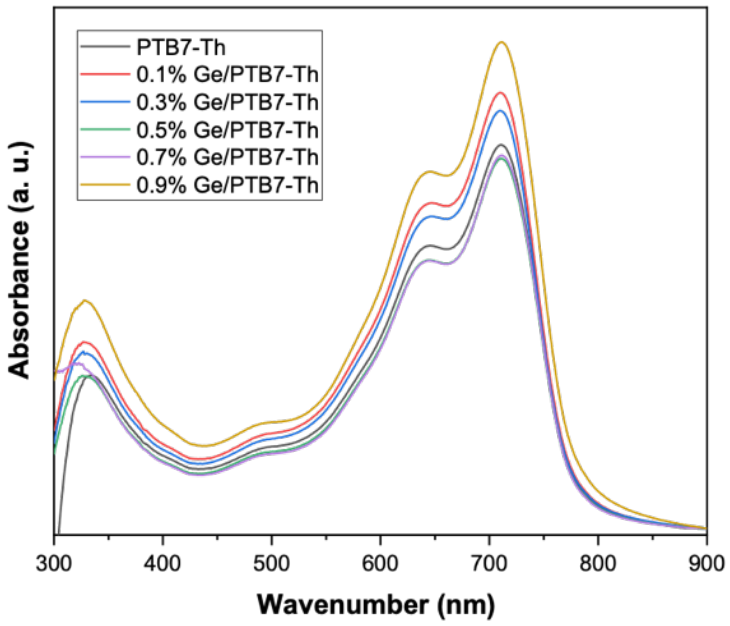

Figure 3.13. UV-vis absorption spectra of PTB7-Th thin films with 0, 0.1, 0.3, 0.5, 0.7, and 0.9% of GeNPs.

To obtain insight into the internal structure (i.e., crystallinity) of PTB7-Th, GIWAXS was performed (Figure 3.14 and 3.15). From the 2D GIWAXS data and the horizontal line cuts, a reflection is noted at *ca.* 0.27 $Å^{-1}$, which is documented as a face-on orientation (100) of PTB7-Th polymer crystallites.[148,248] The origin of a peak at *ca.* 0.41 $Å^{-1}$ is unknown and probably coming from an error during measurement. From the vertical line cut (out-of-plane), we observe a broad peak at *ca.* 1.55 $Å^{-1}$, which may arise from π-π stacking (010) of PTB7-Th. The π-π stacking PTB7-Th was observed at 1.6 $Å^{-1}$ in the literature.[148,248] The other sharp peaks may arise from metal impurities during the measurement. The addition of GeNPs did not show any obvious change in the crystallinity of PTB7-Th.

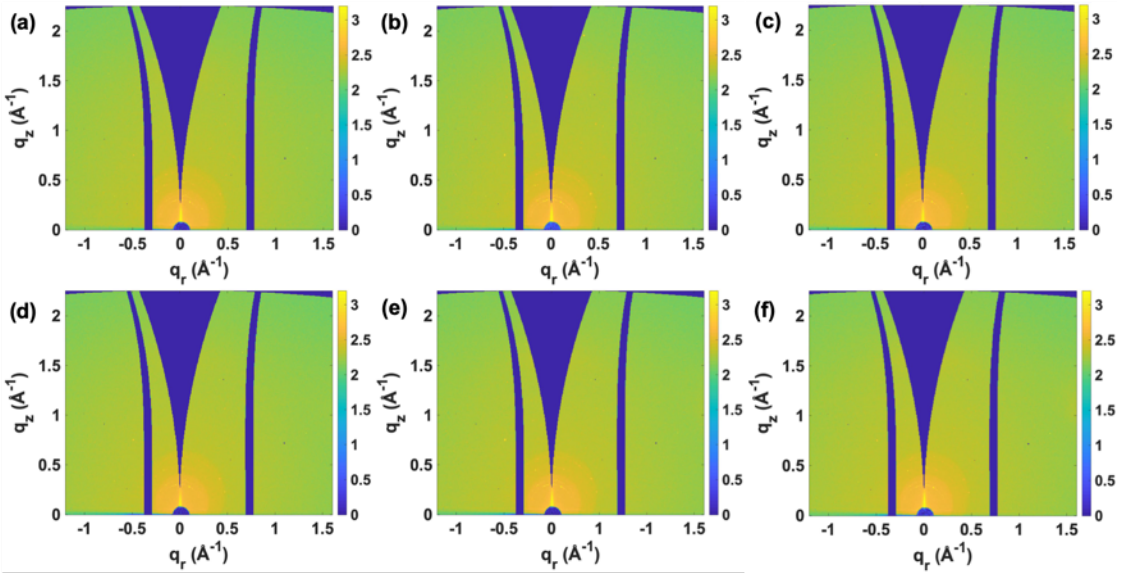

Figure 3.14. Grazing incidence wide angle X-ray scattering (GIWAXS) spectra of (a) PT, (b) 0.1GPT, (c) 0.3GPT, (d) 0.5GPT, (e) 0.7GPT, and (e) 0.9GPT thin films. Two curved blue stripes at q_y = -0.3 Å^{-1} and 0.7 Å^{-1} are due to the intermodular detector gaps.

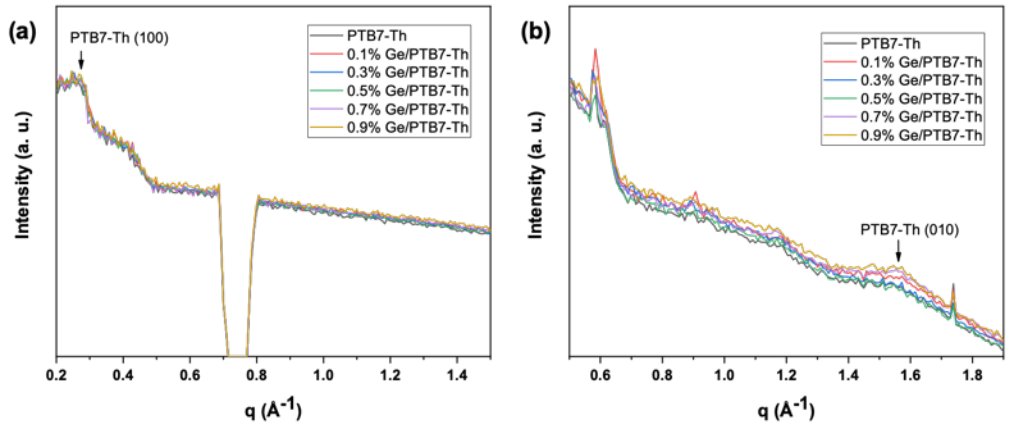

Figure 3.15. (a) Horizontal (in-plane) and (b) vertical (out-of-plane) line cuts of 2D GIWAXS data for PTB7-Th with different proportions of GeNPs.

To obtain information about the inner morphology of the present thin films, GISAXS data were acquired (Figure 3.16). GISAXS can provide information about polymer domain sizes and spatial correlations down to nanometer scales. To obtain quantitative information, horizontal line cuts were performed on the 2D GISAXS data at the Yoneda peak position of PTB7-Th. As the horizontal cuts were performed along the q_y direction, the information about lateral structures e.g., polymer domain sizes and center-

to-center distance of those domains can be found upon appropriate fitting of Figure 3.17. The fitting and the corresponding calculations will be done in future.

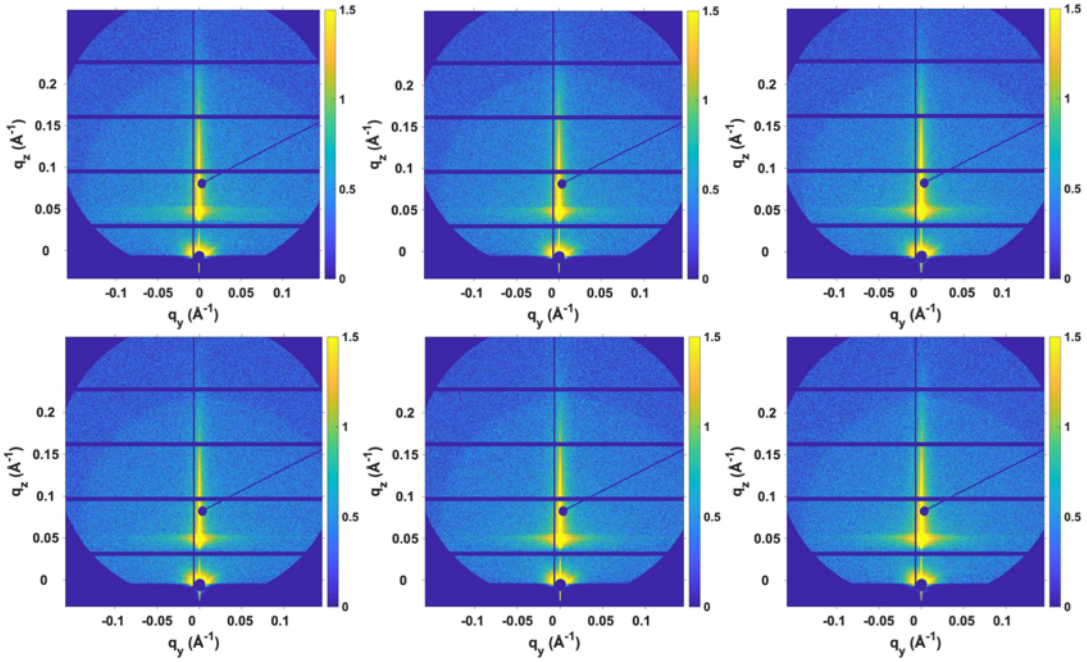

Figure 3.16. Grazing incidence wide angle X-ray scattering (GIWAXS) spectra of (a) PTB7-Th, (b) 0.1% Ge/PTB7-Th, (c) 0.3% Ge/PTB7-Th, (d) 0.5% Ge/PTB7-Th, (e) 0.7% Ge/PTB7-Th, and (e) 0.9% Ge/PTB7-Th thin films.

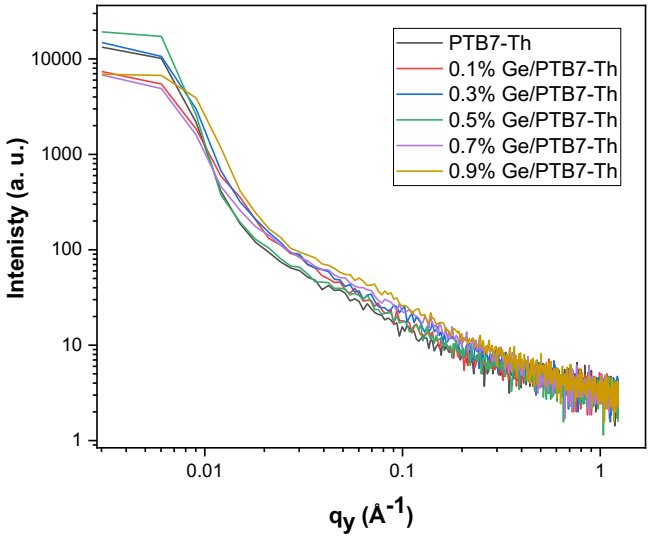

Figure 3.17. Horizontal (in-plane) line cuts of 2D GISAXS data for PTB7-Th with different proportions of GeNPs.

3.3.3 Characterization of GeNPs/PTB7-Th/IT-4F Thin Films

Thin films of PTB7-Th/IT4F (PTI), 0.1% Ge/PTB7-Th/IT-4F (0.1GPTI), 0.3% Ge/PTB7-Th/IT-4F (0.3GPTI), 0.5% Ge/PTB7-Th/IT-4F (0.5GPTI), 0.7% Ge/PTB7-Th/IT-4F (0.7GPTI), and 0.9% Ge/PTB7-Th/IT-4F (0.9GPTI) were characterized by optical microscopy to obtain the film morphology. Figure 3.18 shows optical microscopic images of polymer hybrid thin films on Si substrates. Similar to PTB7-Th (Figure 3.9), the PTB7-Th/IT-4F active layer exhibits a smooth surface, and the GeNPs (0.1–0.9%) did not show any obvious change in the surface smoothness.

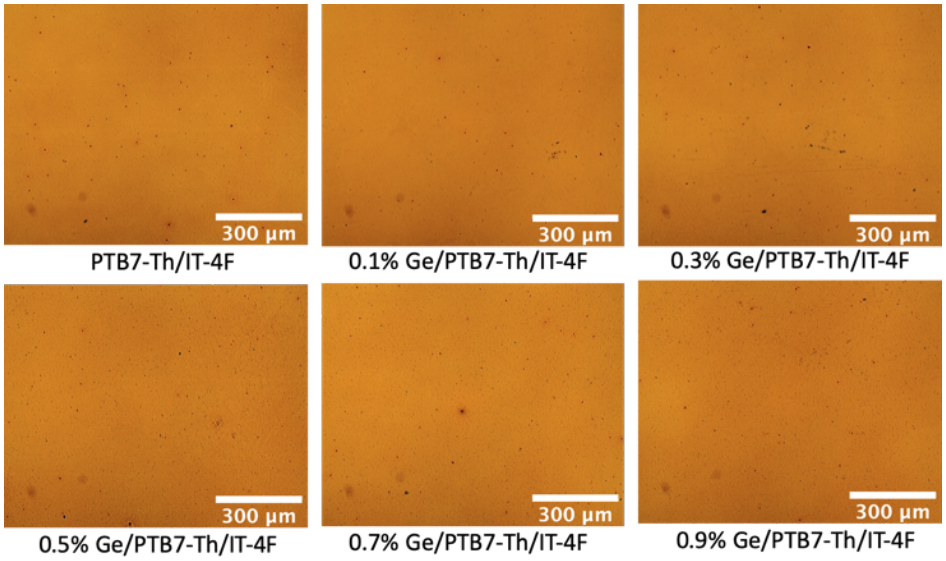

Figure 3.18. Optical microscopy images of PTB7-Th/IT4F thin films with 0, 0.1, 0.3, 0.5, 0.7, and 0.9% of GeNPs.

Atomic force microscopy (AFM) of polymer hybrid thin films are shown in Figure 3.19. The images were analyzed by using Gwydion software. In Figure 3.20, the mean roughness of PTI, 0.1GPTI, 0.3GPTI, 0.5GPTI, 0.7GPTI, and 0.9GPTI was 4.6 nm, 3.6 nm, 3.9 nm, 4.5 nm, 3.3 nm, and 4.2 nm, respectively. The root mean square (RMS) roughness of PTI, 0.1GPTI, 0.3GPTI, 0.5GPTI, 0.7GPTI, and 0.9GPTI was 5.9 nm, 4.9 nm, 5.1 nm, 5.9 nm, 4.1 nm, and 5.4 nm, respectively. Compared to bare PTB7-Th thin-films, the surface roughness of PTB7-Th/IT-4F has increased, however, the addition of GeNPs did not influence the roughness, consistent with optical microscopy.

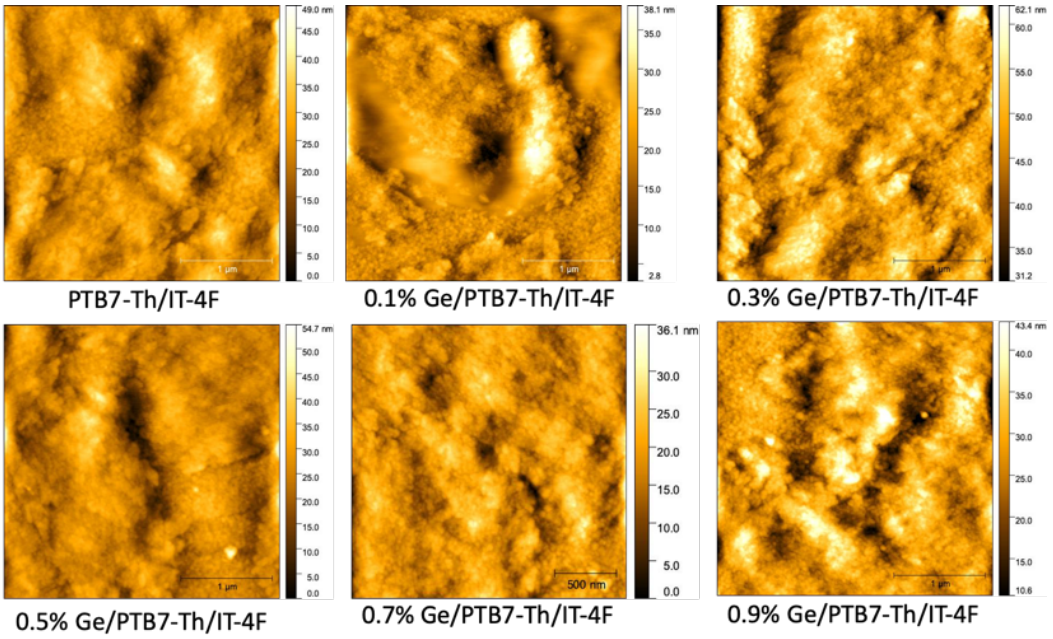

Figure 3.19. AFM images of PTB7-Th/IT4F thin films with 0, 0.1, 0.3, 0.5, 0.7, and 0.9% of GeNPs.

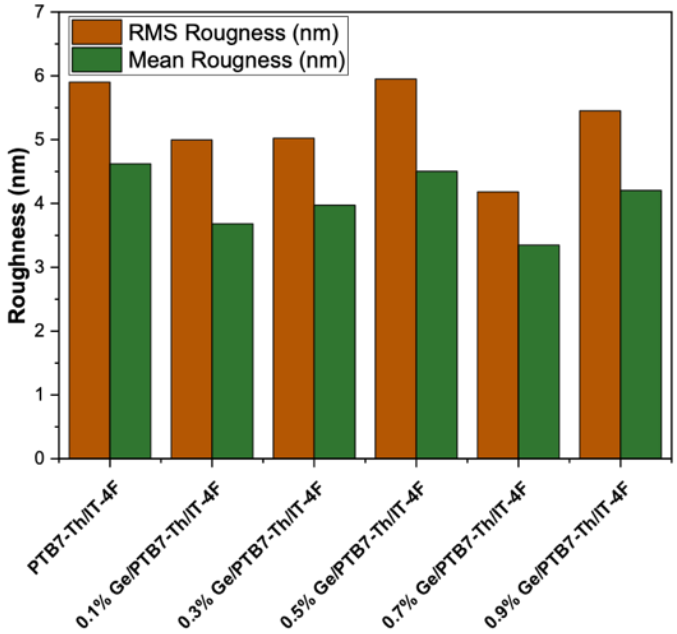

Figure 3.20. Mean roughness and RMS roughness of optical microscopy images of PTB7-Th/IT4F thin films with 0, 0.1, 0.3, 0.5, 0.7, and 0.9% of GeNPs.

The thickness and conductivity of the active layer are shown in Figure 3.21. Upon addition of GeNPs, the conductivity shows a slight increase at first and then decreases. The

increase in film conductivity can be attributed to the higher carrier mobility of GeNPs as observed in the literature.[247]

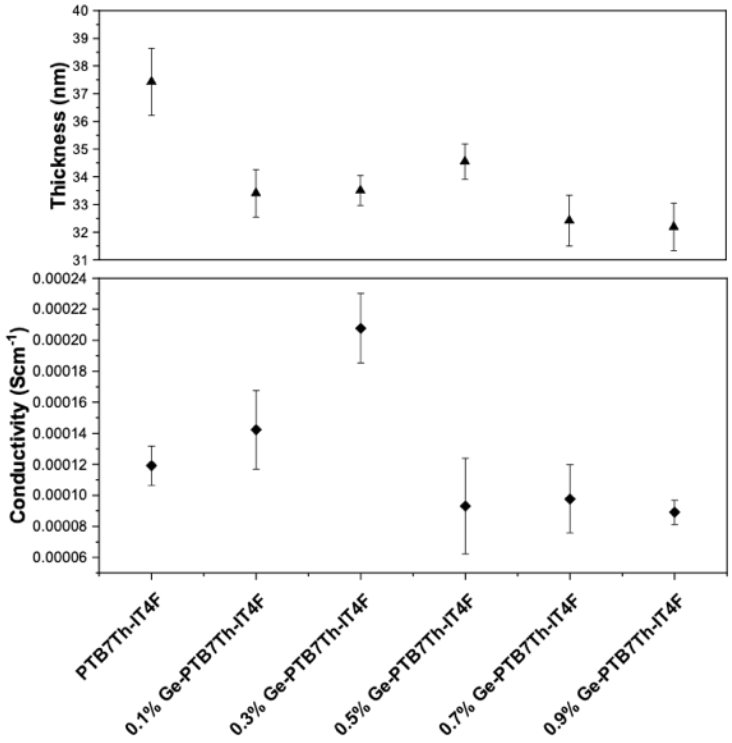

Figure 3.21. Film thickness and conductivity of PTB7-Th/IT-4F thin films with 0, 0.1, 0.3, 0.5, 0.7, and 0.9% of GeNPs.

The UV-vis absorption spectra of PTB7-Th/IT-4F are given in Figure 3.22. The spectra were normalized by the corresponding film thickness. It was noted qualitatively that the intensity of the absorbance of polymer blend thin films increased upon addition of GeNPs into PTB7-Th/IT-4F. This may be attributed to the scattering characteristics of GeNPs.[249]

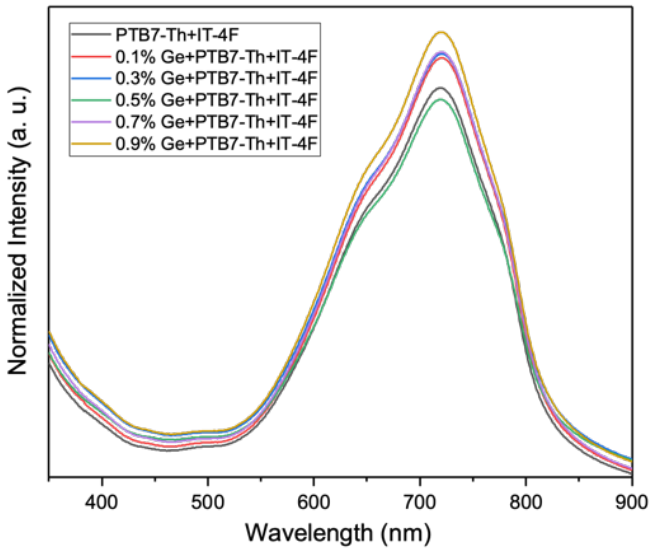

Figure 3.22. UV-vis absorption spectra of PTB7-Th/IT4F thin films with 0, 0.1, 0.3, 0.5, 0.7, and 0.9% of GeNPs.

The GIWAXS of the donor-acceptor blend (active layer) shows more clear scattering of π-π stacking (010) of PTB7-Th compared to the bare PTB7-Th film without acceptor materials (Figure 3.23). The face-on orientation (100) of PTB7-Th that is present in the horizontal line cuts is at *ca.* 0.27 $Å^{-1}$ (Figure 3.24a). Interestingly, the π-π stacking reflections have shifted with the addition of GeNPs (Figure 3.24b). It is unclear why the spacing of π-π interaction polymer films will change due to the addition GeNPs. It might be due to an experimental error because there were some sharp reflections observed that surely are metal impurities. Even the IT-4F did not show its characteristic broad reflections at 0.4 and 1.8 $Å^{-1}$, as given in the literature.[250]

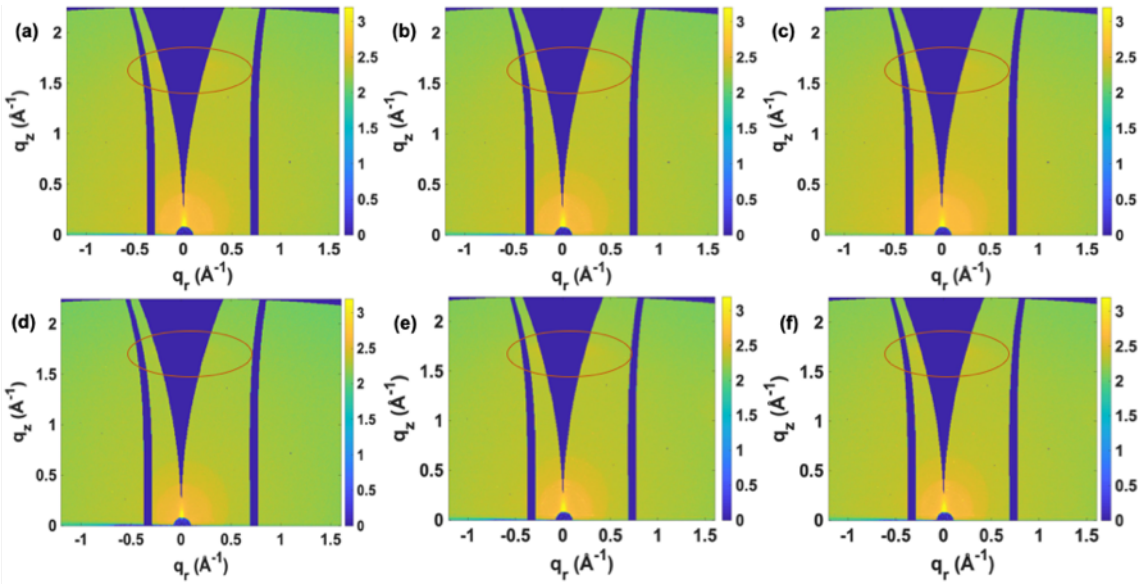

Figure 3.23. GIWAXS images of PTB7-Th/IT4F thin films with (a) 0, (b) 0.1, (c) 0.3, (d) 0.5, (e) 0.7, and (f) 0.9% of GeNPs (red circle represents (010) plane of PTB7-Th for π-π stacking). Two curved blue stripes at q_y = -0.3 Å^{-1} and 0.7 Å^{-1} are due to the intermodular detector gaps.

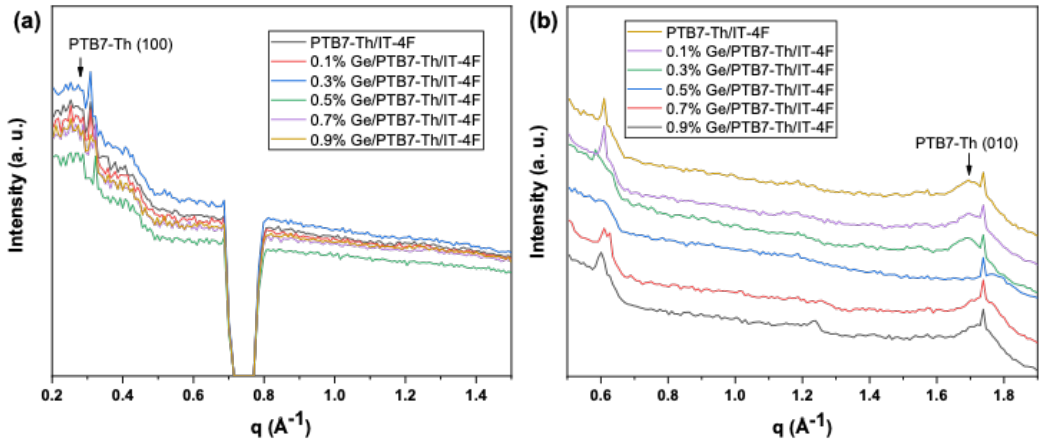

Figure 3.24. (a) Horizontal (in-plane) and (b) vertical (out-of-plane) line cuts of 2D GIWAXS data for PTB7-Th/IT-4F with different proportion of GeNPs.

The 2D GISAXS images of the active layer and their horizontal cuts were performed along the q_y direction to obtain information about lateral structures i.e., the polymer domain sizes and center-to-center distance of those domains (Figure 3.25 and 3.26). The lines need to be fitted and modeled using local monodisperse approximation (LMA) to obtain that information; this will be done in future.

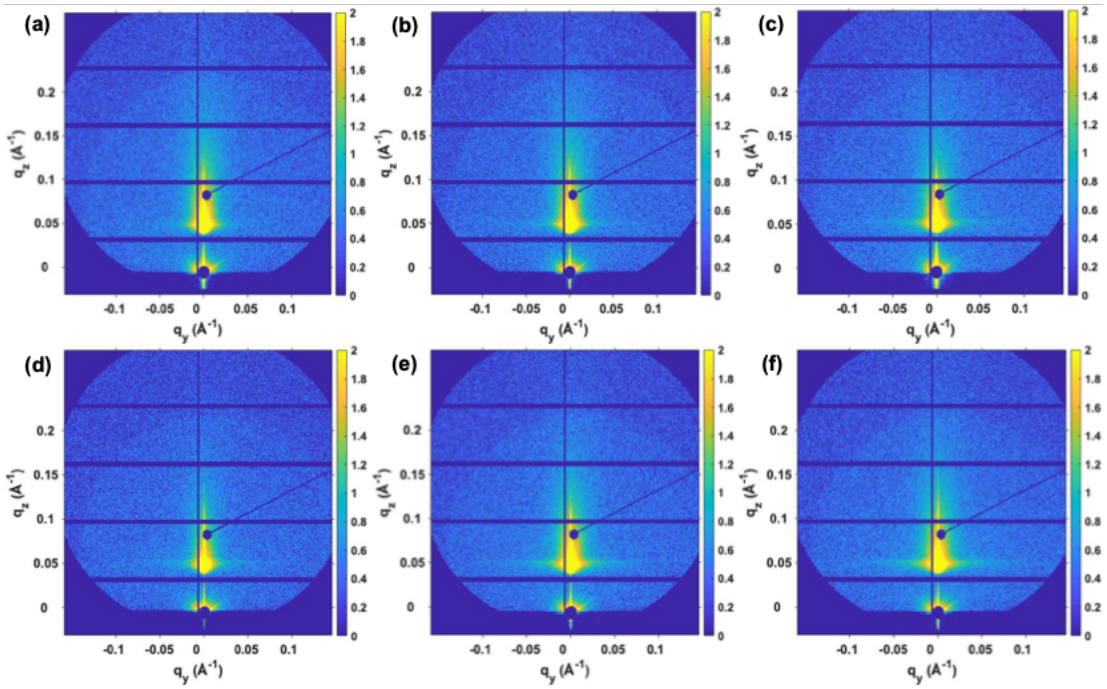

Figure 3.25. GISAXS images of PTB7-Th/IT4F thin films with 0%, 0.1%, 0.3%, 0.5%, 0.7%, and 0.9% of GeNPs.

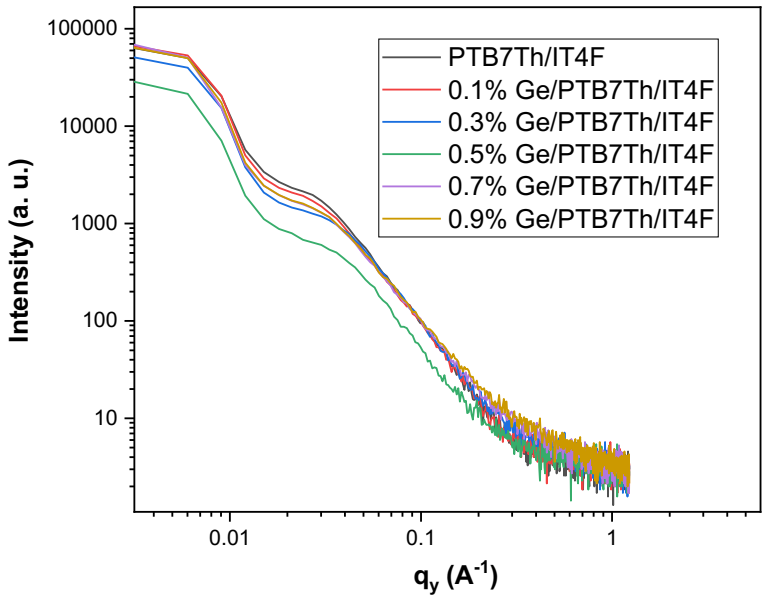

Figure 3.26. Horizontal line cuts of GISAXS images of PTB7-Th/IT4F thin films with 0, 0.1, 0.3, 0.5, 0.7, and 0.9% of GeNPs.

3.3.4 Performance of Solar Cells

Three compositions of inverted polymer solar cells were fabricated with PTB7-Th and IT-4F (1:1 ratio) having 0%, 0.3% and 0.9% GeNPs; these are denoted as PTI, 0.3PT, and

0.9PTI, respectively. The device performance measured under simulated AM 1.5 illumination at 100 mWcm^{-2} is summarized in Table 3.2, and current density versus voltage (*J-V*) curves are shown in Figure 3.27. For each solar cell type, three cells were measured, with each cell containing 8 pixels. Some pixels appeared to be dead (0% Power Conversion Efficiency (PCE)) during measurement. The J_{sc}, V_{oc}, fill factor, lowest PCE, highest PCE, and average PCE for all cells are summarized in Table 3.2. The PCE of 0.3PTI was better than PTI, however, when GeNPs increased to 0.9% (0.9PTI), the PCE decreased. These results are similar to the work of Gonzalez et al.,[251] where Fe_3O_4 nanoparticles were used as dopant in P3HT-PC_{60}BM solar cells. The author observed that at a higher concentration of Fe_3O_4 (>0.6%), the performance of the solar cell decays because of the increased leakage currents due to the presence of nanoparticles.

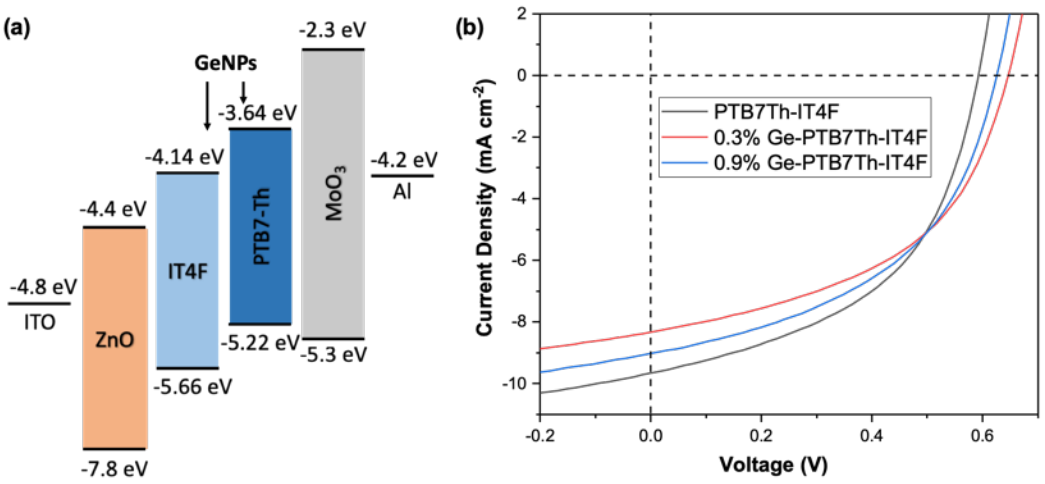

Figure 3.27. (a) Schematic energy level diagram and (b) current density versus voltage (*J-V*) curves of the solar cell devices.

Table 3.2. Summary of the Device Performance Under 100 mWcm^{-2} Simulated AM 1.5 Illumination

	Number of pixels studied	Number of dead pixels	J_{sc} (mA cm^{-2})	V_{oc} (V)	*FF* (%)	Lowest *PCE* (%)	Highest *PCE* (%)	*PCE* (%)
PTI	24	14	-7.1617	0.3941	35.44	0.345	2.82	1.13
0.3GPTI	24	10	-7.9376	0.4832	39.38	0.483	2.59	1.59
0.9GPTI	24	10	-7.0071	0.4995	34.04	0.226	2.67	1.34

3.4 Conclusion and Future Outlook

A new combination polymer donor and small molecule acceptor, such as PTB7-Th and IT-4F, have been used to obtain a better performance of solar cells. GeNPs were used to improve the optical and electrical performance of the active layer. The thin films were characterized by optical microscopy and AFM to obtain information about morphology. GIWAXS and GISAXS were performed to obtain a deeper understanding of their crystallinity and inner morphology. Thus, the inorganic/polymer hybrids offer a new pathway to improve polymer solar cells.

In future, the GIWAXS and GISAXS need to be repeated. There were technical faults in the measurements and, therefore, the expected scattering did not appear in the 2D GIWAXS and GISAXS images. Moreover, there were some sharp reflections that may be due to metal impurities. Modeling should be done on the GISAXS data to obtain polymer domain sizes and their distance.

The device characterizations need to be repeated as well because the solar simulator was not performing up to the mark. More solar cells need to be fabricated to get better statistical data of the performance. The thickness of active layers as well as charge transport layers can be changed.

Dodecyl-GeNPs may not be the best choice for the solar cell since the dodecyl group is insulating. Instead, a conductive GeNP surface should be synthesized and used for the solar cell. H-terminated GeNPs may also be used.

Chapter 4

Inductive Heating to Synthesize a Uniform Size and Shape of Germanium Nanoparticles

4.1 Introduction

Nanoparticles with a uniform shape and size distribution are very important because their application depends on the unique opto-electronic properties governed by their size and shape.[252] Germanium based nanomaterials are very promising for opto-electronic application due to their large exciton Bohr radius (*ca.* 24 nm), narrow band gap (*ca.* 0.67 eV in bulk), high carrier mobility, and high absorption coefficient (*ca.* 2.0×10^5 cm^{-1} at 2 eV).[41,232] Several morphologies of germanium nanomaterials have been studied over the past years, including colloidal nanoparticles,[25,62] nanowires,[253,254] nanocubes,[255] and nanosheets.[256,257]

Several synthesis strategies were developed by researchers to obtain germanium nanoparticles (GeNPs), but controlling their size and shape is still a challenge.[25] Muthuswamy et al.[45] synthesized GeNPs via microwave heating of germanium iodides (GeI_2/GeI_4) with strong reducing agents ($LiAlH_4$, n-BuLi, $NaBH_4$). The authors were able to synthesize GeNPs with wide a range of sizes (4–10 nm), however, the particle shapes were random (Figure 4.1).

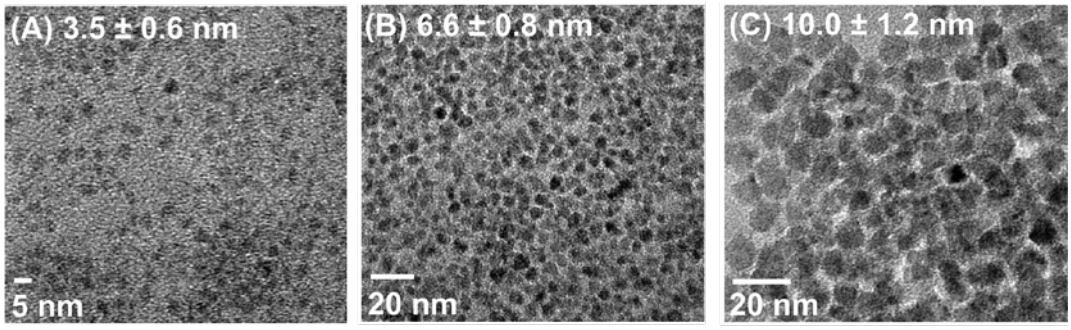

Figure 4.1. Bright field TEM image of GeNPs obtained by microwave synthesis using a different ratio of GeI_2/GeI_4 precursor: (A) 0.4 mmol GeI_2, (B) 0.3/0.1 mmol, and (C) 0.2/0.2 mmol.[45] Reprinted with permission from reference 45. Copyright 2013 American Chemical Society.

Prabakar et al. synthesized GeNPs by reduction of $GeCl_4$ with lithium aluminum hydride ($LiAlH_4$), lithium triethyl borohydride ($Li(C_2H_5)_3BH$), lithium borohydride ($LiBH_4$), and sodium borohydride ($NaBH_4$).[40] They obtained fairly monodisperse particles 4–5.5 nm, but the shape of the GeNPs was random. Figure 4.2 shows TEM images of allylamine passivated GeNPs obtained from reduction by $LiAlH_4$, $Li(C_2H_5)_3BH$, $LiBH_4$, and $NaBH_4$.

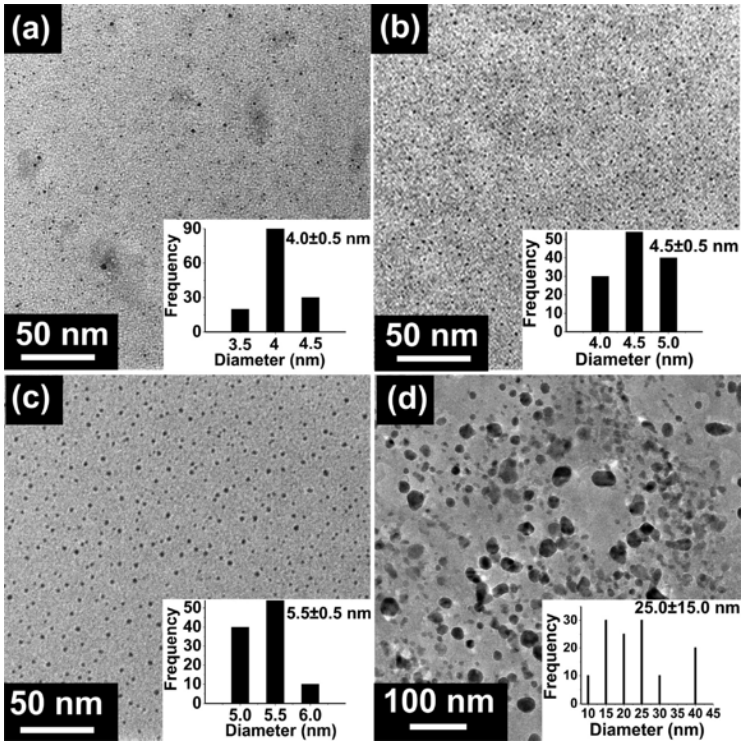

Figure 4.2. Bright field TEM image of GeNPs obtained by reduction of $GeCl_4$ by (a) $LiAlH_4$, (b) $Li(C_2H_5)_3BH$, (c) $LiBH_4$, and (d) $NaBH_4$.[40] Reprinted with permission from reference 40. Copyright 2010 American Chemical Society.

In our lab, a new synthesis strategy for Ge nanoparticles (GeNPs) was developed by Javadi et al.,[51] in which a GeNPs/GeO_x composite was synthesized by thermal disproportionation of $Ge(OH)_2$. The GeO_x was etched by HF to release H-terminated GeNPs and was passivated by alkene through thermal and radical initiated hydrogermylation. A bright-field TEM image of dodecyl passivated GeNPs is shown in Figure 4.3. The GeNPs were randomly shaped and there was little control over size and shape.

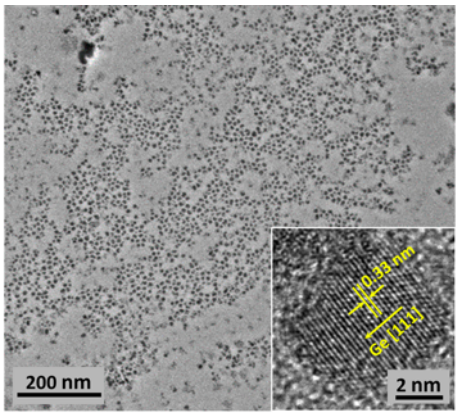

Figure 4.3. Bright field TEM image of dodecyl-GeNPs obtained by thermal hydrogermylation of H-GeNPs by 1-dodecene (inset: HRTEM).[51] Reprinted with permission from reference 51. Copyright 2017 American Chemical Society.

It can be concluded from the different synthesis strategies that it is difficult to synthesize GeNPs with uniform shapes from chemical synthesis.[62] However, the non-thermal plasma synthesis gives uniformly faceted GeNPs, as shown in Figure 4.4.[258] In a non-thermal plasma synthesis, the high energy electrons from plasma dissociates, ionizes the gaseous precursor molecule, and forms highly reactive radicals and ions.[259] These radicals and ions react exothermally to nucleate nanoparticles, followed by coagulation and surface growth of charged particles. To obtain small nanoparticles, it is essential to separate nucleation from growth by tuning the conditions of plasma and the amount of precursor.

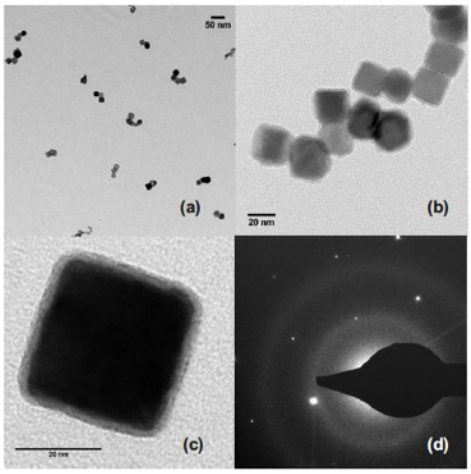

Figure 4.4. (a, b, c) Bright field TEM images and (d) selected area electron diffraction (SAED) of GeNPs obtained by non-thermal plasma synthesis from $GeCl_4$. Reprinted with permission from reference 259. Copyright 2007 American Chemical Society.

Recently, Yu et al. synthesized a morphology-controlled cubooctahedral superlattice of silicon nanocrystals by annealing hydrogen silsesquioxane (HSQ) with a periodic heating and cooling cycle (Figure 4.5). In addition to taking a long time to obtain the desired size and shape using a conventional tube furnace, the temperature of such a furnace is not accurate and often overshoots at 300–600 °C.[260] We hypothesize that it may be possible to separate the nucleation from growth by rapidly heating and cooling and to synthesize nanoparticles with a uniform shape and size distribution.

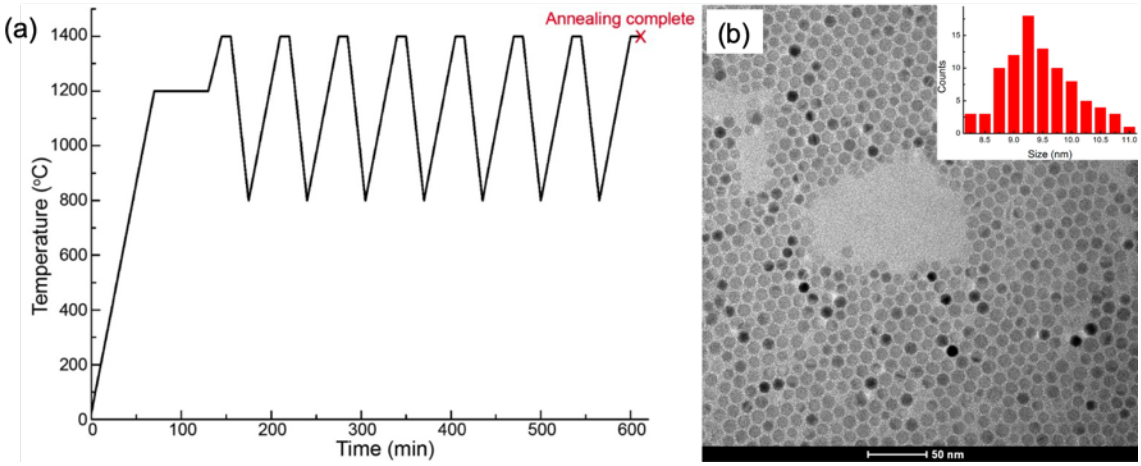

Figure 4.5. (a) Temperature profile of the HSQ decomposition process used to obtain Si nanocrystals with cuboctahedral shape and (b) bright field TEM image of size-selected Si nanocrystals, with a size histogram at the top right corner. Reprinted with permission from reference 261. Copyright 2016 American Chemical Society.

Induction heating has become quite useful in the scientific field, especially for therapeutic applications where magnetic nanoparticles are used to heat and destroy tumor/cancer cells.[261] It also is used as the heating technology in industry as well as in the laboratory.[262] Figure 4.6 shows a typical arrangement of an inductive heating system. An alternating current (AC) source is used to generate an alternating voltage to the inductor coil.[262] The coil generates an alternating magnetic field in the middle of which an induction target is placed. The induction target is heated by two physical phenomena, eddy currents and magnetic hysteresis. Eddy currents oppose the magnetic field applied to the induction target; therefore, they produce heat by the Joule effect.[263] Magnetic hysteresis creates additional heating in ferromagnetic materials. The advantage of induction heating over

conventional heating is that it gives efficient, controlled, fast, and safe heating since it only heats the target. Therefore, it is the choice of heating technology in industrial, domestic, and medical applications.[262]

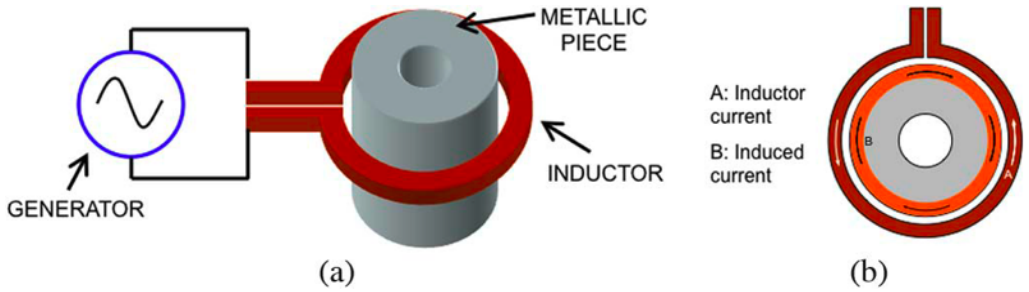

Figure 4.6. Typical arrangement of an induction heating system: (a) general view and (b) top view. Reprinted with permission from reference 18. Copyright 2013 IEEE.

In this work, induction heating was used as a tool to synthesize GeNPs with uniform shape. A graphite crucible was heated inductively by a magnetic field, and the heat was transferred to $Ge(OH)_2$ to synthesize GeNPs/GeO_x under an inert atmosphere. Interestingly, at high temperature, germanium acts as a conductor, which further acts as an induction target and heats the semiconductor internally. The advantage of induction heating over a conventional tube furnace is that it is possible to perform fast heating and also fast cooling by using a cooling jacket.[264] Photographs of an induction heating setup are shown in Figure 4.7. An EASYHEAT LI induction heating system was used with inert gas and cooling water.

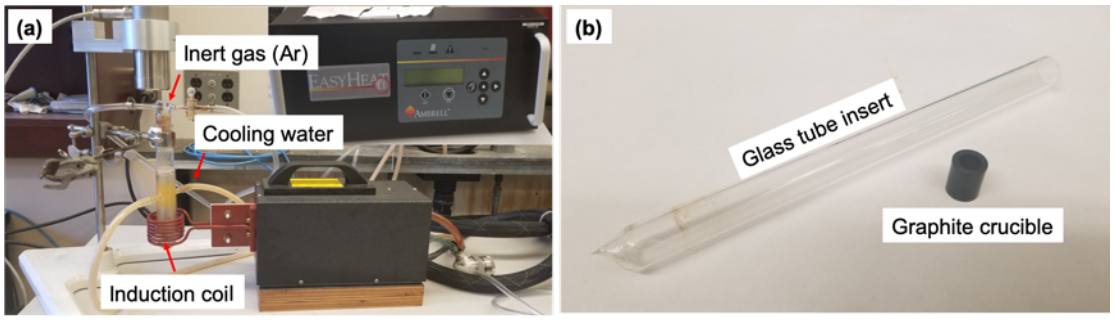

Figure 4.7. Photographs of (a) an inductive heating system and (b) a graphite crucible with a glass insert.

4.2 Experimental

4.2.1 Reagents and Materials

Germanium dioxide powder (GeO_2, 99.9%) was purchased from Gelest. Hypophosphorous acid (50 wt% in water), sodium hydroxide pellets, 1-dodecene (95%), and toluene (99.9%, HPLC grade) were purchased from Sigma-Aldrich. Toluene was purified using a Pure-Solv purification system and collected immediately prior to use. Hydrochloric acid (36.5–38.0 %) and ammonium hydroxide (28–30%) were purchased from Caledon Labs. Electronics grade hydrofluoric acid (HF, 49 % aqueous solution) was purchased from J. T. Baker. Ultrapure H_2O (18.2 MΩ/cm) was obtained from a Barnstead Nanopure Diamond purification system and was used in all reactions. Molecular sieves (4 Å) were purchased from Sigma-Aldrich and activated in a vacuum oven prior to use.

4.2.2 Preparation of $Ge(OH)_2$

$Ge(OH)_2$ was synthesized by reduction of GeO_2 using hypophosphorus acid.[208] Briefly, 2.0 g of GeO_2 were dissolved in 14 mL freshly prepared aqueous NaOH (~17 M). Then, HCl (6 M, 48 mL) was added dropwise to the GeO_2 solution to achieve a pH of ~1. Next, hypophosphorus acid in water (50 wt% H_3PO_2; 15 mL) was added, and the mixture was refluxed for 5.5 h under argon. After that, conc. NH_4OH (20 mL) was added to the boiling reaction mixture to yield a brown precipitate that was isolated by vacuum filtration and washed three times with 10-mL aliquots of ultrapure water. After drying in a vacuum oven at 70 ˚C for 15 h, *ca.* 1.6 g of 'brown $Ge(OH)_2$' were obtained.

4.2.3 Preparation of GeNPs/GeO_x from $Ge(OH)_2$

GeNPs embedded in a germanium oxide matrix (GeNPs/GeO_x) were prepared by the two following methods:

(a) About 100 mg of $Ge(OH)_2$ were transferred into a graphite crucible, placed into an induction heating chamber using a glass insert, and an Ar flow was applied (Figure 4.7). Then, a current was applied through the copper coil to produce a magnetic flux and corresponding eddy currents, which heat the graphite crucible.[264] The obtained

GeNPs/GeO_x were used for reactions and characterization.

(b) About 2 g of $Ge(OH)_2$ were transferred into a quartz boat, placed into a Lindberg tube furnace, and heated at 400 ºC for 1 h under flowing Ar. The resulting GeNPs/GeO*x* were heated in the induction furnace according to the procedure described above. The specific conditions of heating are described in Section 4.3.

4.2.4 Isolation of Hydride-terminated GeNPs

Hydride-terminated GeNPs (H-GeNPs) were liberated from the GeNP/GeO_x via ethanolic hydrofluoric acid (HF) etching using a literature procedure.[51] See Section 2.2.3 for details.

4.2.5 Hydrogermylation of H-GeNPs Surfaces

An established literature procedure was employed to modify GeNP surfaces via thermally-induced hydrogermylation.[51] See Section 3.2.4 for details.

4.2.6 Materials Characterization and Instrumentation

X-ray Diffraction (XRD), bright-field transmission electron microscopy (TEM), and high-resolution TEM (HRTEM) were employed to characterize the GeNPs. See Section 2.2.6 for the details of characterization and instrumentation.

4.3 Results and Discussion

4.3.1 GeNPs/GeO_x from $Ge(OH)_2$ by Induction Heating

$Ge(OH)_2$ was prepared by reducing GeO_2 with hypophosphorus acid using the literature procedure developed in our group.[208] Then, $Ge(OH)_2$ was heated inductively using a graphite crucible with 151.2, 161.7, and 170.1 A currents for 30 min. The diffraction patterns of $Ge(OH)_2$ and GeNPs/GeO_x prepared at different currents are shown in Figure 4.8. The $Ge(OH)_2$ shows broad reflection of the amorphous oxides. At a current of 151.2 A, reflections at 27.4º, 45.7º, 54.1º, 66.2º, 73.4º, and 83.6º appeared, which can be attributed to the 111, 220, 311, 400, 331, and 422 planes of cubic germanium, respectively.[204] At a current of 161.7 A, the reflections of germanium became sharp,

consistent with the growth of nanocrystals. At 170.1 A, reflections from GeO_2 appeared along with the crystalline Ge.[265]

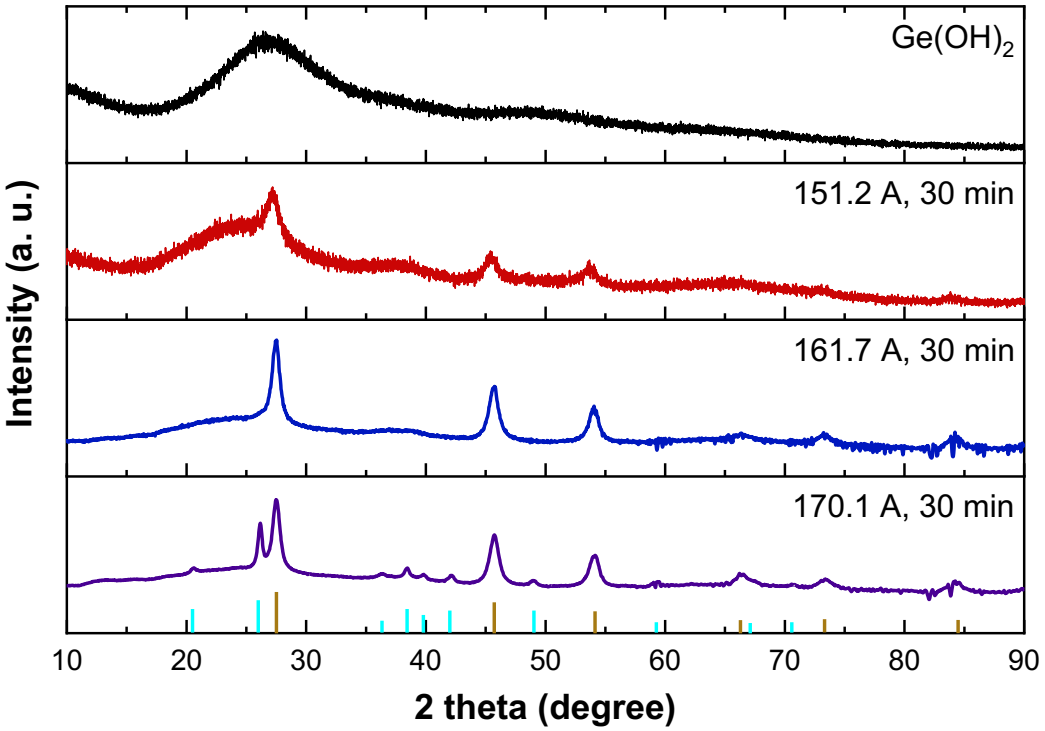

Figure 4.8. X-ray Diffraction of $Ge(OH)_2$ and GeNPs/GeO_x prepared at 151.2 A, 161.7 A, and 170.1 A for 30 min. The brown lines on the *x*-axis indicate reflections associated with diamond cubic Ge, PDF# 04-0545, while the blue lines indicate reflections associated with GeO_2, PDF# 85-1519.

After finding the optimal current required to synthesize the crystalline Ge, five cycles of inductive heat was performed on $Ge(OH)_2$ at 161.7 A with the condition illustrated in Figure 4.9a. Each cycle consists of 10 min of elevated current (161.7 A) and 5 min at no current (0 A) (10 min heating and 5 min cooling). The XRD of GeNPs/GeO_x composites show characteristic reflections of the crystalline Ge (Figure 4.9b).[204]

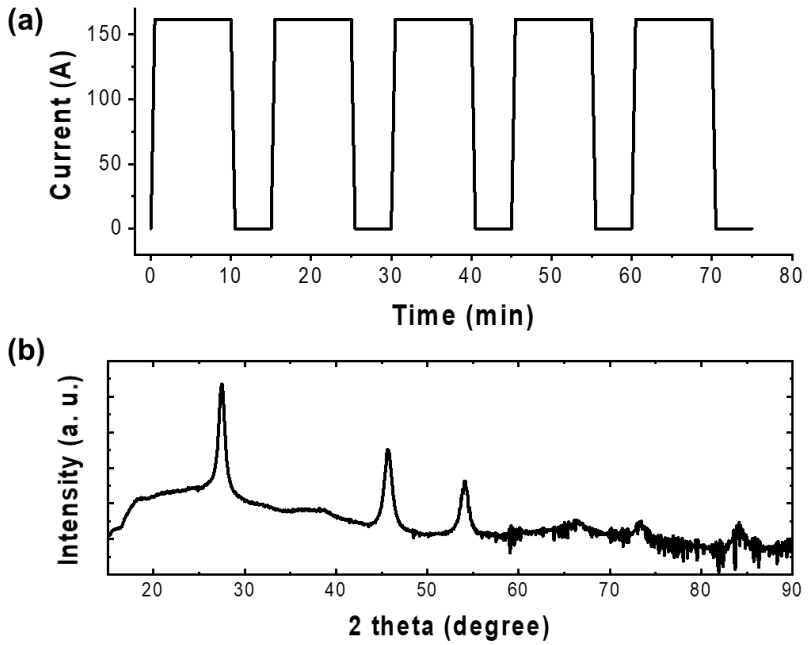

Figure 4.9. (a) Schematic drawing of cyclic heating of $Ge(OH)_2$ at 161.7 A. (b) X-ray Diffraction of GeNPs/GeO_x prepared by cycling heating at 161.7 A.

After that, the GeNPs/GeO_x were etched by ethanolic HF, and the liberated H-GeNPs were subjected to thermal hydrogermylation with 1-dodecene.[51] The dodecyl-GeNPs particles are shown in TEM and HRTEM images in Figure 4.10a-b. The particle sizes were 17.12 ± 3.95 nm. In general, the particles do not have a uniform shape, however, we observed facets. The average shifted histogram is shown in Figure 4.10c.[214]

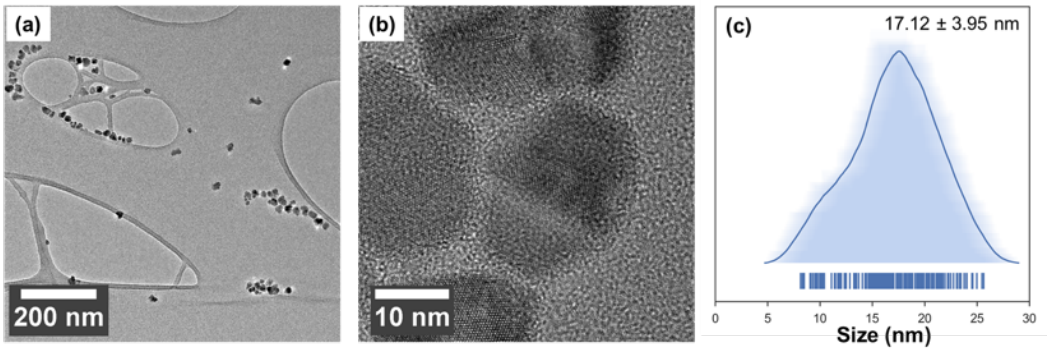

Figure 4.10. (a) Bright field TEM image, (b) high-resolution TEM image (d-spacing = 0.33 nm corresponds to the 111 plane of Ge), and (c) average shifted histogram of dodecyl-GeNPs prepared by five cycles of annealing at 161.7 A in an induction furnace.

4.3.2 GeNPs/GeO_x from Pre-annealed $Ge(OH)_2$

In a second strategy, the $Ge(OH)_2$ was pre-annealed at 400 °C using a Lindberg tube furnace for 1 h to obtain the GeNPs/GeO_x and then exposed to induction annealing at 151.2 A for five cycles and 161.7 A for five cycles (each cycle consists of 10 min heating and 5 min cooling) separately. Figure 4.11 shows diffraction patterns of the GeNPs/GeO_x annealed in a tube furnace and subsequent cyclic induction heating. The characteristic broad reflections of the crystalline GeNPs were observed after the heating of $Ge(OH)_2$ at 400 ºC. The reflections of GeNPs became sharp as they were subjected to inductive heating at 151.2 A for five cycles. Sharper reflections were observed as the current increased to 161.7 A, consistent with the growth of the Ge nanocrystals.

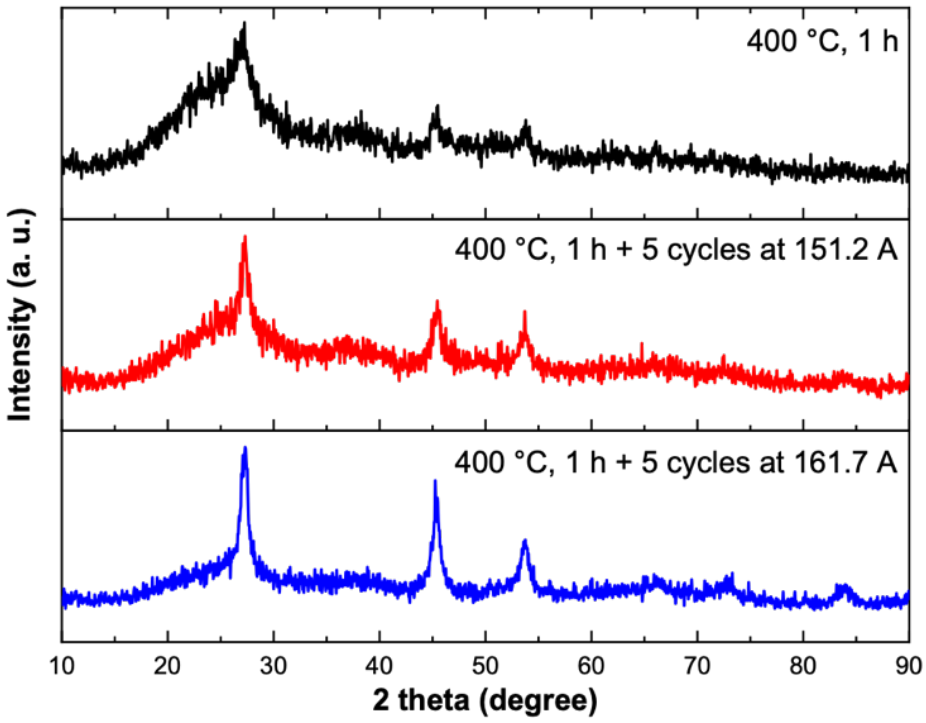

Figure 4.11. X-ray Diffraction of the GeNPs/GeO_x annealed at 400 ºC for 1 h in a tube furnace and subsequent cyclic induction heating at 151.2 A and 161.7 A.

The dodecyl-GeNPs obtained from the above GeNPs/GeO_x were analyzed by TEM and are shown in Figure 4.12. The particle size of the dodecyl-GeNPs prepared by heating in a tube furnace at 400 ºC is 6.07 ± 1.45 nm, while their size prepared by heating followed by five cycles of annealing at 151.2 A is 7.61 ± 1.94 nm. With five cycles of induction

heating at 161.7 A, 15.23 ± 4.00 nm sizes of GeNPs are seen, however, they are still random in shape. The average shifted histogram of particles obtained from conventional heating (Figure 4.12c) followed by cyclic induction heating (Figure 4.12f and 4.12i) indicates that the nanoparticles growth follows Ostwald ripening, in which smaller nanoparticles act as a seed to form larger nanoparticles.[266]

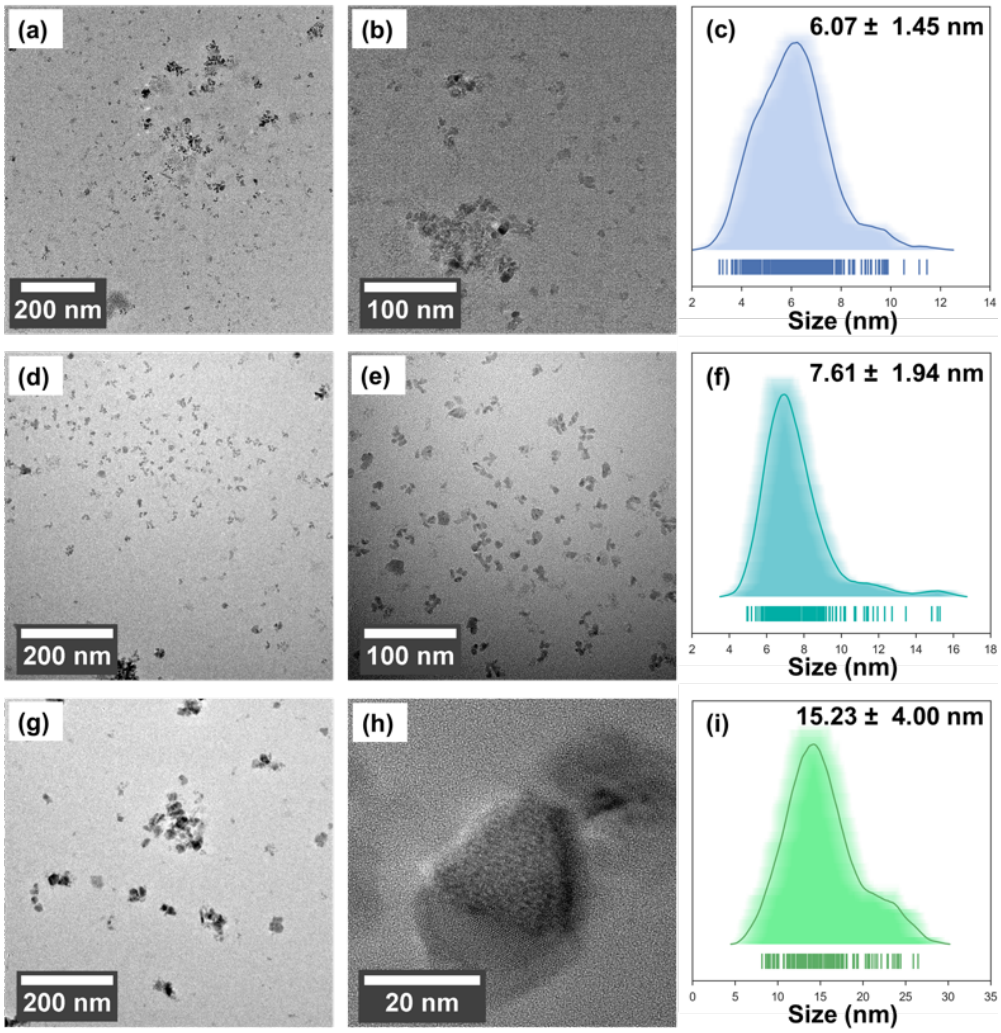

Figure 4.12. (a, b) Bright field TEM images, and (c) average shifted histogram of dodecyl-GeNPs prepared by Lindberg tube furnace at 400 ºC, 1 h, (d, e) Bright field TEM images, and (f) average shifted histogram of dodecyl-GeNPs prepared by Lindberg tube furnace at 400 ºC, 1 h, and 5 cycles of inductive heating at 151.2 A, and (g) Bright field TEM image, (h) high-resolution TEM image (d-spacing = 0.33 nm corresponds to 111 plane of Ge), and (f) average shifted histogram of dodecyl-GeNPs prepared by Lindberg tube furnace at 400 ºC, 1 h, and 5 cycles of inductive heating at 161.7 A.

The GeNPs/GeO_x was annealed at 161.7 A with 20-cycles of heating and cooling (10 min heating and 5 min cooling). The dodecyl-GeNPs obtained from that composite are shown in Figure 4.13. The particle sizes were 22.39 ± 3.96 nm. The particle shapes were mostly hexagonal; however, random shapes also were observed. The particles were aggregated, which might be due to the bigger size. Again, compared to the 5 cycles of induction heating, the 20 cycles of induction heating gives bigger particles, and the distribution of the particle sizes indicates Ostwald ripening.[266]

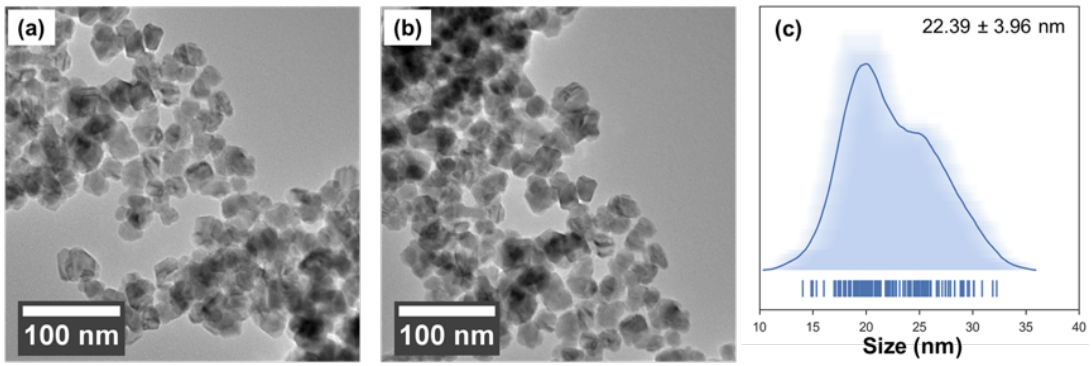

Figure 4.13. (a, b) Bright field TEM image, and (c) average shifted histogram of dodecyl-GeNPs prepared by Lindberg tube furnace at 400 ºC, 1 h, and 20 cycles of induction heating at 161.7 A in an induction furnace.

4.4 Conclusion

We have attempted to synthesize GeNPs of uniform shapes and sizes. It is clear that upon increased cyclic heating and cooling, the particles started to show facets. However, the particles also started to aggregate as the size increases. More experiments need to be done to determine the optimum conditions to obtain GeNPs with uniform size and shape. Specifically, the number of cycles and the time of heating and cooling needs to change. Size selective precipitation also should be done to separate the particles with uniform size.

Chapter 5

Summary and Future Directions

5.1 Summary

The thesis presented here is focused on the synthesis of germanium nanoparticles, their surface chemistry, and their application in polymer hybrid solar cells.

In Chapter 2, a series of experiments were carried out to obtain the optimum reaction conditions for dehydrocoupling between the hydride-terminated GeNPs and an alkylsilane. After determining the optimum conditions for reaction, three alkylsilanes (octadecylsilane, dimethyloctadecylsilane, and hydride-terminated polydimethylsiloxane) were used to passivate the surface hydride-terminated GeNPs via dehydrocoupling conditions. A hydrogermylation with 1-octadecene also was carried out to compare the reactivity with dehydrocoupling. During optimization of the reaction conditions, the reactivity, which was evaluated qualitatively by filtering the particles through a hydrophobic (0.45-μ PTFE) filter, was found to be better at higher temperatures and longer times. Alkyl/alkylsilane passivated GeNPs were analyzed by X-ray diffraction to obtain crystal information as well as to obtain the surface strain due to the presence of Ge–C or Ge–Si bonds on the surface. Alkylsilane passivated GeNPs showed higher crystal strain compared to alkyl passivated GeNPs. Again, tertiary alkylsilane passivated GeNPs (dimethyloctadecylsilane and H-PDMS) showed higher strain compared to primary alkylsilane passivated GeNPs (octadecylsilane).

In Chapter 3, the dodecyl-terminated GeNPs were used as a doping material in a PTB7-Th/IT-4F polymer solar cell. The polymer active layers were characterized by Grazing Incidence Small Angle X-ray Scattering (GISAXS) and Grazing Incidence Wide Angle X-ray Scattering (GIWAXS) to obtain information on the structure and morphology of the fabricated films. From GISAXS and GIWAXS, it is possible to obtain information about the preferred crystalline orientation of the polymer as well as the polymer grain size. However, the measurements need to be repeated because of instrument problems during measurements. The UV-vis absorption spectra show increased absorption due to the

addition of GeNPs (0.1–0.9 wt%) in the active layer. Inverted structured polymer solar cells were fabricated by blending 0, 0.3, 0.9 wt% of GeNPs in the active layers, and the performance of the devices were evaluated. The performance of solar cells incorporated with GeNPs was better than that of the polymer solar cells. However, incorporation 0.9% GeNPs showed inferior performance (1.36%) than 0.3% GeNPs (1.59%).

In Chapter 4, induction heating was used to synthesize GeNPs with uniform shapes and size distributions. The $Ge(OH)_2$ and GeNPs/GeO_x composites were annealed and cooled periodically for up to five cycles, but the particles did not display any preferred shapes apart from the size increase due to Ostwald ripening. At 20 cycles of periodic heating and cooling, hexagonal facets of GeNPs were observed in TEM, but the particles were aggregated. More experiments need to be done in order to obtain GeNPs with uniform shapes and sizes.

5.2 Future Directions

5.2.1 Investigation of the Amorphous and Crystalline GeNPs

In Chapter 2, dehydrocoupling was proven successful, but amorphous germanium content was seen, along with crystalline GeNPs. The source of amorphous content is unknown at this point, but there are two sources that they might come from. During heating of $Ge(OH)_2$ at 400 ºC to obtain GeNPs/GeO_x, it is possible to obtain a mixture of both amorphous and crystalline GeNPs. Raman spectroscopy can be used to obtain further information. For crystalline Ge, there is a Raman shift at 299 cm^{-1}, and for amorphous Ge, it shows a broad peak at 285 cm^{-1}. Again, a high temperature reaction may lead to amorphous particles. Kauzlarich and coworkers[37] reported a synthesis of crystalline butyl-GeNPs by reduction of $GeCl_4$ with Na(naphthalide). Upon heating at 300 ºC in vacuum, the particles became amorphous; these were later crystalized at 550 to 600 ºC. In the current method, dehydrocoupling reactions were carried out at 180 ºC for 96 h; this high temperature and long-time reaction might induce amorphousness in the nanoparticles. This can be confirmed by comparing the Raman data and TEM data for the product after 24 h and 96 h.

5.2.2 Optimization of the Active Layer of Solar Cell

In Chapter 3, dodecyl-GeNPs were used in polymer solar cells to improve their efficiency. The PCE was, in fact, improved from 1.13% to 1.59% by incorporating 0.3% GeNPs. However, the PCE with PTB7-Th donor and IT-4F acceptor should be 8 to 10% because similar solar cells made with PTB7-Th and ITIC showed ~8.0% efficiency.[267] Therefore, we need to repeat the experiment and optimize the thickness and processing conditions of the active layer. The electron extraction layer (MoO_3) also may be changed. To improve the solar cell further, dodecyl passivation can be replaced by a conductive surface ligand, such as phenyl acetylene or a conductive polymer. Hydride-terminated GeNPs also can be used for efficient charge transfer. Although using 0.9 wt% GeNPs showed a decrease in performance, more experiments should be carried out by using 1–5 wt% of GeNPs to see the trend in the performance of solar cells. In addition, different sizes of GeNPs can be applied to observe the effect of the size of nanoparticles on the efficiency of solar cells.

5.2.3 Follow Up Research on Induction Heating

In Chapter 4, induction heating was applied to synthesize a uniform shape and size distribution of GeNPs by periodic heating and cooling. Up to 20 cycles of periodic heating (10 min) and cooling (5 min) at 161.2 A showed hexagonal faceted GeNPs. More experiments need to be carried out by changing the number of cycles and the time of heating and cooling. Similar to Korgel and coworkers,[260] size selective precipitation also should be performed to isolate particles with different sizes and shapes.

5.2.4 GeNPs/P3HT Functional Hybrid Materials

GeNPs have potential uses in photodetectors, thin film transistors, and solar cells, among other optoelectronic applications. However, their utility is limited because the non-passivated surfaces usually are oxidized, rendering them non-conductive, and the passivated surfaces usually are made by non-conductive ligands. To explore their potential application, GeNPs need to be passivated by conducting or semiconducting surface groups. A mixture of GeNPs and P3HT polymer was applied into a photodetector by Wan and coworkers.[268] The authors obtained a significant increase in photocurrent in the hybrid device compared to GeNPs and P3HT alone, thus attained a superior photodetector. Veinot

and coworkers[269] synthesized P3HT functionalized silicon nanocrystals (SiNCs) by direct interfacial bonds on their surface. The authors achieved grafting of P3HT on to hydride-terminated silicon nanocrystals (SiNCs) by surface initiated Kumada catalyst transfer polycondensation. A similar reactivity can be achieved on the surface of GeNPs (Figure 5.1), allowing them to be used in photodetectors and thin film transistors.

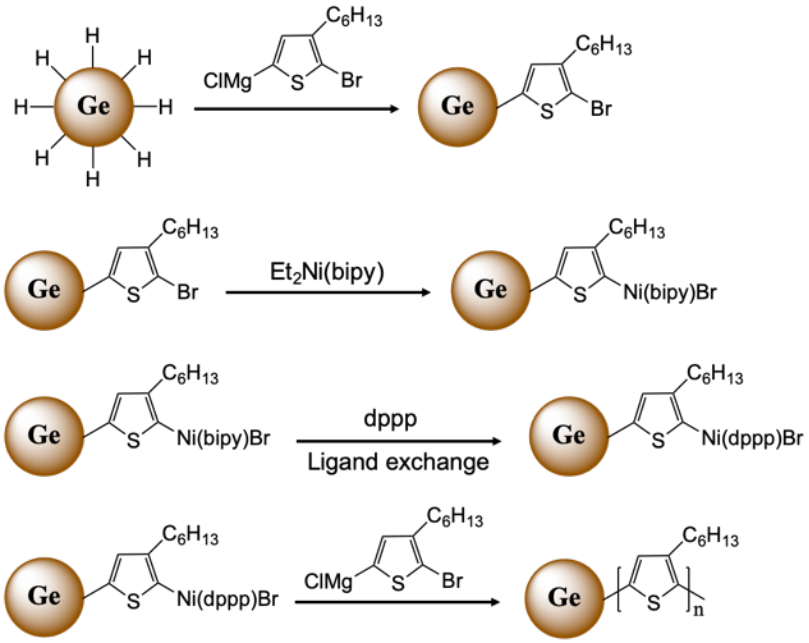

Figure 5.1. Schematic proposed synthesis of GeNPs-P3HT hybrid materials.

5.2.5 GeNPs for Lithium-ion Battery

GeNPs are very promising for lithium batteries (LIBs) because of their high theoretical capacity (1600 mAh/g), high volume expansion (370 %), good lithium diffusivity (400 times higher than silicon), and high electrical conductivity (104 times higher than silicon).[270] However, during lithiation/delithiation processes, GeNPs can aggregate and merge into micron-sized particles. This process leads to structural fracturing and pulverization that destroy the connections between the conductive matrix and the germanium. To overcome this issue, several approaches have been explored, including the mixing of GeNPs with carbon-based materials,[97] In addition, germanium-polymer composites have shown high capacities as anode materials,[270] however, these types of materials have not been studied widely. Fortunately, we can draw inspiration from

analogous investigations of silicon nanocrystals where Chen et al.[271] synthesized a core-shell silicon/polyaniline nanocomposite that showed impressive device metrices. The polyaniline served as a matrix that simultaneously improved the electrical contact between the binders and electrode materials and prevented silicon nanoparticles from degrading upon expansion during lithiation/delithiation processes. In another report, Aghajamali et al.[272] synthesized 10-undecenoic acid functionalized SiNCs and introduced them into a graphene aerogel. The resulting SiNCs-graphene aerogel composite was used as the anode material in LIBs, and they obtained a stable specific capacity of ~1100 mAh/g over 500 cycles, with 90% capacity retention. Based on the similarity between silicon and germanium chemistry, it is possible to apply GeNPs-polyaniline and GeNPs-graphene aerogel composites as the anode materials of LIBs.

BIBLIOGRAPHY

(1) EEA. European Commission of Recommendation on the Definition of Nanomaterial. *Off. J. Eur. Union* **2011**, *L275* (June 2010), 38–40. https://doi.org/10.2777/13162.

(2) Lichtfouse, E.; Schwarzbauer, J.; Robert, D. *Environmental Chemistry for a Sustainable World*; Springer Netherlands, 2012; Vol. 2. https://doi.org/10.1007/978-94-007-2439-6.

(3) Rossetti, R.; Nakahara, S.; Brus, L. E. Quantum Size Effects in the Redox Potentials, Resonance Raman Spectra, and Electronic Spectra of CdS Crystallites in Aqueous Solution. *J. Chem. Phys.* **1983**, *79* (2), 1086–1088. https://doi.org/10.1063/1.445834.

(4) Dasog, M.; De los Reyes, G. B.; Titova, L. V.; Hegmann, F. A.; Veinot, J. G. C. Size *vs* Surface: Tuning the Photoluminescence of Freestanding Silicon Nanocrystals Across the Visible Spectrum *via* Surface Groups. *ACS Nano* **2014**, *8* (9), 9636–9648. https://doi.org/10.1021/nn504109a.

(5) Ashoori, R. C. Electrons in Artificial Atoms. *Nature* **1996**, *379* (6564), 413–419. https://doi.org/10.1038/379413a0.

(6) Kastner, M. A. Artificial Atoms. *Phys. Today* **1993**, *46* (1), 24–31. https://doi.org/10.1063/1.881393.

(7) Quantum Confinement Effects in Semiconductors. In *Applied Nanophotonics*; Demir, H. V., Gaponenko, S. V, Eds.; Cambridge University Press: Cambridge, 2018; pp 52–91. https://doi.org/10.1017/9781316535868.004.

(8) Algar, W. R.; Susumu, K.; Delehanty, J. B.; Medintz, I. L. Semiconductor Quantum Dots in Bioanalysis: Crossing the Valley of Death. *Anal. Chem.* **2011**, *83* (23), 8826–8837. https://doi.org/10.1021/ac201331r.

(9) Kagan, C. R.; Murray, C. B.; Nirmal, M.; Bawendi, M. G. Electronic Energy Transfer in CdSe Quantum Dot Solids. *Phys. Rev. Lett.* **1996**, *76* (9), 1517–1520. https://doi.org/10.1103/PhysRevLett.76.1517.

(10) Li, H.; Shih, W. Y.; Shih*, W.-H. Synthesis and Characterization of Aqueous Carboxyl-Capped CdS Quantum Dots for Bioapplications. **2007**. https://doi.org/10.1021/IE060963S.

(11) Pietryga, J. M.; Schaller, R. D.; Werder, D.; Stewart, M. H.; Klimov, V. I.; Hollingsworth, J. A. Pushing the Band Gap Envelope: Mid-Infrared Emitting Colloidal PbSe Quantum Dots. *J. Am. Chem. Soc.* **2004**, *126* (38), 11752–11753. https://doi.org/10.1021/ja047659f.

(12) Moreels, I.; Justo, Y.; De Geyter, B.; Haustraete, K.; Martins, J. C.; Hens, Z. Size-Tunable, Bright, and Stable PbS Quantum Dots: A Surface Chemistry Study. *ACS Nano* **2011**, *5* (3), 2004–2012. https://doi.org/10.1021/nn103050w.

(13) Micic, O. I.; Curtis, C. J.; Jones, K. M.; Sprague, J. R.; Nozik, A. J. Synthesis and Characterization of InP Quantum Dots. *J. Phys. Chem.* **1994**, *98* (19), 4966–4969. https://doi.org/10.1021/j100070a004.

(14) Guzelian, A. A.; Banin, U.; Kadavanich, A. V.; Peng, X.; Alivisatos, A. P. Colloidal Chemical Synthesis and Characterization of InAs Nanocrystal Quantum Dots. *Appl. Phys. Lett.* **1996**, *69* (10), 1432–1434. https://doi.org/10.1063/1.117605.

(15) Guo, Y.; Zhang, L.; Cao, F.; Mang, L.; Lei, X.; Cheng, S.; Song, J. Hydrothermal Synthesis of Blue-Emitting Silicon Quantum Dots for Fluorescent Detection of Hypochlorite in Tap Water. *Anal. Methods* **2016**, *8* (13), 2723–2728. https://doi.org/10.1039/C5AY03325J.

(16) Karatutlu, A.; Song, M.; Wheeler, A. P.; Ersoy, O.; Little, W. R.; Zhang, Y.; Puech, P.; Boi, F. S.; Luklinska, Z.; Sapelkin, A. V. Synthesis and Structure of Free-Standing Germanium Quantum Dots and Their Application in Live Cell Imaging. *RSC Adv.* **2015**, *5* (26), 20566–20573. https://doi.org/10.1039/c5ra01529d.

(17) Dai, X.; Deng, Y.; Peng, X.; Jin, Y. Quantum-Dot Light-Emitting Diodes for Large-Area Displays: Towards the Dawn of Commercialization. *Adv. Mater.* **2017**, *29* (14), 1607022. https://doi.org/10.1002/adma.201607022.

(18) Namdari, P.; Negahdari, B.; Eatemadi, A. Synthesis, Properties and Biomedical Applications of Carbon-Based Quantum Dots: An Updated Review. *Biomed. Pharmacother.* **2017**, *87*, 209–222. https://doi.org/10.1016/J.BIOPHA.2016.12.108.

(19) Liu, Z.; Yuan, J.; Hawks, S. A.; Shi, G.; Lee, S.-T.; Ma, W. Photovoltaic Devices Based on Colloidal PbX Quantum Dots: Progress and Prospects. *Sol. RRL* **2017**, *1* (5), 1600021. https://doi.org/10.1002/solr.201600021.

(20) García de Arquer, F. P.; Armin, A.; Meredith, P.; Sargent, E. H. Solution-Processed Semiconductors for next-Generation Photodetectors. *Nat. Rev. Mater.* **2017**, *2* (3), 16100. https://doi.org/10.1038/natrevmats.2016.100.

(21) Zhang, Z.; Zheng, T.; Li, X.; Xu, J.; Zeng, H. Progress of Carbon Quantum Dots in Photocatalysis Applications. *Part. Part. Syst. Charact.* **2016**, *33* (8), 457–472. https://doi.org/10.1002/ppsc.201500243.

(22) McVey, B. F. P.; Prabakar, S.; Gooding, J. J.; Tilley, R. D. Solution Synthesis, Surface Passivation, Optical Properties, Biomedical Applications, and Cytotoxicity of Silicon and Germanium Nanocrystals. *Chempluschem* **2017**, *82* (1), 60–73. https://doi.org/10.1002/cplu.201600207.

(23) Nekoueian, K.; Amiri, M.; Sillanpää, M.; Marken, F.; Boukherroub, R.; Szunerits, S. Carbon-Based Quantum Particles: An Electroanalytical and Biomedical Perspective. *Chem. Soc. Rev.* **2019**, *48* (15), 4281–4316. https://doi.org/10.1039/C8CS00445E.

(24) Chang, H.; Sun, S.-Q. Silicon Nanoparticles: Preparation, Properties, and Applications. *Chinese Phys. B* **2014**, *23* (8), 088102. https://doi.org/10.1088/1674-1056/23/8/088102.

(25) Vaughn II, D. D.; Schaak, R. E. Synthesis, Properties and Applications of Colloidal Germanium and Germanium-Based Nanomaterials. *Chem. Soc. Rev.* **2013**, *42* (7), 2861–2879. https://doi.org/10.1039/C2CS35364D.

(26) Dag, Om.; Kuperman, A.; Ozin, G. A. Germanium Nanoclusters: Chemical Vapor Deposition of Digermane in Zeolite Y and Mordenite. *Adv. Mater.* **1994**, *6* (2), 147–150. https://doi.org/10.1002/adma.19940060211.

(27) Kamins, T. I.; Ohlberg, D. A. A.; Williams, R. S.; Zhang, W.; Chou, S. Y. Positioning of Self-

Assembled, Single-Crystal, Germanium Islands by Silicon Nanoimprinting. *Appl. Phys. Lett.* **1999**, *74* (12), 1773–1775. https://doi.org/10.1063/1.123683.

(28) Kartopu, G.; Sapelkin, A. V.; Karavanskii, V. A.; Serincan, U.; Turan, R. Structural and Optical Properties of Porous Nanocrystalline Ge. *J. Appl. Phys.* **2008**, *103* (11), 113518. https://doi.org/10.1063/1.2924417.

(29) Gresback, R.; Holman, Z.; Kortshagen, U. Nonthermal Plasma Synthesis of Size-Controlled, Monodisperse, Freestanding Germanium Nanocrystals. *Appl. Phys. Lett.* **2007**. https://doi.org/10.1063/1.2778356.

(30) Holman, Z. C.; Kortshagen, U. R. Solution-Processed Germanium Nanocrystal Thin Films as Materials for Low-Cost Optical and Electronic Devices. *Langmuir* **2009**, *25* (19), 11883–11889. https://doi.org/10.1021/la9015228.

(31) Stoldt, C. R.; Haag, M. A.; Larsen, B. A. Preparation of Freestanding Germanium Nanocrystals by Ultrasonic Aerosol Pyrolysis. *Appl. Phys. Lett.* **2008**, *93* (4), 043125. https://doi.org/10.1063/1.2965471.

(32) Ngiam, S.; Jensen, K. F.; Kolenbrander, K. D. Synthesis of Ge Nanocrystals Embedded in a Si Host Matrix. *J. Appl. Phys.* **1994**, *76* (12), 8201–8203. https://doi.org/10.1063/1.357878.

(33) Gao, F.; Green, M. A.; Conibeer, G.; Cho, E.-C.; Huang, Y.; Pere-Wurfl, I.; Flynn, C. Fabrication of Multilayered Ge Nanocrystals by Magnetron Sputtering and Annealing. *Nanotechnology* **2008**, *19* (45), 455611. https://doi.org/10.1088/0957-4484/19/45/455611.

(34) Tsuji, H.; Arai, N.; Gotoh, N.; Minotani, T.; Ishibashi, T.; Okumine, T.; Adachi, K.; Kotaki, H.; Gotoh, Y.; Ishikawa, J. Germanium Nanoparticle Formation in Thin Oxide Films on Si by Negative-Ion Implantation. *Surf. Coatings Technol.* **2007**, *201* (19–20), 8516–8520. https://doi.org/10.1016/J.SURFCOAT.2006.02.063.

(35) Kornowski, A.; Giersig, M.; Vogel, R.; Chemseddine, A.; Weller, H. Nanometer-Sized Colloidal Germanium Particles: Wet-Chemical Synthesis, Laser-Induced Crystallization and Particle Growth. *Adv. Mater.* **1993**, *5* (9), 634–636. https://doi.org/10.1002/adma.19930050907.

(36) Lee, H.; Kim, M. G.; Choi, C. H.; Sun, Y.-K.; Yoon, C. S.; Cho, J. Surface-Stabilized Amorphous Germanium Nanoparticles for Lithium-Storage Material. *J. Phys. Chem. B* **2005**, *109* (44), 20719–20723. https://doi.org/10.1021/jp052620y.

(37) Chiu, H. W.; Chervin, C. N.; Kauzlarich, S. M. Phase Changes in Ge Nanoparticles. *Chem. Mater.* **2005**, *17* (19), 4858–4864. https://doi.org/10.1021/cm050674e.

(38) Chiu, H. W.; Kauzlarich, S. M. Investigation of Reaction Conditions for Optimal Germanium Nanoparticle Production by a Simple Reduction Route. *Chem. Mater.* **2006**, *18* (4), 1023–1028. https://doi.org/10.1021/cm0521222.

(39) Wu, H. P.; Liu, J. F.; Wang, Y. W.; Zeng, Y. W.; Jiang, J. Z. Preparation of Ge Nanocrystals via Ultrasonic Solution Reduction. *Mater. Lett.* **2006**, *60* (7), 986–989. https://doi.org/10.1016/J.MATLET.2005.10.063.

(40) Prabakar, S.; Shiohara, A.; Hanada, S.; Fujioka, K.; Yamamoto, K.; Tilley, R. D. Size Controlled Synthesis of Germanium Nanocrystals by Hydride Reducing Agents and Their Biological Applications. *Chem. Mater.* **2010**, *22* (2), 482–486. https://doi.org/10.1021/cm9030599.

(41) Carolan, D.; Doyle, H. Size and Emission Color Tuning in the Solution Phase Synthesis of Highly Luminescent Germanium Nanocrystals. *J. Mater. Chem. C* **2014**, *2* (18), 3562–3568. https://doi.org/10.1039/C4TC00319E.

(42) Vaughn, D. D.; Bondi, J. F.; Schaak, R. E. Colloidal Synthesis of Air-Stable Crystalline Germanium Nanoparticles with Tunable Sizes and Shapes. *Chem. Mater.* **2010**, *22* (22), 6103–6108. https://doi.org/10.1021/cm1015965.

(43) Codoluto, S. C.; Baumgardner, W. J.; Hanrath, T. Fundamental Aspects of Nucleation and Growth in the Solution-Phase Synthesis of Germanium Nanocrystals. *CrystEngComm* **2010**, *12* (10), 2903. https://doi.org/10.1039/c002820g.

(44) Ruddy, D. A.; Johnson, J. C.; Smith, E. R.; Neale, N. R. Size and Bandgap Control in the Solution-Phase Synthesis of Near-Infrared-Emitting Germanium Nanocrystals. *ACS Nano* **2010**, *4* (12), 7459–7466. https://doi.org/10.1021/nn102728u.

(45) Muthuswamy, E.; Iskandar, A. S.; Amador, M. M.; Kauzlarich, S. M. Facile Synthesis of Germanium Nanoparticles with Size Control: Microwave versus Conventional Heating. *Chem. Mater.* **2013**, *25* (8), 1416–1422. https://doi.org/10.1021/cm302229b.

(46) Pescara, B.; Mazzio, K. A.; Lips, K.; Raoux, S. Crystallinity and Size Control of Colloidal Germanium Nanoparticles from Organogermanium Halide Reagents. *Inorg. Chem.* **2019**, *58* (8), 4802–4811. https://doi.org/10.1021/acs.inorgchem.8b03157.

(47) Henderson, E. J.; Hessel, C. M.; Veinot, J. G. C. Synthesis and Photoluminescent Properties of Size-Controlled Germanium Nanocrystals from Phenyl Trichlorogermane-Derived Polymers. *J. Am. Chem. Soc.* **2008**, *130* (11), 3624–3632. https://doi.org/10.1021/ja710286a.

(48) Dag, Ö.; Henderson, E. J.; Ozin, G. A. Synthesis of Nanoamorphous Germanium and Its Transformation to Nanocrystalline Germanium. *Small* **2012**, *8* (6), 921–929. https://doi.org/10.1002/smll.201101993.

(49) Gerung, H.; Bunge, S. D.; Boyle, T. J.; Brinker, C. J.; Han, S. M. Anhydrous Solution Synthesis of Germanium Nanocrystals from the Germanium(Ii) Precursor Ge[N(SiMe3)2]2. *Chem. Commun.* **2005**, No. 14, 1914–1916. https://doi.org/10.1039/b416066e.

(50) Boyle, T. J.; Tribby, L. J.; Ottley, L. A. M.; Han, S. M. Synthesis and Characterization of Germanium Coordination Compounds for Production of Germanium Nanomaterials. *Eur. J. Inorg. Chem.* **2009**, No. 36, 5550–5560. https://doi.org/10.1002/ejic.200900556.

(51) Javadi, M.; Picard, D.; Sinelnikov, R.; Narreto, M. A.; Hegmann, F. A.; Veinot, J. G. C. Synthesis and Surface Functionalization of Hydride-Terminated Ge Nanocrystals Obtained from the Thermal Treatment of Ge(OH)2. *Langmuir* **2017**, *33* (35), 8757–8765. https://doi.org/10.1021/acs.langmuir.7b00358.

(52) Gerion, D.; Zaitseva, N.; Saw, C.; Casula, M. F.; Fakra, S.; Van Buuren, T.; Galli, G. Solution Synthesis of Germanium Nanocrystals: Success and Open Challenges. *Nano Lett.* **2004**, *4* (4), 597–602. https://doi.org/10.1021/nl035231t.

(53) Zaitseva, N.; Dai, Z. R.; Grant, C. D.; Harper, J.; Saw, C. Germanium Nanocrystals Synthesized in High-Boiling-Point Organic Solvents. *Chem. Mater.* **2007**, *19* (21), 5174–5178. https://doi.org/10.1021/cm070062p.

(54) Purkait, T. K.; Swarnakar, A. K.; De Los Reyes, G. B.; Hegmann, F. A.; Rivard, E.; Veinot, J. G. C. One-Pot Synthesis of Functionalized Germanium Nanocrystals from a Single Source Precursor. *Nanoscale* **2015**, *7* (6), 2241–2244. https://doi.org/10.1039/C4NR05125D.

(55) Lu, X.; Ziegler, K. J.; Ghezelbash, A.; Johnston, K. P.; Korgel, B. A. Synthesis of Germanium Nanocrystals in High Temperature Supercritical Fluid Solvents. *Nano Lett.* **2004**, *4* (5), 969–974. https://doi.org/10.1021/nl049831j.

(56) Taylor, B. R.; Kauzlarich, S. M.; Lee, H. W. H.; Delgado, G. R. Solution Synthesis of Germanium Nanocrystals Demonstrating Quantum Confinement. *Chem. Mater.* **1998**, *10* (1), 22–24. https://doi.org/10.1021/cm970576w.

(57) Ma, X.; Wu, F.; Kauzlarich, S. M. Alkyl-Terminated Crystalline Ge Nanoparticles Prepared from NaGe: Synthesis, Functionalization and Optical Properties. *J. Solid State Chem.* **2008**, *181* (7), 1628–1633. https://doi.org/10.1016/J.JSSC.2008.06.018.

(58) Taylor, B. R.; Kauzlarich, S. M.; Delgado, G. R.; Lee, H. W. H. Solution Synthesis and Characterization of Quantum Confined Ge Nanoparticles. *Chem. Mater.* **1999**, *11* (9), 2493–2500. https://doi.org/10.1021/cm990203q.

(59) Tanke, R. S.; Kauzlarich, S. M.; Patten, T. E.; Pettigrew, K. A.; Murphy, D. L.; Thompson, M. E.; Lee, H. W. H. Synthesis of Germanium Nanoclusters with Irreversibly Attached Functional Groups: Acetals, Alcohols, Esters, and Polymers. *Chem. Mater.* **2003**, *15* (8), 1682–1689. https://doi.org/10.1021/cm021778h.

(60) Pugsley, A. J.; Bull, C. L.; Sella, A.; Sankar, G.; McMillan, P. F. XAS/EXAFS Studies of Ge Nanoparticles Produced by Reaction between Mg2Ge and GeCl4. *J. Solid State Chem.* **2011**, *184* (9), 2345–2352. https://doi.org/10.1016/J.JSSC.2011.06.020.

(61) Liu, X.; Lin, N.; Cai, W.; Zhao, Y.; Zhou, J.; Liang, J.; Zhu, Y.; Qian, Y. Mesoporous Germanium Nanoparticles Synthesized in Molten Zinc Chloride at Low Temperature as a High-Performance Anode for Lithium-Ion Batteries. *Dalt. Trans.* **2018**, *47* (22), 7402–7406. https://doi.org/10.1039/c8dt01060a.

(62) Carolan, D. Recent Advances in Germanium Nanocrystals: Synthesis, Optical Properties and Applications. *Prog. Mater. Sci.* **2017**, *90*, 128–158. https://doi.org/10.1016/j.pmatsci.2017.07.005.

(63) Fok, E.; Shih, M.; Meldrum, A.; Veinot, J. G. C. Preparation of Alkyl-Surface Functionalized Germanium Quantum Dots via Thermally Initiated Hydrogermylation. *Chem. Commun.* **2004**, *0* (4), 386. https://doi.org/10.1039/b314887d.

(64) Warner, J. H.; Tilley, R. D. Synthesis of Water-Soluble Photoluminescent Germanium Nanocrystals. *Nanotechnology* **2006**, *17* (15), 3745–3749. https://doi.org/10.1088/0957-4484/17/15/022.

(65) Carolan, D.; Doyle, H. Tuning the Photoluminescence of Germanium Nanocrystals through Surface Bound Functional Groups. *Part. Part. Syst. Charact.* **2017**, *34* (2), 1600303. https://doi.org/10.1002/ppsc.201600303.

(66) McVey, B. F. P.; O'Mara, P. B.; McGrath, A. J.; Faramus, A.; Yasarapudi, V. B.; Gonçales, V. R.; Tan, V. T. G.; Schmidt, T. W.; Gooding, J. J.; Tilley, R. D. Role of Surface Capping Molecule Polarity on the Optical Properties of Solution Synthesized Germanium Nanocrystals. *Langmuir* **2017**, *33* (35), 8790–8798. https://doi.org/10.1021/acs.langmuir.7b01028.

(67) Vasudevan, D.; Gaddam, R. R.; Trinchi, A.; Cole, I. Core–Shell Quantum Dots: Properties and Applications. *J. Alloys Compd.* **2015**, *636*, 395–404. https://doi.org/10.1016/J.JALLCOM.2015.02.102.

(68) Guo, Y.; Rowland, C. E.; Schaller, R. D.; Vela, J. Near-Infrared Photoluminescence Enhancement in Ge/CdS and Ge/ZnS Core/Shell Nanocrystals: Utilizing IV/II–VI Semiconductor Epitaxy. *ACS Nano* **2014**, *8* (8), 8334–8343. https://doi.org/10.1021/nn502792m.

(69) Hunter, K. I.; Held, J. T.; Mkhoyan, K. A.; Kortshagen, U. R. Nonthermal Plasma Synthesis of Core/Shell Quantum Dots: Strained Ge/Si Nanocrystals. *ACS Appl. Mater. Interfaces* **2017**, *9* (9), 8263–8270. https://doi.org/10.1021/acsami.6b16170.

(70) Maeda, Y.; Tsukamoto, N.; Yazawa, Y.; Kanemitsu, Y.; Masumoto, Y. Visible Photoluminescence of Ge Microcrystals Embedded in SiO_2 Glassy Matrices. *Appl. Phys. Lett.* **1991**, *59* (24), 3168–3170. https://doi.org/10.1063/1.105773.

(71) Millo, O.; Balberg, I.; Azulay, D.; Purkait, T. K.; Swarnakar, A. K.; Rivard, E.; Veinot, J. G. C. Direct Evaluation of the Quantum Confinement Effect in Single Isolated Ge Nanocrystals. *J. Phys. Chem. Lett.* **2015**, *6* (17), 3396–3402. https://doi.org/10.1021/acs.jpclett.5b01541.

(72) Lee, D. C.; Pietryga, J. M.; Robel, I.; Werder, D. J.; Schaller, R. D.; Klimov, V. I. Colloidal Synthesis of Infrared-Emitting Germanium Nanocrystals. *J. Am. Chem. Soc.* **2009**, *131* (10), 3436–3437. https://doi.org/10.1021/ja809218s.

(73) Wheeler, L. M.; Levij, L. M.; Kortshagen, U. R. Tunable Band Gap Emission and Surface Passivation of Germanium Nanocrystals Synthesized in the Gas Phase. *J. Phys. Chem. Lett.* **2013**, *4* (20), 3392–3396. https://doi.org/10.1021/jz401576b.

(74) Little, W.; Karatutlu, A.; Bolmatov, D.; Trachenko, K.; Sapelkin, A. V.; Cibin, G.; Taylor, R.; Mosselmans, F.; Dent, A. J.; Mountjoy, G. Structural Origin of Light Emission in Germanium Quantum Dots. *Sci. Rep.* **2015**, *4* (1), 7372. https://doi.org/10.1038/srep07372.

(75) Holman, Z. C.; Liu, C.-Y.; Kortshagen, U. R. Germanium and Silicon Nanocrystal Thin-Film Field-Effect Transistors from Solution. *Nano Lett.* **2010**, *10* (7), 2661–2666. https://doi.org/10.1021/nl101413d.

(76) Liu, X.; Ji, X.; Liu, M.; Liu, N.; Tao, Z.; Dai, Q.; Wei, L.; Li, C.; Zhang, X.; Wang, B. High-

Performance Ge Quantum Dot Decorated Graphene/Zinc-Oxide Heterostructure Infrared Photodetector. *ACS Appl. Mater. Interfaces* **2015**, *7* (4), 2452–2458. https://doi.org/10.1021/am5072173.

(77) Seino, M.; Henderson, E. J.; Puzzo, D. P.; Kadota, N.; Ozin, G. A. Germanium Nanocrystal Doped Inverse Crystalline Silicon Opal. *J. Mater. Chem.* **2011**, *21* (40), 15895. https://doi.org/10.1039/c1jm13172a.

(78) Meric, Z.; Mehringer, C.; Karpstein, N.; Jank, M. P. M.; Peukert, W.; Frey, L. Tunable Conduction Type of Solution-Processed Germanium Nanoparticle Based Field Effect Transistors and Their Inverter Integration. *Phys. Chem. Chem. Phys.* **2015**, *17* (34), 22106–22114. https://doi.org/10.1039/C5CP03321G.

(79) Gao, Y.; Pi, X.; Wang, X.; Yuan, T.; Jiang, Q.; Gresback, R.; Lu, J.; Yang, D. Structures, Oxidation, and Charge Transport of Phosphorus-Doped Germanium Nanocrystals. *Part. Part. Syst. Charact.* **2016**, *33* (5), 271–278. https://doi.org/10.1002/ppsc.201600016.

(80) Wheeler, L. M.; Nichols, A. W.; Chernomordik, B. D.; Anderson, N. C.; Beard, M. C.; Neale, N. R. All-Inorganic Germanium Nanocrystal Films by Cationic Ligand Exchange. *Nano Lett.* **2016**, *16* (3), 1949–1954. https://doi.org/10.1021/acs.nanolett.5b05192.

(81) Sun, B.; Zou, G.; Shen, X.; Zhang, X. Exciton Dissociation and Photovoltaic Effect in Germanium Nanocrystals and Poly(3-Hexylthiophene) Composites. *Appl. Phys. Lett.* **2009**, *94* (23), 233504. https://doi.org/10.1063/1.3152997.

(82) Manthiram, A. Materials Challenges and Opportunities of Lithium Ion Batteries. *J. Phys. Chem. Lett.* **2011**, *2* (3), 176–184. https://doi.org/10.1021/jz1015422.

(83) Dunn, B.; Kamath, H.; Tarascon, J.-M. Electrical Energy Storage for the Grid: A Battery of Choices. *Science (80-.).* **2011**, *334* (6058), 928–935. https://doi.org/10.1126/SCIENCE.1212741.

(84) Li, X.; Liang, J.; Hou, Z.; Zhu, Y.; Wang, Y.; Qian, Y. A Synchronous Approach for Facile Production of Ge–Carbon Hybrid Nanoparticles for High-Performance Lithium Batteries. *Chem. Commun.* **2015**, *51* (18), 3882–3885. https://doi.org/10.1039/C5CC00080G.

(85) Cheng, J.; Du, J. Facile Synthesis of Germanium–Graphene Nanocomposites and Their Application as Anode Materials for Lithium Ion Batteries. *CrystEngComm* **2012**, *14* (2), 397–400. https://doi.org/10.1039/C1CE06251D.

(86) Zhong, X.; Wang, J.; Li, W.; Liu, X.; Yang, Z.; Gu, L.; Yu*, Y. Facile Synthesis of Germanium–Reduced Graphene Oxide Composite as Anode for High Performance Lithium-Ion Batteries. *RSC Adv.* **2014**, *4* (102), 58184–58189. https://doi.org/10.1039/C4RA08797F.

(87) Qin, J.; Wang, X.; Cao, M.; Hu, C. Germanium Quantum Dots Embedded in N-Doping Graphene Matrix with Sponge-Like Architecture for Enhanced Performance in Lithium-Ion Batteries. *Chem. - A Eur. J.* **2014**, *20* (31), 9675–9682. https://doi.org/10.1002/chem.201402151.

(88) Xiao, Y.; Cao, M. High-Performance Lithium Storage Achieved by Chemically Binding Germanium Nanoparticles with N-Doped Carbon. *ACS Appl. Mater. Interfaces* **2014**, *6* (15), 12922–12930.

https://doi.org/10.1021/am502867f.

(89) Ren, J.-G.; Wu, Q.-H.; Tang, H.; Hong, G.; Zhang, W.; Lee, S.-T. Germanium–Graphene Composite Anode for High-Energy Lithium Batteries with Long Cycle Life. *J. Mater. Chem. A* **2013**, *1* (5), 1821–1826. https://doi.org/10.1039/C2TA01286C.

(90) Li, W.; Yang, Z.; Cheng, J.; Zhong, X.; Gu, L.; Yu, Y. Germanium Nanoparticles Encapsulated in Flexible Carbon Nanofibers as Self-Supported Electrodes for High Performance Lithium-Ion Batteries. *Nanoscale* **2014**, *6* (9), 4532–4537. https://doi.org/10.1039/C4NR00140K.

(91) Park, M.-H.; Kim, K.; Kim, J.; Cho, J. Flexible Dimensional Control of High-Capacity Li-Ion-Battery Anodes: From 0D Hollow to 3D Porous Germanium Nanoparticle Assemblies. *Adv. Mater.* **2010**, *22* (3), 415–418. https://doi.org/10.1002/adma.200901846.

(92) Xue, D.-J.; Xin, S.; Yan, Y.; Jiang, K.-C.; Yin, Y.-X.; Guo, Y.-G.; Wan, L.-J. Improving the Electrode Performance of Ge through Ge@C Core–Shell Nanoparticles and Graphene Networks. *J. Am. Chem. Soc.* **2012**, *134* (5), 2512–2515. https://doi.org/10.1021/ja211266m.

(93) Ngo, D. T.; Kalubarme, R. S.; Le, H. T. T.; Fisher, J. G.; Park, C.-N.; Kim, I.-D.; Park, C.-J. Carbon-Interconnected Ge Nanocrystals as an Anode with Ultra-Long-Term Cyclability for Lithium Ion Batteries. *Adv. Funct. Mater.* **2014**, *24* (33), 5291–5298. https://doi.org/10.1002/adfm.201400888.

(94) Liu, M.; Ma, X.; Gan, L.; Xu, Z.; Zhu, D.; Chen, L. A Facile Synthesis of a Novel Mesoporous Ge@C Sphere Anode with Stable and High Capacity for Lithium Ion Batteries. *J. Mater. Chem. A* **2014**, *2* (40), 17107–17114. https://doi.org/10.1039/C4TA02888K.

(95) Cui, G.; Gu, L.; Zhi, L.; Kaskhedikar, N.; Van Aken, P. A.; Müllen, K.; Maier, J.; M??llen, K.; Maier, J. A Germanium-Carbon Nanocomposite Material for Lithium Batteries. *Adv. Mater.* **2008**, *20* (16), 3079–3083. https://doi.org/10.1002/adma.200800586.

(96) Cui, G.; Gu, L.; Kaskhedikar, N.; van Aken, P. A.; Maier, J. A Novel Germanium/Carbon Nanotubes Nanocomposite for Lithium Storage Material. *Electrochim. Acta* **2010**, *55* (3), 985–988. https://doi.org/10.1016/J.ELECTACTA.2009.08.056.

(97) Jo, G.; Choi, I.; Ahn, H.; Park, M. J. Binder-Free Ge Nanoparticles-Carbon Hybrids for Anode Materials of Advanced Lithium Batteries with High Capacity and Rate Capability. *Chem. Commun.* **2012**, *48* (33), 3987–3989. https://doi.org/10.1039/C2CC30294B.

(98) Liu, J.; Song, K.; Zhu, C.; Chen, C.-C.; van Aken, P. A.; Maier, J.; Yu, Y. Ge/C Nanowires as High-Capacity and Long-Life Anode Materials for Li-Ion Batteries. *ACS Nano* **2014**, *8* (7), 7051–7059. https://doi.org/10.1021/nn501945f.

(99) Jin, S.; Li, N.; Cui, H.; Wang, C. Embedded into Graphene Ge Nanoparticles Highly Dispersed on Vertically Aligned Graphene with Excellent Electrochemical Performance for Lithium Storage. *ACS Appl. Mater. Interfaces* **2014**, *6* (21), 19397–19404. https://doi.org/10.1021/am505499x.

(100) Zhong, C.; Wang, J.-Z.; Gao, X.-W.; Wexler, D.; Liu, H.-K. In Situ One-Step Synthesis of a 3D Nanostructured Germanium–Graphene Composite and Its Application in Lithium-Ion Batteries. *J. Mater. Chem. A* **2013**, *1* (36), 10798. https://doi.org/10.1039/c3ta11796k.

(101) Yuan, F.-W.; Tuan, H.-Y. Scalable Solution-Grown High-Germanium-Nanoparticle-Loading Graphene Nanocomposites as High-Performance Lithium-Ion Battery Electrodes: An Example of a Graphene-Based Platform toward Practical Full-Cell Applications. *Chem. Mater.* **2014**, *26* (6), 2172–2179. https://doi.org/10.1021/cm5002016.

(102) Fan, J.; Chu, P. K. Group IV Nanoparticles: Synthesis, Properties, and Biological Applications. *Small* **2010**, *6* (19), 2080–2098. https://doi.org/10.1002/smll.201000543.

(103) Lambert, T. N.; Andrews, N. L.; Gerung, H.; Boyle, T. J.; Oliver, J. M.; Wilson, B. S.; Han, S. M. Water-Soluble Germanium(0) Nanocrystals: Cell Recognition and Near-Infrared Photothermal Conversion Properties. *Small* **2007**, *3* (4), 691–699. https://doi.org/10.1002/smll.200600529.

(104) Carolan, D.; Doyle, H. Germanium Nanocrystals as Luminescent Probes for Rapid, Sensitive and Label-Free Detection of Fe^{3+} Ions. *Nanoscale* **2015**, *7* (12), 5488–5494. https://doi.org/10.1039/C4NR07470J.

(105) Tiwari, S.; Tiwari, T.; Carter, S. A.; Scott, J. C.; Yakhmi, J. V. Advances in Polymer-Based Photovoltaic Cells: Review of Pioneering Materials, Design, and Device Physics. In *Handbook of Ecomaterials*; Springer International Publishing: Cham, 2018; pp 1–48. https://doi.org/10.1007/978-3-319-48281-1_59-1.

(106) Jacobson, M. Z.; Delucchi, M. A.; Bauer, Z. A. F.; Goodman, S. C.; Chapman, W. E.; Cameron, M. A.; Bozonnat, C.; Chobadi, L.; Clonts, H. A.; Enevoldsen, P.; et al. 100% Clean and Renewable Wind, Water, and Sunlight All-Sector Energy Roadmaps for 139 Countries of the World. *Joule* **2017**, *1* (1), 108–121. https://doi.org/10.1016/J.JOULE.2017.07.005.

(107) Hagfeldt, A.; Boschloo, G.; Sun, L.; Kloo, L.; Pettersson, H. Dye-Sensitized Solar Cells. *Chem. Rev.* **2010**, *110* (11), 6595–6663. https://doi.org/10.1021/cr900356p.

(108) Khatibi, A.; Razi Astaraei, F.; Ahmadi, M. H. Generation and Combination of the Solar Cells: A Current Model Review. *Energy Sci. Eng.* **2019**, *7* (2), 305–322. https://doi.org/10.1002/ese3.292.

(109) Gong, J.; Liang, J.; Sumathy, K. Review on Dye-Sensitized Solar Cells (DSSCs): Fundamental Concepts and Novel Materials. *Renew. Sustain. Energy Rev.* **2012**, *16* (8), 5848–5860. https://doi.org/10.1016/J.RSER.2012.04.044.

(110) Abdulrazzaq, O. A.; Saini, V.; Bourdo, S.; Dervishi, E.; Biris, A. S. Organic Solar Cells: A Review of Materials, Limitations, and Possibilities for Improvement. *Part. Sci. Technol.* **2013**, *31* (5), 427–442. https://doi.org/10.1080/02726351.2013.769470.

(111) Niu, G.; Guo, X.; Wang, L. Review of Recent Progress in Chemical Stability of Perovskite Solar Cells. *J. Mater. Chem. A* **2015**, *3* (17), 8970–8980. https://doi.org/10.1039/C4TA04994B.

(112) Jun, H. K.; Careem, M. A.; Arof, A. K. Quantum Dot-Sensitized Solar Cells—Perspective and Recent Developments: A Review of Cd Chalcogenide Quantum Dots as Sensitizers. *Renew. Sustain. Energy Rev.* **2013**, *22*, 148–167. https://doi.org/10.1016/J.RSER.2013.01.030.

(113) Best Research-Cell Efficiency Chart | Photovoltaic Research | NREL https://www.nrel.gov/pv/cell-efficiency.html (accessed Oct 1, 2019).

(114) Yoo, J. J.; Wieghold, S.; Sponseller, M. C.; Chua, M. R.; Bertram, S. N.; Hartono, N. T. P.; Tresback, J. S.; Hansen, E. C.; Correa-Baena, J.-P.; Bulović, V.; et al. An Interface Stabilized Perovskite Solar Cell with High Stabilized Efficiency and Low Voltage Loss. *Energy Environ. Sci.* **2019**, *12* (7), 2192–2199. https://doi.org/10.1039/C9EE00751B.

(115) Fan, B.; Zhang, D.; Li, M.; Zhong, W.; Zeng, Z.; Ying, L.; Huang, F.; Cao, Y. Achieving over 16% Efficiency for Single-Junction Organic Solar Cells. *Sci. China Chem.* **2019**, *62* (6), 746–752. https://doi.org/10.1007/s11426-019-9457-5.

(116) Bisquert, J. *The Physics of Solar Cells : Perovskites, Organics, and Photovoltaic Fundamentals*.

(117) Pelzer, K. M.; Darling, S. B. Charge Generation in Organic Photovoltaics: A Review of Theory and Computation. *Mol. Syst. Des. Eng.* **2016**, *1* (1), 10–24. https://doi.org/10.1039/C6ME00005C.

(118) Brabec, C.; Scherf, U.; Dyakonov, V. *Organic Photovoltaics : Materials, Device Physics, and Manufacturing Technologies.*; Wiley, 2014.

(119) Hedley, G. J.; Ruseckas, A.; Samuel, I. D. W. Light Harvesting for Organic Photovoltaics. *Chem. Rev.* **2017**, *117* (2), 796–837. https://doi.org/10.1021/acs.chemrev.6b00215.

(120) Peumans, P.; Yakimov, A.; Forrest, S. R. Small Molecular Weight Organic Thin-Film Photodetectors and Solar Cells. *J. Appl. Phys.* **2003**, *93* (7), 3693–3723. https://doi.org/10.1063/1.1534621.

(121) Tessler, N.; Preezant, Y.; Rappaport, N.; Roichman, Y. Charge Transport in Disordered Organic Materials and Its Relevance to Thin-Film Devices: A Tutorial Review. *Adv. Mater.* **2009**, *21* (27), 2741–2761. https://doi.org/10.1002/adma.200803541.

(122) de Castro, F. A.; Heier, J.; Nüesch, F.; Hany, R. Origin of the Kink in Current-Density Versus Voltage Curves and Efficiency Enhancement of Polymer-C $_{\bf 60}$ Heterojunction Solar Cells. *IEEE J. Sel. Top. Quantum Electron.* **2010**, *16* (6), 1690–1699. https://doi.org/10.1109/JSTQE.2010.2040807.

(123) Nüesch, F.; Rotzinger, F.; Si-Ahmed, L.; Zuppiroli, L. Chemical Potential Shifts at Organic Device Electrodes Induced by Grafted Monolayers. *Chem. Phys. Lett.* **1998**, *288* (5–6), 861–867. https://doi.org/10.1016/S0009-2614(98)00350-9.

(124) Kemerink, M.; Kramer, J. M.; Gommans, H. H. P.; Janssen, R. A. J. Temperature-Dependent Built-in Potential in Organic Semiconductor Devices. *Appl. Phys. Lett.* **2006**, *88* (19), 192108. https://doi.org/10.1063/1.2205007.

(125) Lee, T.-W.; Park, O. O. The Effect of Different Heat Treatments on the Luminescence Efficiency of Polymer Light-Emitting Diodes. *Adv. Mater.* **2000**, *12* (11), 801–804. https://doi.org/10.1002/(SICI)1521-4095(200006)12:11<801::AID-ADMA801>3.0.CO;2-G.

(126) Photovoltaic Effect in Single-Layer Organic Solar Cell Devices Fabricated with Two New Imidazolin-5-One Molecules. *Sol. Energy Mater. Sol. Cells* **2008**, *92* (9), 1043–1046. https://doi.org/10.1016/J.SOLMAT.2008.02.039.

(127) Eftaiha, A. F.; Sun, J.-P.; Hill, I. G.; Welch, G. C. Recent Advances of Non-Fullerene, Small Molecular Acceptors for Solution Processed Bulk Heterojunction Solar Cells. *J. Mater. Chem. A*

2014, *2* (5), 1201–1213. https://doi.org/10.1039/C3TA14236A.

(128) Li, G.; Shrotriya, V.; Huang, J.; Yao, Y.; Moriarty, T.; Emery, K.; Yang, Y. High-Efficiency Solution Processable Polymer Photovoltaic Cells by Self-Organization of Polymer Blends. *Nat. Mater.* **2005**, *4* (11), 864–868. https://doi.org/10.1038/nmat1500.

(129) Huang, Y.; Kramer, E. J.; Heeger, A. J.; Bazan, G. C. Bulk Heterojunction Solar Cells: Morphology and Performance Relationships. *Chem. Rev.* **2014**, *114* (14), 7006–7043. https://doi.org/10.1021/cr400353v.

(130) Rafique, S.; Abdullah, S. M.; Sulaiman, K.; Iwamoto, M. Fundamentals of Bulk Heterojunction Organic Solar Cells: An Overview of Stability/Degradation Issues and Strategies for Improvement. *Renew. Sustain. Energy Rev.* **2018**, *84*, 43–53. https://doi.org/10.1016/J.RSER.2017.12.008.

(131) Wang, K.; Ren, H.; Yi, C.; Liu, C.; Wang, H.; Huang, L.; Zhang, H.; Karim, A.; Gong, X. Solution-Processed Fe 3 O 4 Magnetic Nanoparticle Thin Film Aligned by an External Magnetostatic Field as a Hole Extraction Layer for Polymer Solar Cells. *ACS Appl. Mater. Interfaces* **2013**, *5* (20), 10325–10330. https://doi.org/10.1021/am4033179.

(132) Yu, G.; Gao, J.; Hummelen, J. C.; Wudl, F.; Heeger, A. J. Polymer Photovoltaic Cells: Enhanced Efficiencies via a Network of Internal Donor-Acceptor Heterojunctions. *Science (80-.).* **1995**, *270* (5243), 1789 LP – 1791. https://doi.org/10.1126/science.270.5243.1789.

(133) Wong, K. W.; Yip, H. L.; Luo, Y.; Wong, K. Y.; Lau, W. M.; Low, K. H.; Chow, H. F.; Gao, Z. Q.; Yeung, W. L.; Chang, C. C. Blocking Reactions between Indium-Tin Oxide and Poly (3,4-Ethylene Dioxythiophene):Poly(Styrene Sulphonate) with a Self-Assembly Monolayer. *Appl. Phys. Lett.* **2002**, *80* (15), 2788–2790. https://doi.org/10.1063/1.1469220.

(134) de Jong, M. P.; van IJzendoorn, L. J.; de Voigt, M. J. A. Stability of the Interface between Indium-Tin-Oxide and Poly(3,4-Ethylenedioxythiophene)/Poly(Styrenesulfonate) in Polymer Light-Emitting Diodes. *Appl. Phys. Lett.* **2000**, *77* (14), 2255–2257. https://doi.org/10.1063/1.1315344.

(135) Wang, K.; Liu, C.; Meng, T.; Yi, C.; Gong, X. Inverted Organic Photovoltaic Cells. *Chem. Soc. Rev.* **2016**, *45* (10), 2937–2975. https://doi.org/10.1039/C5CS00831J.

(136) Lloyd, M. T.; Peters, C. H.; Garcia, A.; Kauvar, I. V.; Berry, J. J.; Reese, M. O.; McGehee, M. D.; Ginley, D. S.; Olson, D. C. Influence of the Hole-Transport Layer on the Initial Behavior and Lifetime of Inverted Organic Photovoltaics. *Sol. Energy Mater. Sol. Cells* **2011**, *95* (5), 1382–1388. https://doi.org/10.1016/J.SOLMAT.2010.12.036.

(137) Lloyd, M. T.; Olson, D. C.; Lu, P.; Fang, E.; Moore, D. L.; White, M. S.; Reese, M. O.; Ginley, D. S.; Hsu, J. W. P. Impact of Contact Evolution on the Shelf Life of Organic Solar Cells. *J. Mater. Chem.* **2009**, *19* (41), 7638–7642. https://doi.org/10.1039/b910213b.

(138) Krebs, F. C. Air Stable Polymer Photovoltaics Based on a Process Free from Vacuum Steps and Fullerenes. *Sol. Energy Mater. Sol. Cells* **2008**, *92* (7), 715–726. https://doi.org/10.1016/J.SOLMAT.2008.01.013.

(139) Bian, L.; Zhu, E.; Tang, J.; Tang, W.; Zhang, F. Recent Progress in the Design of Narrow Bandgap

Conjugated Polymers for High-Efficiency Organic Solar Cells. *Prog. Polym. Sci.* **2012**, *37* (9), 1292–1331. https://doi.org/10.1016/J.PROGPOLYMSCI.2012.03.001.

(140) Tang, C. W. Two-layer Organic Photovoltaic Cell. *Appl. Phys. Lett.* **1986**, *48* (2), 183–185. https://doi.org/10.1063/1.96937.

(141) Kim, J. Y.; Kim, S. H.; Lee, H.-H.; Lee, K.; Ma, W.; Gong, X.; Heeger, A. J. New Architecture for High-Efficiency Polymer Photovoltaic Cells Using Solution-Based Titanium Oxide as an Optical Spacer. *Adv. Mater.* **2006**, *18* (5), 572–576. https://doi.org/10.1002/adma.200501825.

(142) Wang, W.; Song, L.; Magerl, D.; Moseguí González, D.; Körstgens, V.; Philipp, M.; Moulin, J.-F.; Müller-Buschbaum, P. Influence of Solvent Additive 1,8-Octanedithiol on P3HT:PCBM Solar Cells. *Adv. Funct. Mater.* **2018**, *28* (20), 1800209. https://doi.org/10.1002/adfm.201800209.

(143) Duan, C.; Huang, F.; Cao, Y. Recent Development of Push–Pull Conjugated Polymers for Bulk-Heterojunction Photovoltaics: Rational Design and Fine Tailoring of Molecular Structures. *J. Mater. Chem.* **2012**, *22* (21), 10416. https://doi.org/10.1039/c2jm30470h.

(144) Zhang, Y.; Bovill, E.; Kingsley, J.; Buckley, A. R.; Yi, H.; Iraqi, A.; Wang, T.; Lidzey, D. G. PCDTBT Based Solar Cells: One Year of Operation under Real-World Conditions. *Sci. Rep.* **2016**, *6* (1), 21632. https://doi.org/10.1038/srep21632.

(145) Mateker, W. R.; Douglas, J. D.; Cabanetos, C.; Sachs-Quintana, I. T.; Bartelt, J. A.; Hoke, E. T.; El Labban, A.; Beaujuge, P. M.; Fréchet, J. M. J.; McGehee, M. D. Improving the Long-Term Stability of PBDTTPD Polymer Solar Cells through Material Purification Aimed at Removing Organic Impurities. *Energy Environ. Sci.* **2013**, *6* (8), 2529. https://doi.org/10.1039/c3ee41328d.

(146) Zheng, Y.; Wang, G.; Huang, D.; Kong, J.; Goh, T.; Huang, W.; Yu, J.; Taylor, A. D. Binary Solvent Additives Treatment Boosts the Efficiency of PTB7:PCBM Polymer Solar Cells to Over 9.5%. *Sol. RRL* **2018**, *2* (4), 1700144. https://doi.org/10.1002/solr.201700144.

(147) S. Gurney, R.; Li, W.; Yan, Y.; Liu, D.; J. Pearson, A.; Wang, T. Morphology and Efficiency Enhancements of PTB7-Th:ITIC Nonfullerene Organic Solar Cells Processed via Solvent Vapor Annealing. *J. Energy Chem.* **2019**, *37*, 148–156. https://doi.org/10.1016/J.JECHEM.2018.12.015.

(148) Wan, Q.; Guo, X.; Wang, Z.; Li, W.; Guo, B.; Ma, W.; Zhang, M.; Li, Y. 10.8% Efficiency Polymer Solar Cells Based on PTB7-Th and PC 71 BM via Binary Solvent Additives Treatment. *Adv. Funct. Mater.* **2016**. https://doi.org/10.1002/adfm.201602181.

(149) Wadsworth, A.; Moser, M.; Marks, A.; Little, M. S.; Gasparini, N.; Brabec, C. J.; Baran, D.; McCulloch, I. Critical Review of the Molecular Design Progress in Non-Fullerene Electron Acceptors towards Commercially Viable Organic Solar Cells. *Chem. Soc. Rev.* **2019**, *48* (6), 1596–1625. https://doi.org/10.1039/C7CS00892A.

(150) Zhang, G.; Zhao, J.; Chow, P. C. Y.; Jiang, K.; Zhang, J.; Zhu, Z.; Zhang, J.; Huang, F.; Yan, H. Nonfullerene Acceptor Molecules for Bulk Heterojunction Organic Solar Cells. *Chem. Rev.* **2018**, *118* (7), 3447–3507. https://doi.org/10.1021/acs.chemrev.7b00535.

(151) Yang, Y.; Zhang, Z.-G.; Bin, H.; Chen, S.; Gao, L.; Xue, L.; Yang, C.; Li, Y. Side-Chain

Isomerization on an n-Type Organic Semiconductor ITIC Acceptor Makes 11.77% High Efficiency Polymer Solar Cells. *J. Am. Chem. Soc.* **2016**, *138* (45), 15011–15018. https://doi.org/10.1021/jacs.6b09110.

(152) Liu, F.; Zhang, J.; Wang, Y.; Chen, S.; Zhou, Z.; Yang, C.; Gao, F.; Zhu, X. Modulating Structure Ordering via Side-Chain Engineering of Thieno[3,4- *b*]Thiophene-Based Electron Acceptors for Efficient Organic Solar Cells with Reduced Energy Losses. *ACS Appl. Mater. Interfaces* **2019**, *11* (38), 35193–35200. https://doi.org/10.1021/acsami.9b10641.

(153) Yao, H.; Cui, Y.; Yu, R.; Gao, B.; Zhang, H.; Hou, J. Design, Synthesis, and Photovoltaic Characterization of a Small Molecular Acceptor with an Ultra-Narrow Band Gap. *Angew. Chemie Int. Ed.* **2017**, *56* (11), 3045–3049. https://doi.org/10.1002/anie.201610944.

(154) Li, S.; Ye, L.; Zhao, W.; Zhang, S.; Mukherjee, S.; Ade, H.; Hou, J. Energy-Level Modulation of Small-Molecule Electron Acceptors to Achieve over 12% Efficiency in Polymer Solar Cells. *Adv. Mater.* **2016**, *28* (42), 9423–9429. https://doi.org/10.1002/adma.201602776.

(155) Dai, S.; Zhao, F.; Zhang, Q.; Lau, T.-K.; Li, T.; Liu, K.; Ling, Q.; Wang, C.; Lu, X.; You, W.; et al. Fused Nonacyclic Electron Acceptors for Efficient Polymer Solar Cells. *J. Am. Chem. Soc.* **2017**, *139* (3), 1336–1343. https://doi.org/10.1021/jacs.6b12755.

(156) Zhao, F.; Dai, S.; Wu, Y.; Zhang, Q.; Wang, J.; Jiang, L.; Ling, Q.; Wei, Z.; Ma, W.; You, W.; et al. Single-Junction Binary-Blend Nonfullerene Polymer Solar Cells with 12.1% Efficiency. *Adv. Mater.* **2017**, *29* (18), 1700144. https://doi.org/10.1002/adma.201700144.

(157) Zhao, W.; Li, S.; Yao, H.; Zhang, S.; Zhang, Y.; Yang, B.; Hou, J. Molecular Optimization Enables over 13% Efficiency in Organic Solar Cells. *J. Am. Chem. Soc.* **2017**, *139* (21), 7148–7151. https://doi.org/10.1021/jacs.7b02677.

(158) Chueh, C.-C.; Li, C.-Z.; Jen, A. K.-Y. Recent Progress and Perspective in Solution-Processed Interfacial Materials for Efficient and Stable Polymer and Organometal Perovskite Solar Cells. *Energy Environ. Sci.* **2015**, *8* (4), 1160–1189. https://doi.org/10.1039/C4EE03824J.

(159) Yip, H.-L.; Jen, A. K.-Y. Recent Advances in Solution-Processed Interfacial Materials for Efficient and Stable Polymer Solar Cells. *Energy Environ. Sci.* **2012**, *5* (3), 5994. https://doi.org/10.1039/c2ee02806a.

(160) Lan, W.; Liu, Y.; Wu, B.; Xu, B.; Pu, H.; Wei, B.; Peng, Y.; Tian, W.; Zhu, F. Effect of ZnO Electron Extraction Layer on Charge Recombination and Collection Properties in Organic Solar Cells. *ACS Appl. Energy Mater.* **2019**, acsaem.9b01383. https://doi.org/10.1021/acsaem.9b01383.

(161) Sun, Y.; Seo, J. H.; Takacs, C. J.; Seifter, J.; Heeger, A. J. Inverted Polymer Solar Cells Integrated with a Low-Temperature-Annealed Sol-Gel-Derived ZnO Film as an Electron Transport Layer. *Adv. Mater.* **2011**, *23* (14), 1679–1683. https://doi.org/10.1002/adma.201004301.

(162) White, M. S.; Olson, D. C.; Shaheen, S. E.; Kopidakis, N.; Ginley, D. S. Inverted Bulk-Heterojunction Organic Photovoltaic Device Using a Solution-Derived ZnO Underlayer. *Appl. Phys. Lett.* **2006**, *89* (14), 143517. https://doi.org/10.1063/1.2359579.

(163) Jagadamma, L. K.; Abdelsamie, M.; El Labban, A.; Aresu, E.; Ngongang Ndjawa, G. O.; Anjum, D. H.; Cha, D.; Beaujuge, P. M.; Amassian, A. Efficient Inverted Bulk-Heterojunction Solar Cells from Low-Temperature Processing of Amorphous ZnO Buffer Layers. *J. Mater. Chem. A* **2014**, *2* (33), 13321. https://doi.org/10.1039/C4TA02276A.

(164) Thambidurai, M.; Kim, J. Y.; Ko, Y.; Song, H.; Shin, H.; Song, J.; Lee, Y.; Muthukumarasamy, N.; Velauthapillai, D.; Lee, C. High-Efficiency Inverted Organic Solar Cells with Polyethylene Oxide-Modified Zn-Doped TiO $_2$ as an Interfacial Electron Transport Layer. *Nanoscale* **2014**, *6* (15), 8585. https://doi.org/10.1039/C4NR02780A.

(165) Chen, F.; Chen, Q.; Mao, L.; Wang, Y.; Huang, X.; Lu, W.; Wang, B.; Chen, L. Tuning Indium Tin Oxide Work Function with Solution-Processed Alkali Carbonate Interfacial Layers for High-Efficiency Inverted Organic Photovoltaic Cells. *Nanotechnology* **2013**, *24* (48), 484011. https://doi.org/10.1088/0957-4484/24/48/484011.

(166) Park, B.; Shin, J. C.; Cho, C. Y. Water-Processable Electron-Collecting Layers of a Hybrid Poly(Ethylene Oxide): Caesium Carbonate Composite for Flexible Inverted Polymer Solar Cells. *Sol. Energy Mater. Sol. Cells* **2013**, *108*, 1–8. https://doi.org/10.1016/J.SOLMAT.2012.09.006.

(167) Hu, X.; Chen, L.; Chen, Y. Universal and Versatile MoO $_3$ -Based Hole Transport Layers for Efficient and Stable Polymer Solar Cells. *J. Phys. Chem. C* **2014**, *118* (19), 9930–9938. https://doi.org/10.1021/jp501995t.

(168) Dang, Y.; Wang, Y.; Shen, S.; Huang, S.; Qu, X.; Pang, Y.; Silva, S. R. P.; Kang, B.; Lu, G. Solution Processed Hybrid Graphene-MoO3 Hole Transport Layers for Improved Performance of Organic Solar Cells. *Org. Electron.* **2019**, *67*, 95–100. https://doi.org/10.1016/J.ORGEL.2019.01.013.

(169) Cheng, F.; Wu, Y.; Shen, Y.; Cai, X.; Li, L. Enhancing the Performance and Stability of Organic Solar Cells Using Solution Processed MoO $_3$ as Hole Transport Layer. *RSC Adv.* **2017**, *7* (60), 37952–37958. https://doi.org/10.1039/C7RA06511F.

(170) Shim, J. W.; Fuentes-Hernandez, C.; Dindar, A.; Zhou, Y.; Khan, T. M.; Kippelen, B. Polymer Solar Cells with NiO Hole-Collecting Interlayers Processed by Atomic Layer Deposition. *Org. Electron.* **2013**, *14* (11), 2802–2808. https://doi.org/10.1016/J.ORGEL.2013.07.028.

(171) Steirer, K. X.; Ndione, P. F.; Widjonarko, N. E.; Lloyd, M. T.; Meyer, J.; Ratcliff, E. L.; Kahn, A.; Armstrong, N. R.; Curtis, C. J.; Ginley, D. S.; et al. Enhanced Efficiency in Plastic Solar Cells via Energy Matched Solution Processed NiOx Interlayers. *Adv. Energy Mater.* **2011**, *1* (5), 813–820. https://doi.org/10.1002/aenm.201100234.

(172) Chen, C.-P.; Chen, Y.-D.; Chuang, S.-C. High-Performance and Highly Durable Inverted Organic Photovoltaics Embedding Solution-Processable Vanadium Oxides as an Interfacial Hole-Transporting Layer. *Adv. Mater.* **2011**, *23* (33), n/a-n/a. https://doi.org/10.1002/adma.201102142.

(173) Lu, L.; Xu, T.; Jung, I. H.; Yu, L. Match the Interfacial Energy Levels between Hole Transport Layer and Donor Polymer To Achieve High Solar Cell Performance. *J. Phys. Chem. C* **2014**, *118* (40), 22834–22839. https://doi.org/10.1021/jp5036663.

(174) Li, S.-S.; Tu, K.-H.; Lin, C.-C.; Chen, C.-W.; Chhowalla, M. Solution-Processable Graphene Oxide as an Efficient Hole Transport Layer in Polymer Solar Cells. *ACS Nano* **2010**, *4* (6), 3169–3174. https://doi.org/10.1021/nn100551j.

(175) Fan, Z.; Zhang, H.; Yu, W.; Xing, Z.; Wei, H.; Dong, Q.; Tian, W.; Yang, B. Aqueous-Solution-Processed Hybrid Solar Cells from Poly(1,4-Naphthalenevinylene) and CdTe Nanocrystals. *ACS Appl. Mater. Interfaces* **2011**, *3* (8), 2919–2923. https://doi.org/10.1021/am200616j.

(176) Ren, S.; Chang, L. Y.; Lim, S. K.; Zhao, J.; Smith, M.; Zhao, N.; Bulović, V.; Bawendi, M.; Gradečak, S. Inorganic-Organic Hybrid Solar Cell: Bridging Quantum Dots to Conjugated Polymer Nanowires. *Nano Lett.* **2011**. https://doi.org/10.1021/nl202435t.

(177) Lek, J. Y.; Xi, L.; Kardynal, B. E.; Wong, L. H.; Lam, Y. M. Understanding the Effect of Surface Chemistry on Charge Generation and Transport in Poly (3-Hexylthiophene)/CdSe Hybrid Solar Cells. *ACS Appl. Mater. Interfaces* **2011**, *3* (2), 287–292. https://doi.org/10.1021/am100938f.

(178) Oosterhout, S. D.; Wienk, M. M.; van Bavel, S. S.; Thiedmann, R.; Jan Anton Koster, L.; Gilot, J.; Loos, J.; Schmidt, V.; Janssen, R. A. J. The Effect of Three-Dimensional Morphology on the Efficiency of Hybrid Polymer Solar Cells. *Nat. Mater.* **2009**, *8* (10), 818–824. https://doi.org/10.1038/nmat2533.

(179) Lee, J.; Jho, J. Y. Fabrication of Highly Ordered and Vertically Oriented TiO2 Nanotube Arrays for Ordered Heterojunction Polymer/Inorganic Hybrid Solar Cell. *Sol. Energy Mater. Sol. Cells* **2011**, *95* (11), 3152–3156. https://doi.org/10.1016/J.SOLMAT.2011.06.046.

(180) Günes, S.; Fritz, K. P.; Neugebauer, H.; Sariciftci, N. S.; Kumar, S.; Scholes, G. D. Hybrid Solar Cells Using PbS Nanoparticles. *Sol. Energy Mater. Sol. Cells* **2007**, *91* (5), 420–423. https://doi.org/10.1016/j.solmat.2006.10.016.

(181) Sun, Y.; Liu, Z.; Yuan, J.; Chen, J.; Zhou, Y.; Huang, X.; Ma, W. Polymer Selection toward Efficient Polymer/PbSe Planar Heterojunction Hybrid Solar Cells. *Org. Electron.* **2015**, *24*, 263–271. https://doi.org/10.1016/J.ORGEL.2015.06.010.

(182) Kudo, N.; Shimazaki, Y.; Ohkita, H.; Ohoka, M.; Ito, S. Organic–Inorganic Hybrid Solar Cells Based on Conducting Polymer and SnO2 Nanoparticles Chemically Modified with a Fullerene Derivative. *Sol. Energy Mater. Sol. Cells* **2007**, *91* (13), 1243–1247. https://doi.org/10.1016/J.SOLMAT.2006.11.019.

(183) Liu, C.-Y.; Holman, Z. C.; Kortshagen, U. R. Hybrid Solar Cells from P3HT and Silicon Nanocrystals. *Nano Lett.* **2009**, *9* (1), 449–452. https://doi.org/10.1021/nl8034338.

(184) Preparation and Characterization of P3HT:CuInSe2:TiO2 Thin Film for Hybrid Solar Cell Applications. *Thin Solid Films* **2011**, *520* (5), 1503–1510. https://doi.org/10.1016/J.TSF.2011.08.001.

(185) Liu, C.-Y.; Kortshagen, U. R. Hybrid Solar Cells from MDMO-PPV and Silicon Nanocrystals. *Nanoscale* **2012**, *4* (13), 3963–3968. https://doi.org/10.1039/C2NR30436H.

(186) Zhao, S.; Pi, X.; Mercier, C.; Yuan, Z.; Sun, B.; Yang, D. Silicon-Nanocrystal-Incorporated Ternary

Hybrid Solar Cells. *Nano Energy* **2016**, *26*, 305–312. https://doi.org/10.1016/j.nanoen.2016.05.040.

(187) Wanninayake, A. P.; Gunashekar, S.; Li, S.; Church, B. C.; Abu-Zahra, N. Performance Enhancement of Polymer Solar Cells Using Copper Oxide Nanoparticles. *Semicond. Sci. Technol.* **2015**, *30* (6), 064004. https://doi.org/10.1088/0268-1242/30/6/064004.

(188) Amollo, T. A.; Mola, G. T.; Nyamori, V. O. Germanium Quantum Dot/Nitrogen-Doped Graphene Nanocomposite for High-Performance Bulk Heterojunction Solar Cells. *RSC Adv.* **2018**, *8* (39), 21841–21849. https://doi.org/10.1039/C8RA04223C.

(189) Hekmatshoar, B.; Shahrjerdi, D.; Hopstaken, M.; Fogel, K.; Sadana, D. K. High-Efficiency Heterojunction Solar Cells on Crystalline Germanium Substrates. *Appl. Phys. Lett.* **2012**, *101* (3), 032102. https://doi.org/10.1063/1.4737166.

(190) Pillarisetty, R. Academic and Industry Research Progress in Germanium Nanodevices. *Nature* **2011**, *479* (7373), 324–328. https://doi.org/10.1038/nature10678.

(191) Mc Vey, B. F. P.; Prabakar, S.; Gooding, J. J.; Tilley, R. D. Solution Synthesis, Surface Passivation, Optical Properties, Biomedical Applications and Cytotoxicty of Silicon and Germanium Nanocrystals. *Chempluschem* **2016**, *81*, 60–73. https://doi.org/10.1002/cplu.201600207.

(192) Hanrath, T.; Korgel, B. A. Chemical Surface Passivation of Ge Nanowires. *J. Am. Chem. Soc.* **2004**, *126* (47), 15466–15472. https://doi.org/10.1021/ja0465808.

(193) Choi, K.; Buriak, J. M. Hydrogermylation of Alkenes and Alkynes on Hydride-Terminated Ge(100) Surfaces. *Langmuir* **2000**, *16* (20), 7737–7741. https://doi.org/10.1021/la000413d.

(194) Buriak, J. M. Organometallic Chemistry on Silicon and Germanium Surfaces. *Chem. Rev.* **2002**, *102* (5), 1271–1308. https://doi.org/10.1021/cr000064s.

(195) Choi, H. C.; Buriak, J. M. Preparation and Functionalization of Hydride Terminated Porous Germanium. *Chem. Commun.* **2000**, No. 17, 1669–1670. https://doi.org/10.1039/b004011h.

(196) Melen, R. L. Dehydrocoupling Routes to Element-Element Bonds Catalysed by Main Group Compounds. *Chemical Society Reviews*. 2016, pp 775–778. https://doi.org/10.1039/c5cs00521c.

(197) Waterman, R. Mechanisms of Metal-Catalyzed Dehydrocoupling Reactions. *Chem. Soc. Rev.* **2013**, *42* (13), 5629–5641. https://doi.org/10.1039/C3CS60082C.

(198) Li, Y.-H.; Buriak, J. M. Dehydrogenative Silane Coupling on Silicon Surfaces via Early Transition Metal Catalysis. *Inorg. Chem.* **2006**, *45* (3), 1096–1102. https://doi.org/10.1021/ic051431r.

(199) Yang, Z.; Wahl, M. H.; Veinot, J. G. C. Size-Independent Organosilane Functionalization of Silicon Nanocrystals Using Wilkinson's Catalyst. *Can. J. Chem.* **2014**, *92* (10), 951–957. https://doi.org/10.1139/cjc-2014-0048.

(200) Kim, D.; Joo, J.; Pan, Y.; Boarino, A.; Jun, Y. W.; Ahn, K. H.; Arkles, B.; Sailor, M. J. Thermally Induced Silane Dehydrocoupling on Silicon Nanostructures. *Angew. Chemie - Int. Ed.* **2016**, *55* (22), 6423–6427. https://doi.org/10.1002/anie.201601010.

(201) Iv, J. E. B.; Litz, K. E.; Giarikos, D.; Wells, N. J.; Holl, M. M. B.; Kampf, J. W. Intermediates in the Catalytic Dehydrogenative Coupling of Arylgermanes. **1997**, *3* (11), 1793–1796.

(202) Bruker AXS. *TOPAS V4: General Profile and Structure Analysis Software for Powder Diffraction Data*; 2008.

(203) Yang, Z.; Gonzalez, C. M.; Purkait, T. K.; Iqbal, M.; Meldrum, A.; Veinot, J. G. C. Radical Initiated Hydrosilylation on Silicon Nanocrystal Surfaces: An Evaluation of Functional Group Tolerance and Mechanistic Study. *Langmuir* **2015**, *31* (38), 10540–10548. https://doi.org/10.1021/acs.langmuir.5b02307.

(204) Bernard, A.; Zhang, K.; Larson, D.; Tabatabaei, K.; Kauzlarich, S. M. Solvent Effects on Growth, Crystallinity, and Surface Bonding of Ge Nanoparticles. *Inorg. Chem.* **2018**, *57* (9), 5299–5306. https://doi.org/10.1021/acs.inorgchem.8b00334.

(205) Sui, Z.; Burke, H. H.; Herman, I. P. Raman Scattering in Germanium-Silicon Alloys under Hydrostatic Pressure. *Phys. Rev. B* **1993**, *48* (4), 2162–2168. https://doi.org/10.1103/PhysRevB.48.2162.

(206) Balzar, D.; Audebrand, N.; Daymond, M. R.; Fitch, A.; Hewat, A.; Langford, J. I.; Le Bail, A.; Louër, D.; Masson, O.; McCowan, C. N.; et al. Size-Strain Line-Broadening Analysis of the Ceria Round-Robin Sample. *J. Appl. Crystallogr.* **2004**, *37* (6), 911–924. https://doi.org/10.1107/S0021889804022551.

(207) Stokes, A. R.; Wilson, A. J. C. The Diffraction of X Rays by Distorted Crystal Aggregates - I. *Proc. Phys. Soc.* **1944**, *56* (3), 174–181. https://doi.org/10.1088/0959-5309/56/3/303.

(208) Javadi, M.; Michaelis, V. K.; Veinot, J. G. C. Thermally Induced Evolution of "$Ge(OH)_2$": Controlling the Formation of Oxide-Embedded Ge Nanocrystals. *J. Phys. Chem. C* **2018**, *122* (30), 17518–17525. https://doi.org/10.1021/acs.jpcc.8b04640.

(209) Wang, Y.; Ramesh, U.; Nyamekye, C. K. A.; Ryan, B. J.; Nelson, R. D.; Alebri, A. M.; Hamdeh, U. H.; Hadi, A.; Smith, E. A.; Panthani, M. G. Synthesis of Germanium Nanocrystals from Solid-State Disproportionation of a Chloride-Derived Germania Glass. *Chem. Commun.* **2019**, *55* (43), 6102–6105. https://doi.org/10.1039/C9CC01676G.

(210) Swift, P. Adventitious Carbon?The Panacea for Energy Referencing? *Surf. Interface Anal.* **1982**, *4* (2), 47–51. https://doi.org/10.1002/sia.740040204.

(211) Barr, T. L.; Seal, S. Nature of the Use of Adventitious Carbon as a Binding Energy Standard. *J. Vac. Sci. Technol. A Vacuum, Surfaces, Film.* **1995**, *13* (3), 1239–1246. https://doi.org/10.1116/1.579868.

(212) Miller, D. J.; Biesinger, M. C.; McIntyre, N. S. Interactions of CO2 and CO at Fractional Atmosphere Pressures with Iron and Iron Oxide Surfaces: One Possible Mechanism for Surface Contamination? *Surf. Interface Anal.* **2002**, *33* (4), 299–305. https://doi.org/10.1002/sia.1188.

(213) Shirahata, N.; Seo, W.-S.; Kinoshita, T.; Yonezawa, T.; Hozumi, A.; Yokogawa, Y.; Kameyama, T.; Masuda, Y.; Koumoto, K. Interfacial Observation of an Alkylsilane Self-Assembled Monolayer on Hydrogen-Terminated Si. *Langmuir* **2004**, *20* (20), 8942–8946. https://doi.org/10.1021/la036362c.

(214) Anderson, S. L.; Luber, E. J.; Olsen, B. C.; Buriak, J. M. Substance over Subjectivity: Moving beyond the Histogram. *Chem. Mater.* **2016**, *28* (17), 5973–5975.

https://doi.org/10.1021/acs.chemmater.6b03430.

(215) Whitesides, G. M.; Crabtree, G. W. Don't Forget Long-Term Fundamental Research in Energy. *Science (80-.).* **2007**, *315* (5813), 796–798. https://doi.org/10.1126/science.1140362.

(216) Lewis, N. S.; Nocera, D. G. Powering the Planet: Chemical Challenges in Solar Energy Utilization. *Proc. Natl. Acad. Sci.* **2006**, *103* (43), 15729–15735. https://doi.org/10.1073/pnas.0603395103.

(217) Lu, L.; Zheng, T.; Wu, Q.; Schneider, A. M.; Zhao, D.; Yu, L. Recent Advances in Bulk Heterojunction Polymer Solar Cells. *Chem. Rev.* **2015**, *115* (23), 12666–12731. https://doi.org/10.1021/acs.chemrev.5b00098.

(218) Parida, B.; Iniyan, S.; Goic, R. A Review of Solar Photovoltaic Technologies. *Renew. Sustain. Energy Rev.* **2011**, *15* (3), 1625–1636. https://doi.org/10.1016/j.rser.2010.11.032.

(219) Green, M. A. Thin-Film Solar Cells: Review of Materials, Technologies and Commercial Status. In *Journal of Materials Science: Materials in Electronics*; 2007; Vol. 18, pp 15–19. https://doi.org/10.1007/s10854-007-9177-9.

(220) Mayer, A. C.; Scully, S. R.; Hardin, B. E.; Rowell, M. W.; McGehee, M. D. *Polymer-Based Solar Cells*; Elsevier, 2007; Vol. 10, pp 28–33. https://doi.org/10.1016/S1369-7021(07)70276-6.

(221) Zhang, S.; Ye, L.; Hou, J. Breaking the 10% Efficiency Barrier in Organic Photovoltaics: Morphology and Device Optimization of Well-Known PBDTTT Polymers. *Adv. Energy Mater.* **2016**, *6* (11), 1502529. https://doi.org/10.1002/aenm.201502529.

(222) Ye, L.; Zhang, S.; Zhao, W.; Yao, H.; Hou, J. Highly Efficient 2D-Conjugated Benzodithiophene-Based Photovoltaic Polymer with Linear Alkylthio Side Chain. *Chem. Mater.* **2014**, *26* (12), 3603–3605. https://doi.org/10.1021/cm501513n.

(223) Lin, Y.; Wang, J.; Zhang, Z.-G.; Bai, H.; Li, Y.; Zhu, D.; Zhan, X. An Electron Acceptor Challenging Fullerenes for Efficient Polymer Solar Cells. *Adv. Mater.* **2015**, *27* (7), 1170–1174. https://doi.org/10.1002/adma.201404317.

(224) Zhang, M.; Guo, X.; Zhang, S.; Hou, J. Synergistic Effect of Fluorination on Molecular Energy Level Modulation in Highly Efficient Photovoltaic Polymers. *Adv. Mater.* **2014**, *26* (7), 1118–1123. https://doi.org/10.1002/adma.201304427.

(225) Reichenbächer, K.; Süss, H. I.; Hulliger, J. Fluorine in Crystal Engineering - "The Little Atom That Could." *Chemical Society Reviews*. 2005. https://doi.org/10.1039/b406892k.

(226) Müller-Buschbaum, P. Structure Determination in Thin Film Geometry Using Grazing Incidence Small-Angle Scattering. In *Polymer Surfaces and Interfaces: Characterization, Modification and Applications*; Stamm, M., Ed.; Springer Berlin Heidelberg: Berlin, Heidelberg, 2008; pp 17–46. https://doi.org/10.1007/978-3-540-73865-7_2.

(227) Zhou, Y.; Eck, M.; Veit, C.; Zimmermann, B.; Rauscher, F.; Niyamakom, P.; Yilmaz, S.; Dumsch, I.; Allard, S.; Scherf, U. Efficiency Enhancement for Bulk-Heterojunction Hybrid Solar Cells Based on Acid Treated CdSe Quantum Dots and Low Bandgap Polymer PCPDTBT. *Sol. Energy Mater. Sol. Cells* **2011**, *95* (4), 1232–1237. https://doi.org/10.1016/j.solmat.2010.12.041.

(228) Beek, W. J. E.; Wienk, M. M.; Janssen, R. A. J. Hybrid Solar Cells from Regioregular Polythiophene and ZnO Nanoparticles. *Adv. Funct. Mater.* **2006**, *16* (8), 1112–1116. https://doi.org/10.1002/adfm.200500573.

(229) Kwong, C. Y.; Choy, W. C. H.; Djuri i, A. B.; Chui, P. C.; Cheng, K. W.; Chan, W. K. Poly(3-Hexylthiophene):TiO 2 Nanocomposites for Solar Cell Applications. *Nanotechnology* **2004**, *15* (9), 1156–1161. https://doi.org/10.1088/0957-4484/15/9/008.

(230) Yuan, J.; Gallagher, A.; Liu, Z.; Sun, Y.; Ma, W. High-Efficiency Polymer–PbS Hybrid Solar Cells via Molecular Engineering. *J. Mater. Chem. A* **2015**, *3* (6), 2572–2579. https://doi.org/10.1039/C4TA03995E.

(231) Huang, C.; Yu, H.; Chen, J.; Zhang, J.; Wu, Z.; Hou, C. Improved Performance of Polymer Solar Cells by Doping with Bi2O2S Nanocrystals. *Sol. Energy Mater. Sol. Cells* **2019**, *200*, 110030. https://doi.org/10.1016/j.solmat.2019.110030.

(232) Maeda, Y. Visible Photoluminescence from Nanocrystallite Ge Embedded in a Glassy SiO2 Matrix: Evidence in Support of the Quantum-Confinement Mechanism. *Phys. Rev. B* **1995**, *51* (3), 1658–1670. https://doi.org/10.1103/PhysRevB.51.1658.

(233) Amollo, T. A.; Mola, G. T.; Nyamori, V. O. Germanium Quantum Dot/Nitrogen-Doped Graphene Nanocomposite for High-Performance Bulk Heterojunction Solar Cells. *RSC Adv.* **2018**, *8* (39), 21841–21849. https://doi.org/10.1039/C8RA04223C.

(234) Müller-Buschbaum, P. A Basic Introduction to Grazing Incidence Small-Angle X-Ray Scattering. In *Applications of Synchrotron Light to Scattering and Diffraction in Materials and Life Sciences*; Gomez, M., Nogales, A., Garcia-Gutierrez, M. C., Ezquerra, T. A., Eds.; Springer Berlin Heidelberg: Berlin, Heidelberg, 2009; Vol. 776, pp 61–89. https://doi.org/10.1007/978-3-540-95968-7_3.

(235) Müller-Buschbaum, P. The Active Layer Morphology of Organic Solar Cells Probed with Grazing Incidence Scattering Techniques. *Adv. Mater.* **2014**, *26* (46), 7692–7709. https://doi.org/10.1002/adma.201304187.

(236) Wilson, A. J. C. The Optical Principles of the Diffraction of X-Rays by R.W. James. *Acta Crystallogr.* **1950**. https://doi.org/10.1107/s0365110x50001476.

(237) Yoneda, Y. Anomalous Surface Reflection of X Rays. *Phys. Rev.* **1963**, *131* (5), 2010–2013. https://doi.org/10.1103/PhysRev.131.2010.

(238) Pedersen, J. S. Determination of Size Distributions from Small-Angle Scattering Data for Systems with Effective Hard-Sphere Interactions. *J. Appl. Crystallogr.* **1994**, *27* (pt 4), 595–608. https://doi.org/10.1107/S0021889893013810.

(239) Benecke, G.; Wagermaier, W.; Li, C.; Schwartzkopf, M.; Flucke, G.; Hoerth, R.; Zizak, I.; Burghammer, M.; Metwalli, E.; Müller-Buschbaum, P.; et al. A Customizable Software for Fast Reduction and Analysis of Large X-Ray Scattering Data Sets: Applications of the New DPDAK Package to Small-Angle X-Ray Scattering and Grazing-Incidence Small-Angle X-Ray Scattering. *J. Appl. Crystallogr.* **2014**, *47* (5), 1797–1803. https://doi.org/10.1107/S1600576714019773.

(240) Ruderer, M. A.; Guo, S.; Meier, R.; Chiang, H. Y.; Körstgens, V.; Wiedersich, J.; Perlich, J.; Roth, S. V.; Müller-Buschbaum, P. Solvent-Induced Morphology in Polymer-Based Systems for Organic Photovoltaics. *Adv. Funct. Mater.* **2011**. https://doi.org/10.1002/adfm.201100945.

(241) Verploegen, E.; Miller, C. E.; Schmidt, K.; Bao, Z.; Toney, M. F. Manipulating the Morphology of P3HT–PCBM Bulk Heterojunction Blends with Solvent Vapor Annealing. *Chem. Mater.* **2012**, *24* (20), 3923–3931. https://doi.org/10.1021/cm302312a.

(242) Gargi, D.; Kline, R. J.; DeLongchamp, D. M.; Fischer, D. A.; Toney, M. F.; O'Connor, B. T. Charge Transport in Highly Face-On Poly(3-Hexylthiophene) Films. *J. Phys. Chem. C* **2013**, *117* (34), 17421–17428. https://doi.org/10.1021/jp4050644.

(243) Jiang, Z. GIXSGUI: A MATLAB Toolbox for Grazing-Incidence X-Ray Scattering Data Visualization and Reduction, and Indexing of Buried Three-Dimensional Periodic Nanostructured Films. *J. Appl. Crystallogr.* **2015**, *48*, 917–926. https://doi.org/10.1107/S1600576715004434.

(244) Müller-Buschbaum, P. Influence of Surface Cleaning on Dewetting of Thin Polystyrene Films. *Eur. Phys. J. E* **2003**, *12* (3), 443–448. https://doi.org/10.1140/epje/e2004-00014-7.

(245) Song, L.; Wang, T.; Körstgens, V.; Wang, W.; Saxena, N.; Schaffer, C. J.; Fröschl, T.; Hüsing, N.; Bernstorff, S.; Müller-Buschbaum, P. Wet Imprinting of Channel-Type Superstructures in Nanostructured Titania Thin Films at Low Temperatures for Hybrid Solar Cells. *ChemSusChem* **2018**, *11* (7), 1179–1186. https://doi.org/10.1002/cssc.201800129.

(246) Lee, J. H.; Ko, K. H.; Park, B. O. Electrical and Optical Properties of ZnO Transparent Conducting Films by the Sol-Gel Method. *J. Cryst. Growth* **2003**. https://doi.org/10.1016/S0022-0248(02)01907-3.

(247) Amollo, T. A.; Mola, G. T.; Nyamori, V. O. Polymer Solar Cells with Reduced Graphene Oxide–Germanium Quantum Dots Nanocomposite in the Hole Transport Layer. *J. Mater. Sci. Mater. Electron.* **2018**, *29* (9), 7820–7831. https://doi.org/10.1007/s10854-018-8781-1.

(248) Bencheikh, F.; Duché, D.; Ruiz, C. M.; Simon, J.-J.; Escoubas, L. Study of Optical Properties and Molecular Aggregation of Conjugated Low Band Gap Copolymers: PTB7 and PTB7-Th. *J. Phys. Chem. C* **2015**, *119* (43), 24643–24648. https://doi.org/10.1021/acs.jpcc.5b07803.

(249) Rosso-Vasic, M.; Spruijt, E.; Van Lagen, B.; De Cola, L.; Zuilhof, H. Alkyl-Functionalized Oxide-Free Silicon Nanoparticles: Synthesis and Optical Properties. *Small* **2008**. https://doi.org/10.1002/smll.200800066.

(250) Wu, Y.; Yang, H.; Zou, Y.; Dong, Y.; Yuan, J.; Cui, C.; Li, Y. A New Dialkylthio-Substituted Naphtho[2,3- c]Thiophene-4,9-Dione Based Polymer Donor for High-Performance Polymer Solar Cells. *Energy Environ. Sci.* **2019**, *12* (2), 675–683. https://doi.org/10.1039/C8EE03608J.

(251) González, D. M.; Körstgens, V.; Yao, Y.; Song, L.; Santoro, G.; Roth, S. V.; Müller-Buschbaum, P. Improved Power Conversion Efficiency of P3HT:PCBM Organic Solar Cells by Strong Spin-Orbit Coupling-Induced Delayed Fluorescence. *Adv. Energy Mater.* **2015**, *5* (8), 1401770. https://doi.org/10.1002/aenm.201401770.

(252) Burda, C.; Chen, X.; Narayanan, R.; El-Sayed, M. A. Chemistry and Properties of Nanocrystals of Different Shapes. *Chem. Rev.* **2005**, *105* (4), 1025–1102. https://doi.org/10.1021/cr030063a.

(253) O'Regan, C.; Biswas, S.; Petkov, N.; Holmes, J. D. Recent Advances in the Growth of Germanium Nanowires: Synthesis, Growth Dynamics and Morphology Control. *J. Mater. Chem. C* **2014**, *2* (1), 14–33. https://doi.org/10.1039/c3tc31736f.

(254) Seifner, M. S.; Sistani, M.; Porrati, F.; Di Prima, G.; Pertl, P.; Huth, M.; Lugstein, A.; Barth, S. Direct Synthesis of Hyperdoped Germanium Nanowires. *ACS Nano* **2018**, *12* (2), 1236–1241. https://doi.org/10.1021/acsnano.7b07248.

(255) Wang, W.; Huang, J.; Ren, Z. Synthesis of Germanium Nanocubes by a Low-Temperature Inverse Micelle Solvothermal Technique. *Langmuir* **2005**, *21* (2), 751–754. https://doi.org/10.1021/la0479531.

(256) Yu, H.; Helbich, T.; Scherf, L. M.; Chen, J.; Cui, K.; Fässler, T. F.; Rieger, B.; Veinot, J. G. C. Radical-Initiated and Thermally Induced Hydrogermylation of Alkenes on the Surfaces of Germanium Nanosheets. *Chem. Mater.* **2018**, *30* (7), 2274–2280. https://doi.org/10.1021/acs.chemmater.7b04974.

(257) Bianco, E.; Butler, S.; Jiang, S.; Restrepo, O. D.; Windl, W.; Goldberger, J. E. Stability and Exfoliation of Germanane: A Germanium Graphane Analogue. *ACS Nano* **2013**, *7* (5), 4414–4421. https://doi.org/10.1021/nn4009406.

(258) Cernetti, P.; Gresback, R.; Campbell, S. A.; Kortshagen, U. Nonthermal Plasma Synthesis of Faceted Germanium Nanocrystals. *Chem. Vap. Depos.* **2007**, *13* (6–7), 345–350. https://doi.org/10.1002/cvde.200606559.

(259) Kortshagen, U. R.; Sankaran, R. M.; Pereira, R. N.; Girshick, S. L.; Wu, J. J.; Aydil, E. S. Nonthermal Plasma Synthesis of Nanocrystals: Fundamental Principles, Materials, and Applications. *Chem. Rev.* **2016**, *116* (18), 11061–11127. https://doi.org/10.1021/acs.chemrev.6b00039.

(260) Yu, Y.; Lu, X.; Guillaussier, A.; Voggu, V. R.; Pineros, W.; de la Mata, M.; Arbiol, J.; Smilgies, D.-M.; Truskett, T. M.; Korgel, B. A. Orientationally Ordered Silicon Nanocrystal Cuboctahedra in Superlattices. *Nano Lett.* **2016**, *16* (12), 7814–7821. https://doi.org/10.1021/acs.nanolett.6b04006.

(261) Ha, P. T.; Le, T. T. H.; Bui, T. Q.; Pham, H. N.; Ho, A. S.; Nguyen, L. T. Doxorubicin Release by Magnetic Inductive Heating and in Vivo Hyperthermia-Chemotherapy Combined Cancer Treatment of Multifunctional Magnetic Nanoparticles. *New J. Chem.* **2019**, *43*, 5404–5413. https://doi.org/10.1039/C9NJ00111E.

(262) Lucia, O.; Maussion, P.; Dede, E. J.; Burdio, J. M. Induction Heating Technology and Its Applications: Past Developments, Current Technology, and Future Challenges. *IEEE Trans. Ind. Electron.* **2014**, *61* (5), 2509–2520. https://doi.org/10.1109/TIE.2013.2281162.

(263) Brown, G. H.; Hoyler, C. N.; Bierwirth, R. A. *Theory and Application of Radio-Frequency Heating.*; D. van Nostrand Company, Inc.: 250 Fourth Avenue, New York, 1947.

(264) Patidar, B.; M. Hussain, M.; Jha, S. K.; Sharma, A.; Tiwari, A. P. Analytical, Numerical and

Experimental Analysis of Induction Heating of Graphite Crucible for Melting of Non-Magnetic Materials. *IET Electr. Power Appl.* **2017**, *11* (3), 342–351. https://doi.org/10.1049/iet-epa.2016.0393.

(265) Boix, E.; Puddu, V.; Perry, C. C. Preparation of Hexagonal GeO 2 Particles with Particle Size and Crystallinity Controlled by Peptides, Silk and Silk-Peptide Chimeras. *Dalt. Trans.* **2014**, *43* (44), 16902–16910. https://doi.org/10.1039/C4DT01974A.

(266) Thanh, N. T. K.; Maclean, N.; Mahiddine, S. Mechanisms of Nucleation and Growth of Nanoparticles in Solution. *Chem. Rev.* **2014**, *114* (15), 7610–7630. https://doi.org/10.1021/cr400544s.

(267) Wang, Y.; Wu, B.; Wu, Z.; Lan, Z.; Li, Y.; Zhang, M.; Zhu, F. Origin of Efficient Inverted Nonfullerene Organic Solar Cells: Enhancement of Charge Extraction and Suppression of Bimolecular Recombination Enabled by Augmented Internal Electric Field. *J. Phys. Chem. Lett.* **2017**, *8* (21), 5264–5271. https://doi.org/10.1021/acs.jpclett.7b02308.

(268) Xue, D.-J.; Wang, J.-J.; Wang, Y.-Q.; Xin, S.; Guo, Y.-G.; Wan, L.-J. Facile Synthesis of Germanium Nanocrystals and Their Application in Organic-Inorganic Hybrid Photodetectors. *Adv. Mater.* **2011**, *23* (32), 3704–3707. https://doi.org/10.1002/adma.201101436.

(269) Islam, M. A.; Purkait, T. K.; Mobarok, M. H.; Hoehlein, I. M. D.; Sinelnikov, R.; Iqbal, M.; Azulay, D.; Balberg, I.; Millo, O.; Rieger, B.; et al. Grafting Poly(3-Hexylthiophene) from Silicon Nanocrystal Surfaces: Synthesis and Properties of a Functional Hybrid Material with Direct Interfacial Contact. *Angew. Chemie - Int. Ed.* **2016**, *55* (26), 7393–7397. https://doi.org/10.1002/anie.201601341.

(270) Gao, X.; Luo, W.; Zhong, C.; Wexler, D.; Chou, S.-L.; Liu, H.-K.; Shi, Z.; Chen, G.; Ozawa, K.; Wang, J.-Z. Novel Germanium/Polypyrrole Composite for High Power Lithium-Ion Batteries. *Sci. Rep.* **2014**, *4*, 6095. https://doi.org/10.1038/srep06095.

(271) Lin, H.-Y.; Li, C.-H.; Wang, D.-Y.; Chen, C.-C. Chemical Doping of a Core–Shell Silicon Nanoparticles@polyaniline Nanocomposite for the Performance Enhancement of a Lithium Ion Battery Anode. *Nanoscale* **2016**, *8* (3), 1280–1287. https://doi.org/10.1039/C5NR07152F.

(272) Aghajamali, M.; Xie, H.; Javadi, M.; Kalisvaart, W. P.; Buriak, J. M.; Veinot, J. G. C. Size and Surface Effects of Silicon Nanocrystals in Graphene Aerogel Composite Anodes for Lithium Ion Batteries. *Chem. Mater.* **2018**, *30* (21), 7782–7792. https://doi.org/10.1021/acs.chemmater.8b03198.

APPENDIX A

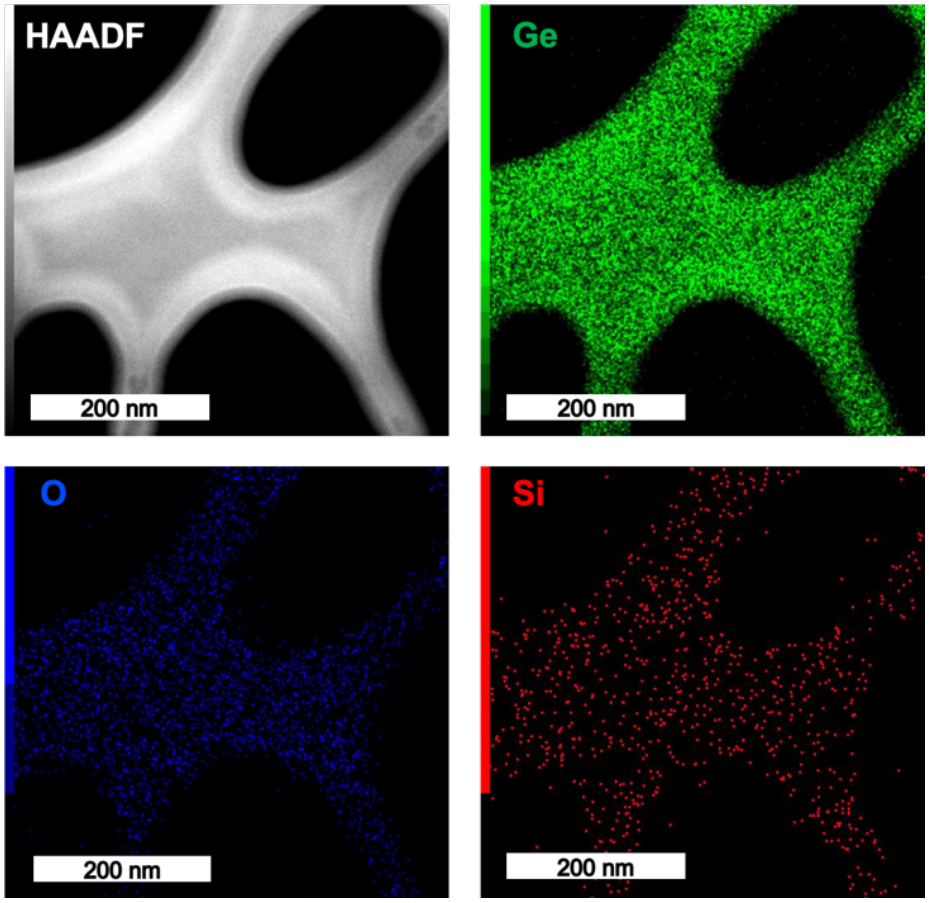

Figure A1. EDX mapping of empty holey carbon TEM grid suggesting adventitious carbon and oxygen as well as Si impurities.

A control reaction was performed using only octadecylsilane and dodecane. It was not possible to separate any solid mass by using toluene, acetonitrile, and centrifuging as in the DHC reactions. Therefore, the toluene and acetonitrile were evacuated with a rotovap, and the liquid was characterized by FTIR and ^{1}H-NMR. The FTIR shows characteristic stretching and bending modes of dodecane and octadecylsilane (Figure A2). Similar to the FTIR, ^{1}H-NMR also shows characteristic resonances for dodecane and octdecylsilane (Figure A3). The silane proton (Si–H) at 3.48 ppm is still present in the same place, however, its intensity is low; this might be due the high intensity of dodecane protons.

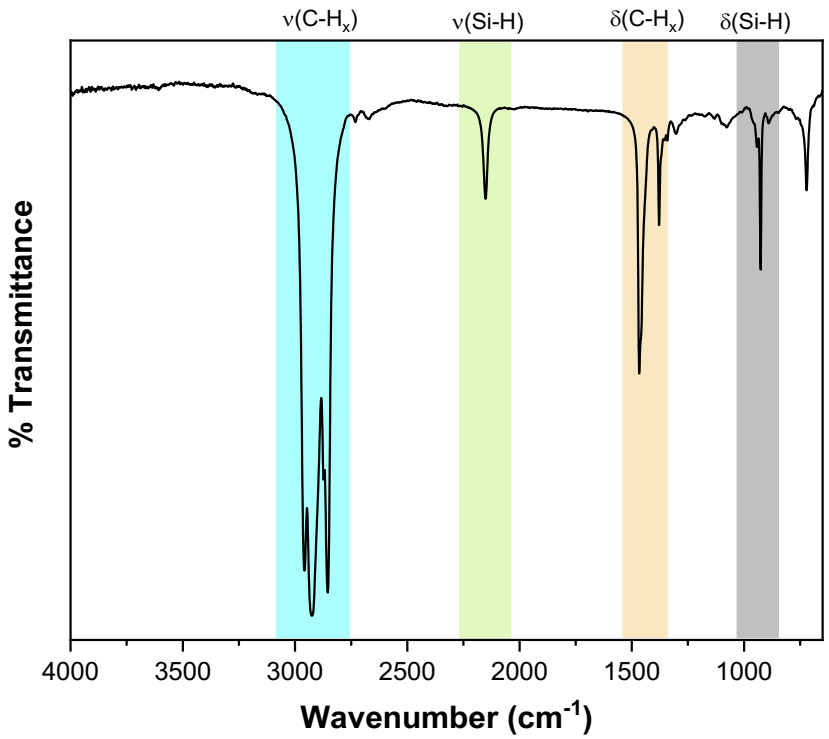

Figure A2. FTIR of the control reaction performed by using dodecane and octadecylsilane.

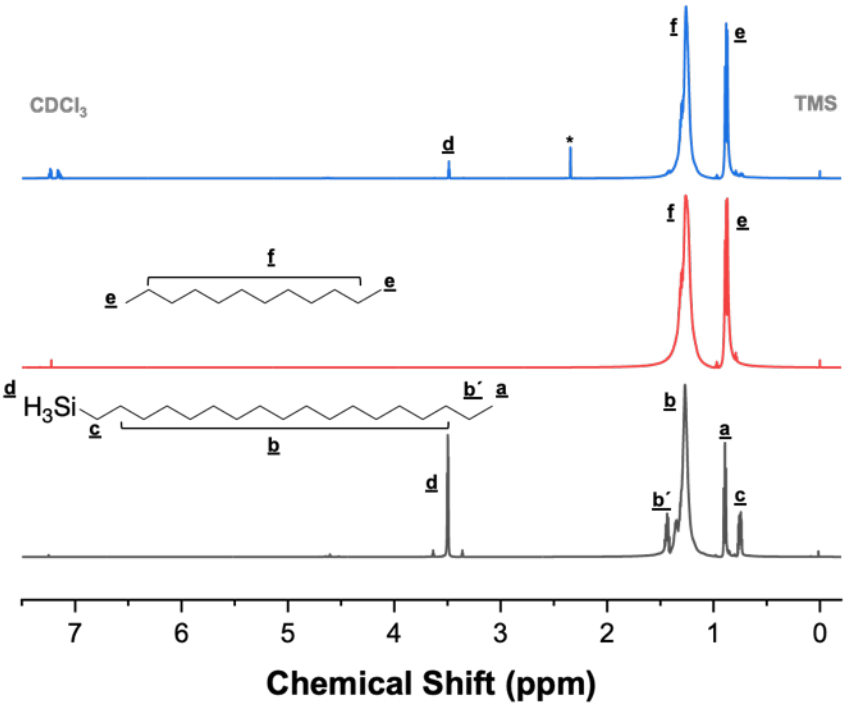

Figure A3. ^{1}H-NMR of the product of the control reaction (blue line), dodecane (red line), and octadecylsilane (grey line) in $CDCl_3$ solvent with 0.03% TMS (* suggests methyl peak of toluene).